

# THÈSE

PRÉSENTÉE À

**L'UNIVERSITÉ BORDEAUX 1**

ÉCOLE DOCTORALE DE MATHÉMATIQUES ET INFORMATIQUE

Par David THANOON

POUR OBTENIR LE GRADE DE

**DOCTEUR**

SPÉCIALITÉ : MATHÉMATIQUES APPLIQUÉES

---

## **COMPUTATIONAL FRAMEWORK FOR LOCAL BREAST CANCER TREATMENT**

---

Directeur de recherche :

Dr. Thierry COLIN(Université de Bordeaux I) et Dr. Marc GARBEY(University of Houston)

Soutenue le 28 Novembre 2011

Devant la commission d'examen formée de :

MME BASS Barbara Lee :	Professeur en établissement étranger
M. COLIN Thierry :	Professeur des Universités
M. GARBEY Marc :	Professeur en établissement étranger
MME HUBERT Florence :	Maître de conférences (HDR)
M. SAUT OLIVIER :	Chargé de recherche
M. TSEKOS Nikolaos V. :	Professeur en établissement étranger

Directeur de thèse  
Directeur de thèse

# Acknowledgments

This research work would not have been possible without the support of many people and institutions. First, I would like to express my gratitude to my supervisors, Dr. Marc Garbey and Dr. Thierry Colin, who helped me in joining the PhD program, were abundantly helpful, patient, and offered invaluable advice and support. My deepest gratitude is also due to the members of the supervisory committee especially to Dr. Barbara Bass for funding and injecting the brightest idea to this project. To Dr. Olivier Saut for his outstanding support and advice on the tumor growth modeling research and Dr. Nam-Ho Kim for his help and advice on the mechanical modeling of this dissertation.

I would also like to convey thanks to the Department of Computer Science at the University of Houston for the financial support during this PhD program.

I thank all my relatives for their patience and unconditional love and support through the duration of my studies, to Asad and Tania Ibrahim for considering me as their family as soon as they met me in Houston. Special thanks also to all my friends who have always been there for me and the members and alumni of Modeling and Computational Science Laboratory. Finally I would like to thank my wonderful fiancée Wafa Taiym who supported me, cheered me up, and motivated me during the last but most challenging semester of this PhD.

I would like to dedicate all this work to my beloved mother and father, to my sisters, to my brother in law, to my beloved uncle Emir and aunt Sheima, to my two grand mothers who passed away during the duration of this PhD. To Nadia

Abu-Adas a breast cancer survivor and to the mother of a beloved friend who was diagnosed with breast cancer during the writing of this dissertation.

# COMPUTATIONAL FRAMEWORK FOR LOCAL BREAST CANCER TREATMENT

---

An Abstract of a Dissertation  
Presented to  
the Faculty of the Department of Applied Mathematics  
University of Bordeaux I

---

In Partial Fulfillment  
of the Requirements for the Degree  
Doctor of Philosophy

---

By  
David Thanoon  
December 2011



# Abstract

Breast cancer is the most common cancer among women in the developed as well as the developing countries. There are a plethora of proposed solutions regarding possible medical interventions for breast cancer—one in particular is Breast Conserving Therapy (BCT). BCT comprises of complete surgical excision of the tumor (partial mastectomy), and post-operative radiotherapy for the remaining breast tissue. This is a feasible treatment for most women with breast cancer. The goal of BCT is to achieve local control of the cancer, as well as to preserve breast shape that appeases a woman's cosmetic concerns. Although these goals are usually achieved, there are still occasional unexpected results, such as reexcision of the tumor due to a positive margin assessment, tumor local recurrence, unsatisfactory cosmetic results, and breast pain. Other than surgical experience and judgment, there are currently no tools which can predict the outcome of partial mastectomy on the contour and deformity of the treated breast. The objective of this dissertation is to propose computational framework, which contributes to BCT operations, this was achieve by exploring two areas.

On the one hand we developed a multiscale model adapted for breast cancer tumor growth, ductal carcinoma in situ (DCIS). The model features included: nutrients growth limitation, wall degradation enzyme and HER2 chemical expression tumor phenotype. Our model successfully simulate some pattern of DCIS carcinoma. Among the interesting result we showed that the enzyme contributed to a greater tumor size and that when HER2 was overexpressed, the growth limiting factor was the EGFR. On the other hand, we developed a virtual surgery box to simulate BCT

surgery. The box will input MRI patient data and will output cosmetic and functional indicator to rate the impact of the surgery. It appears that stiffness of the tissue, resection radius as well as the lump quadrant location are the most sensitive parameters to the indicators. A healing model was also embedded to simulate the wound closure after resection, this model was stress dependent and illustrate an asymmetric wound closure progression.

The tools developed in this research allows a new type of field convergence between the surgery and computation field. At the local level it will allow surgeons and patient to be able to communicate on the pertinence and necessity of performing a lumpectomy surgery, enabling to anticipate the possible outcome of the operation. On the global aspect this type of tool gives birth to a new type of field: computational surgery, where computer scientist and surgeons work hand in hand to provide the best and the most reliable service to the patients.

# Contents

<b>I</b>	<b>Motivation and background</b>	<b>1</b>
<b>1</b>	<b>Introduction</b>	<b>2</b>
1.1	Dissertation overview and contributions . . . . .	3
<b>2</b>	<b>Background</b>	<b>7</b>
2.1	The women's breast . . . . .	7
2.1.1	Anatomy of the breast . . . . .	8
2.1.2	Breast cancer biology . . . . .	11
2.1.3	Breast cancer treatment . . . . .	28
2.2	Elements of soft tissue biomechanics modeling . . . . .	33
2.2.1	Kinematics . . . . .	33
2.2.2	Stress equilibrium . . . . .	36
2.2.3	Constitutive equations: hyperelastic material . . . . .	38
2.2.4	Computational implementation . . . . .	40
2.3	Image segmentation . . . . .	41
2.3.1	Active contour models . . . . .	42
2.3.2	Level set methods . . . . .	44
2.3.3	Energy functions . . . . .	47
2.3.4	Localized active contour model . . . . .	48
2.4	Mathematical tools element for tumor growth model . . . . .	50

2.4.1	Ordinary differential equation model . . . . .	51
2.4.2	Partial differential equation model . . . . .	54
2.4.3	Cellular automata model . . . . .	56
<b>II</b>	<b>Tumor growth modeling</b>	<b>61</b>
<b>3</b>	<b>Biology model</b>	<b>64</b>
3.1	Ductal carcinoma in situ (DCIS) pathology . . . . .	64
3.2	DCIS abnormality . . . . .	68
3.3	DCIS modeling-related work . . . . .	71
<b>4</b>	<b>Mathematical model</b>	<b>75</b>
4.1	Environmental conditions . . . . .	76
4.2	Nutrients distribution . . . . .	78
4.3	HER overexpression . . . . .	80
4.3.1	Eladdadi and Isaacson model . . . . .	80
4.3.2	Receptor-ligand interaction . . . . .	84
4.4	Computation of velocity . . . . .	85
4.5	Duct wall: localization and degradation . . . . .	87
4.6	Computational approach . . . . .	88
<b>5</b>	<b>Results &amp; discussions</b>	<b>90</b>
5.1	Results . . . . .	90
5.2	Discussion . . . . .	98
<b>III</b>	<b>Virtual surgery box for breast conserving therapy</b>	<b>104</b>
<b>6</b>	<b>Review &amp; motivation</b>	<b>105</b>

6.1	Motivation for virtual surgery . . . . .	105
6.2	Model and related work . . . . .	108
<b>7</b>	<b>The virtual surgery box (VSB)</b>	<b>114</b>
7.1	Design considerations . . . . .	114
7.2	VSB algorithm . . . . .	119
7.2.1	Image acquisition . . . . .	121
7.2.2	FEM simulation . . . . .	128
<b>8</b>	<b>Building surgical indicators</b>	<b>137</b>
8.1	Cosmetic indicator . . . . .	138
8.2	Functional indicator . . . . .	140
<b>9</b>	<b>Results &amp; discussions</b>	<b>144</b>
9.1	Vizualization results . . . . .	146
9.2	Sensitivity analysis for the VSB input . . . . .	151
9.2.1	Sensitivity analysis . . . . .	153
9.2.2	Discussion . . . . .	164
<b>10</b>	<b>Multiscale modeling</b>	<b>167</b>
10.1	Two-time scale model . . . . .	168
10.2	Model for wound healing . . . . .	171
10.3	Preliminary results . . . . .	176
<b>IV</b>	<b>Thesis review</b>	<b>181</b>
<b>11</b>	<b>Conclusions and future work</b>	<b>182</b>
11.1	Tumor growth model studies . . . . .	183
11.2	Breast conserving therapy modeling studies . . . . .	185

11.3 Work contributions . . . . .	186
11.4 Future work . . . . .	187
11.5 List of publications . . . . .	188
<b>Bibliography</b>	<b>190</b>

# List of Figures

2.1	Anatomy of the breast: a cross section through the sagittal plane (image taken from [105]). . . . .	9
2.2	(left) Breast duct micro-architecture; (right) breast duct epithelial cell polarization (Image taken from [48]). . . . .	11
2.3	Schematic of the cell cycle. Outer ring: I = Interphase, M = Mitosis; inner ring: M = Mitosis, $G_1$ = Gap 1, $G_2$ = Gap 2, S = Synthesis; not in ring: $G_0$ = Gap 0/Quiescence. The duration of mitosis in relation to the other phases has been exaggerated in this diagram. Picture taken from [7] . . . . .	18
2.4	Configuration of a deformed body (image taken from [76]). . . . .	34
2.5	Newton-Raphson method for non-linear equation $P(u) = f$ (image taken from [76]). . . . .	41
2.6	A Closed Active Contour Model: This diagram shows a snake with its ends enjoined so that it forms a closed loop. Over a series of time steps the snake moves into alignment with the nearest salient feature, here an edge (image taken from [69]). . . . .	43
2.7	Natural changes of topology in the level set framework. The right column presents the evolution of the curve and the left column shows the evolution of the associated level set function. We note that the curve changes its topology but not the level set function. (image taken from [26]). . . . .	58
2.8	Best-fit curves by Gompertz and logistic models with <i>in-vivo</i> results of tumor growth volumes in $\mu m^3$ / time in days) (image taken from [86]).	59

2.9	Sections of the virtual human brain intersecting the site of the glioma originating in the superior frontal region denoted by an asterisk (*). The left column of brain sections corresponds to the tumor at diagnosis whereas the right column represents the same tumor at death. Red denotes a high density of tumor cells while blue denotes a low density. A thick black contour defines the edge of the tumor detectable by enhanced CT. Cell migration was performed in a truly three-dimensional solid representation of the brain. The elapsed time between diagnosis and death for this virtual glioma is approximately 158 days. (image taken from [130]). . . . .	60
3.1	Solid DCIS sample: (left) general view; (right) zoomed on a fern like projection. Picture taken from [1] . . . . .	65
3.2	Cribiform DCIS sample. Pink represents the tumor cells and white spots represents the non tumor area (lumen). Picture taken from [1] .	66
3.3	Micropapillary DCIS example: (left) general view; (right) zoomed on a fern like projection. Pink represents the tumor cells and white spots represents the non tumor area (lumen). Picture taken from [1] . . . .	66
3.4	DCIS - comedo type with microcalcification [4] . . . . .	67
3.5	Possible pathways for the natural history of DCIS. Cross section of a breast-duct. Figure taken from [43] . . . . .	70
3.6	Results taken from Norton et al. work [91], from left to right: micropapillary structures, cribiform pathology, solid comedo, non-comedo. In the simulations, the green cells represent myoepithelial cells, the blue cells represent the tumour cells and the gray cells represent the necrotic cells. . . . .	73
4.1	Tumor growth model . . . . .	76
4.2	Simple ternary complex model (image modified from [38] . . . . .	81
5.1	Computational domain of the experimental setup considered . . . . .	91
5.2	Illustration of the initial environment default setup scenario. Light blue being the lumen, dark blue the stroma/healthy cell, black dot the initial proliferant cells, white disks represent the nutrient sources, and the red strips the duct wall. . . . .	92



5.3	Default test after 3000 cellular cycle. Gray: proliferant density $P \geq 0.5$ ; Black: necrosis density $N \geq 0.5$ . Percentage distribution in the whole domain: $P = 1.097\%$ , $N = 0.201\%$ , $S = 87.183\%$ and $L_u = 11.511\%$ . . . . .	93
5.4	Juxtaposition of numerical results and biopsy. <i>Left</i> : Default test after 3000 cellular cycle. Gray: proliferant density $P \geq 0.5$ ; Black: necrosis density $N \geq 0.5$ . <i>Right</i> : Biopsy of DCIS with comedo type. . . . .	93
5.5	Default test after 1000 cellular cycle with a nutrient consumption rate very low: $\Phi = 1$ . Gray: proliferant density $P \geq 0.5$ ; no necrosis core has been reported in this simulation. . . . .	94
5.6	Graphs showing the total density of cells in function of the variation rate of the default value parameter: $\rho_R$ (blue), $\rho_H$ (red), $\gamma_P$ (green), $\lambda_d$ (purple). <i>Left</i> : Proliferant cells; <i>Right</i> : Necrosis cells. . . . .	95
5.7	Total density of proliferant and necrosis cell as a function of the MMP production coefficient $\beta_{max}$ . . . . .	96
5.8	Illustration of the duct wall degradation by the MMP enzyme for a initial tumor placed at the lower part of the two-dimensional duct . .	97
5.9	Left: Initial configuration for test-A, four sources of nutrients are placed around the duct. Right: Result of test-A computation (light red) proliferant cells, (white) necrosis cells. . . . .	98
5.10	Left: Initial configuration for test-B, two sources of nutrients represented in the transverse cut parallel to the duct . Right: Result of test-B computation (light red) proliferant cells, (white) necrosis cells.	99
5.11	Transverse configuration of the duct with an initial tumor inside . . .	100
5.12	Improved tumor growth model . . . . .	102
7.1	Virtual surgery box illustration. . . . .	118
7.2	Flowchart illustrating the model construction and simulation of BCT.	120
7.3	Magnetic resonance imaging device Optima MR360 from General Electric (image taken from [9]). . . . .	122
7.4	The three MR slice orientations: 1. Coronal, 2. Sagittal, 3. Axial. (Image taken from [3]) . . . . .	123

7.5	(left) Patient positioning in MR examinations [6]; (right) Breast MRI equipment [5] . . . . .	124
7.6	Breast Magnetic Resonance Images (BMRI) in the Sagittal plane orientation . . . . .	125
7.7	Illustration of noisy breast MRI in the sagittal plane orientation . . .	126
7.8	Illustration of a 3 level multiresolution pyramid. We can see that the resolution of the images increases when going to the right direction. The use of low resolution for segmentation allows the segmentation contour to increase the computation speed as well as making sure the active contour model segments the main object. . . . .	128
7.9	Snake method segmentation for different breast MRI slices of patient #01, after: 500 iterations(left); 1250 iterations (middle, right) . . . .	129
7.10	3D breast reconstruction in MATLAB <sup>TM</sup> after segmentation of the DICOM stack . . . . .	130
7.11	SOLID187 elements of ANSYS <sup>TM</sup> . . . . .	131
7.12	Illustration of the prone and the standing position in regards to gravity direction (Image modified from [67]). Note that the “prone axis” is always attached to the patients body. . . . .	133
8.1	Virtual surgery box illustration. . . . .	138
9.1	Breast shape of patient # 02. Top row: before surgery; middle row: resection radius R=15mm; bottom row: resection radius R=35mm; .	146
9.2	Breast shape of patient # 03 R. Top row: before surgery; middle row: resection radius R=15mm; bottom row: resection radius R=35mm; .	147
9.3	Breast deform shape on a sagittal plan (from left to right) P01, P02, RP03, LP03 for a resection radius R=35mm. . . . .	149
9.4	Displacement difference on gravity loading direction of breast before and after BCT operation for the different tumor size of (top left) LP03, (top right) RP03, (bottom left) P01, (bottom right) P02. Sagittal plane	150
9.5	Breast deformation pattern after BCT operation; (red) local minima and maxima points, (green) fixed points. . . . .	151

9.6	Pain indicator contour for a tumor resection size $R_T = 30$ mm on P01. Sagittal plane. Scale map from dark blue to red: [ 1, 2, 5, 10, 15, 20, 50, 100, 140] . . . . .	152
9.7	Pain indicator contour for a tumor resection size $R_T = 30$ mm on P02. Sagittal plane. Scale map from dark blue to red: [ 1, 2, 5, 10, 15] . . .	152
9.8	This schematic drawing demonstrates the four quadrants of the breast: upper inner quadrant (UIQ), upper outer quadrant (UOQ), lower inner quadrant (LIQ), and lower outer quadrant (LIQ). The clock face model is superimposed on the four quadrant model to demonstrate how each breast is subdivided within the quadrant model. . . . .	154
9.9	Cosmetic indicator as a function of the quadrant location of a tumor resection of radius $R = 20mm$ . Left: Sagittal plan; Right: Axial plan	154
9.10	$\ \cdot\ _\infty$ norm of the functional indicator as a function of the quadrant location - Test 1; From right to left top to bottom: P01, P02, PL03, PR03. . . . .	155
9.11	Cosmetic indicator as a function of the tumor resection size $R_T$ (in mm); Left: Sagittal plan; Right: Axial plan. . . . .	156
9.12	$\ \cdot\ _\infty$ norm of the functional indicator as a function of tumor resection radius - Test 2; Sagittal plan. . . . .	157
9.13	Cosmetic indicator as a function of the bulk modulus $\kappa$ (in Pa) for patient #1 and #2. Sagittal plan . . . . .	158
9.14	$\ \cdot\ _\infty$ norm of the functional indicator as a function of the tissue compressibility - Test 3; Sagittal plan. . . . .	159
9.15	Cosmetic indicator as a function of the initial shear modulus $\mu$ (in Pa); Left: Sagittal plan; Right: Axial plan. . . . .	160
9.16	$\ \cdot\ _\infty$ norm of the functional indicator as a function of the tissue stiffness - Test 4. Sagittal plan . . . . .	160
9.17	Cosmetic indicator as a function of an imposed pressure at wound boundary surface $P_{wound}$ (in Pa). Left: Sagittal plan; Right: Axial plan.	161
9.18	$\ \cdot\ _\infty$ norm of the functional indicator as a function of the hydrostatic pressure at the wound - Test 5. Sagittal plan . . . . .	162
9.19	Cosmetic indicator as a function of the filling fluid compressibility for a tumor resection of radius $R = 30mm$ . $E_{FLUID} = 500Pa$ ; Sagittal plan	163

9.20	$\ \cdot\ _\infty$ norm of the functional indicator as a function of the filling fluid compressibility for a tumor resection of radius $R = 30mm$ . $E_{FLUID} = 500Pa$ ; Sagittal plan . . . . .	164
9.21	Absolute relative impact of parameters on the cosmetic indicator, average value on the 3 patients combined. Blue: Sagittal plan; Red: Axial plan. . . . .	165
9.22	Absolute relative impact of parameters on the functional indicator average value on the 3 patients combined. Sagittal plan . . . . .	166
10.1	Illustration of the two steps Algorithm. . . . .	169
10.2	Hexagonal grid for CA. . . . .	172
10.3	Meshing of breast with wounded area. . . . .	177
10.4	Evolution of strain energy through the healing process $E(\theta) = f(t)$ . .	178
10.5	Closure of the wound: history of the wound area. . . . .	179
10.6	Final and intermediate shape of the breast through the healing process.	180

# List of Tables

2.1	Histologic grade system . . . . .	15
5.1	Default parameter values of the tumor growth model . . . . .	103
9.1	Patient's specification . . . . .	145
9.2	Radius ( $mm$ ) and corresponding volume ( $cm^3$ ) of the occlusion that have been tested. . . . .	156
9.3	Summary of cosmetic indicator behavior in regards to the input pa- rameters. . . . .	164

# Part I

## Motivation and background

# Chapter 1

## Introduction

According to the World Health Organization, breast cancer is the most common cause of cancer among women worldwide, comprising 16% of all female cancers. It is estimated that one in eight women will face breast cancer in their lifetime. According to the American Cancer Society, about 1.3 million women will be diagnosed with breast cancer annually worldwide and about 465,000 will die from the disease. Although the incidence of breast cancer is rising, the mortality from the disease is slowly declining. This has been achieved through earlier diagnosis and improved treatment.

In the best scenario, and the most developed countries, breast cancer care is provided by breast specialists of each discipline forming a multidisciplinary team. Such a team will usually be composed of: a specialist clinician (breast surgeon), specialist radiologist and pathologist, breast care nurses, clinical oncologists, and a dedicated multidisciplinary team coordinator. The team composed of various specialties

demonstrates the multi-level implication of the disease. This leads to discussion and compromises the interest between each specialty.

*The primary objective of this dissertation is to allow applied mathematicians and computer scientists to join this multidisciplinary team by providing valuable material in the breast cancer management process.*

Implementing computers effectively in the medical field can be achieved by the merging of disciplines such as mechanical engineering, computer science, applied math, biology, oncology, and surgery. Construction of such a tool is an example of the convergence between computation sciences and surgery sciences - see <http://computational surgery.org> - providing additional digital information for clinicians and patients. We believe such a science will be a golden subject, improving with the years with computer and science progress thus providing a direct application of knowledge.

## 1.1 Dissertation overview and contributions

**The work in this dissertation focuses on the development of a computational platform for breast cancer treatment.** This work addresses two different areas of breast cancer: tumor modeling and breast conserving surgery modeling.

Tumor modeling is essential in order to understand the dynamics of growth in breast tumors. The ultimate goal being to have the ability of correctly assessing the negative margin and to predict the potential invasiveness of tumors. In both cases, this will allow the patient to avoid unnecessary surgery.



Breast conserving surgery modeling research focuses on designing a tool that will predict the surgery outcome. The ultimate goal being to compute the Breast Conserving Therapy (BCT) post-surgery shape in the short and long term. This tool will provide:

1. essential information to correctly select the best surgery option to undergo;
2. a method to outline the potential procedures that cause poor outcomes. Helping the multi-disciplinary team to accordingly adapt breast cancer treatment for each patient.
3. an educational tool for clinicians to build experiences on BCT surgery.

This dissertation is divided into four major parts, each consisting of a set of chapters focused on a specific area of work. An overview of the parts and chapters in this dissertation are provided here, highlighting the contribution made by this research to the field of breast cancer.

## **Part I: Motivation and background**

Part I provides an introduction and background information to the work in this dissertation.

**Chapter 2** provides background information on the anatomy of the breast and breast cancer, the mechanics theory for soft tissue modeling, digital image processing tools, and more specifically image segmentation tools. The chapter concludes with a informative section on mathematical tool used for tumor modeling.

## **Part II: Tumor growth modeling**

Part II describes the work done for building a tumor growth model adapted for breast cancer.

**Chapter 3** outlines the biology of the tumor growth model we simulate for this work, ductal carcinoma in situ. We detail the specificity of this tumor pathology, and detail the previous research achieved to model DCIS growth.

**Chapter 4** depicts the mathematical model of our tumor growth model. We describe the set of equations and their interaction, implementing the biology model from chapter 3. This chapter provides a strong example of multiscale mathematical modeling implementation.

**Chapter 5** presents the tumor growth results. We discuss the results obtained from such a model. At last we discuss the adjustment to provide in order to get a more realistic model adapted for breast tumor modeling.

## **Part III: Virtual surgery box for breast conserving therapy:**

Part III describes the work accomplished to simulate the breast conserving therapy surgery.

**Chapter 7** describes the design of the virtual surgery box. We outline the different tools and methods used to proceed for virtual surgery, starting from medical image processing to the mechanical modeling.

**Chapter 8** presents an innovative method to output the results of our virtual surgery box. We defined two indicators outlining the impact of surgery in two aspects: the

cosmetic and the breast functionality.

**Chapter 9** illustrates the results obtained from this virtual surgery box. We present a sensitivity analysis of data on a set of three MRI patients.

**Chapter 10** presents the design of a more advanced complex simulation model for breast conserving therapy, implementing a cellular agent to model the post surgery healing.

## **Part IV: Dissertation review**

**Chapter 11** summarizes the body of work presented in this dissertation, the limitation of our work, and outlines the future directions towards implementing a clinically applicable tool. A list of publications arising from this work is also provided at the end of the chapter.

# Chapter 2

## Background

This chapter provides the necessary background to develop our computational framework. Section 2.1 provides a description of the women's breast anatomy, breast cancer cell biology, and the current method to detect and treat breast cancer. This is followed by a description of elements for biomechanics modeling (Section 2.2). Image segmentation tools are discussed in Section 2.3. The chapter concludes with a brief review of the mathematical tool to model tumor growth (Section 2.4).

### 2.1 The women's breast

An understanding of the breast anatomy, the biological specificity of breast tumor as well as the treatment of breast cancer is important for the development of this computational framework. We will take time to describe these in the following subsections. Subsection 2.1.1 provides a precise description of the breast anatomy. This

is followed by a gross description of breast cancer pathology, the biology mechanism of cancer, and at last an in depth description of ductal carcinoma in situ (subsection 2.1.2). This section concludes with a description of the tools and method available to detect and treat breast cancer (subsection 2.1.3).

### **2.1.1 Anatomy of the breast**

The mammary glands are present in both sexes, but they normally function only in females. The biological role of the breast is to produce milk to nourish a new born baby, therefore they are only of importance when reproduction has been accomplished.

Fig. 2.1 depicts the gross anatomical structure and organization of the female breast. The breast is composed of fat, fibrous, and glandular tissues attached to the thoracic wall by connective tissues known as Cooper's ligaments. Cooper's ligaments, also known as the suspensory ligaments of Cooper, is an underlying structure of fibrous bands which provides additional support and also contributes to determining the shape and contour of the breast. It runs from the clavicle and the clavi-pectoral fascia branching out through and around breast tissue to the dermis of the skin overlying the breast.

Each breast contains 15–25 lobes of compound glands that are embedded in fibrous and adipose -fat- tissue. These lobes, contain an excretory duct that drains into the lactiferous sinus, radiating from a central nipple-areolar complex. As in all tissues, this structure is surrounded and supported by connective tissue, extracellular matrix (ECM).

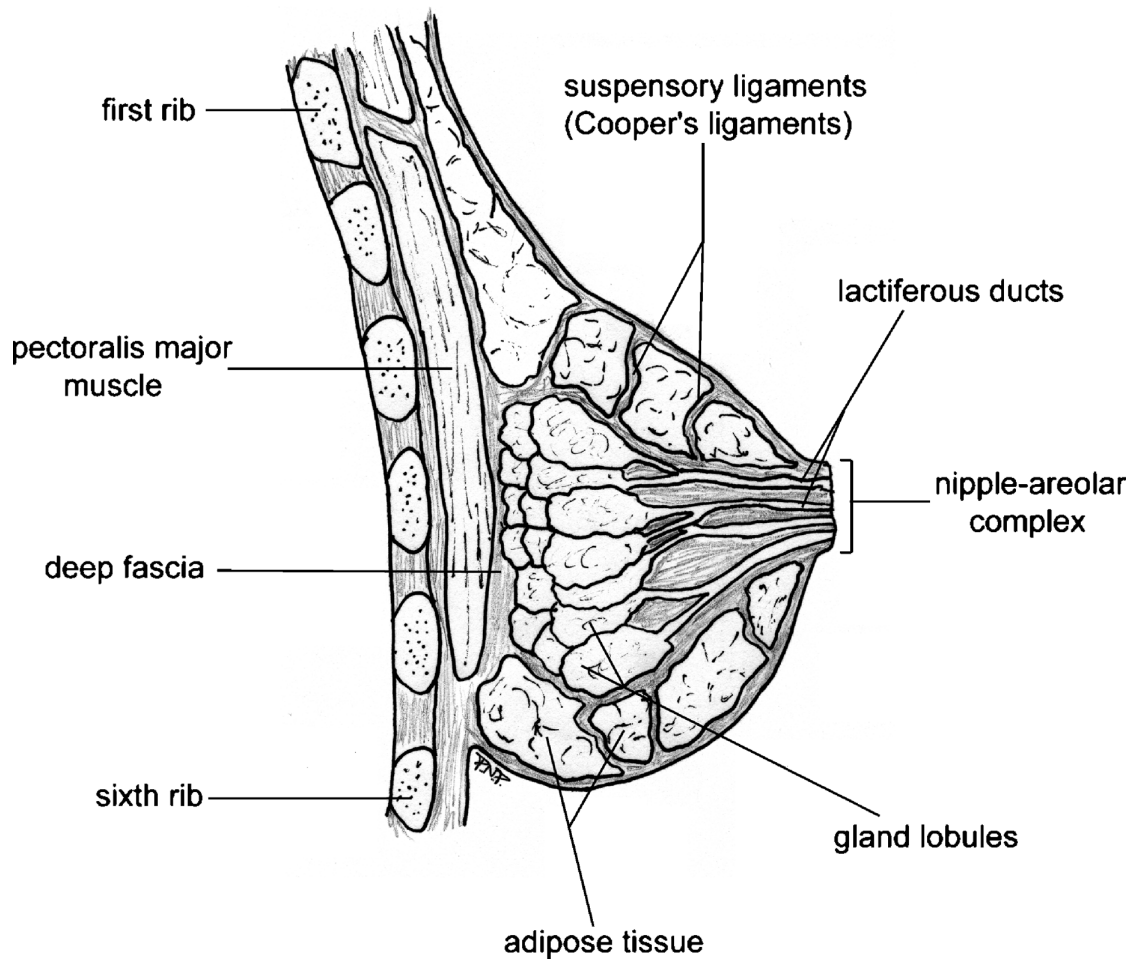


Figure 2.1: Anatomy of the breast: a cross section through the sagittal plane (image taken from [105]).

The ducts are composed of three separate layered tubes: the first is composed of the basement membrane (BM); the second of myoepithelial cells; and the third of epithelial cells [47]. The epithelial and myoepithelial cells are joined by intermediate or gap junctions and a number of inter-cellular adhesion molecules. The basement membrane is composed of fibrous proteins embedded in a hydrated gel. Both the myoepithelial cell layer and the basement membrane layer are permanent structural constituents, normally allowing only the passage of small molecules. The inside of this tubular duct is composed of a liquid called lumen. The mean diameter of the main ducts at the base of the nipple is  $1.9 \pm 0.6mm$  [111]. It is understood that the duct structure is submitted to various structure evolution at two different levels. The first one is regulated by the occurrence of pregnancy: the epithelial cells is exposed to massive change with an increasing number of alveoli developing. These alveoli produce breast milk. After pregnancy the duct comes back to normal; the epithelium is eliminated by apoptosis[127]. During lactation, myoepithelial cells play a major role, they contract in response to hormones and move milk into ducts and coordinate the ejection of milk smoothly. The second change is more of a periodical regulation: the epithelial cells oscillate with the menstrual cycle [48]. In order to maintain this structure and its normal functionality with structure remodeling, the basement membrane as well as the myoepithelial cells have asymmetric properties and functionality. These various mechanisms lead to a polarization that has only recently been revealed [90]. Cell polarity induces different levels of cell adhesion between each type of anatomy composing the ducts [116, 127, 44, 48] as well as cell

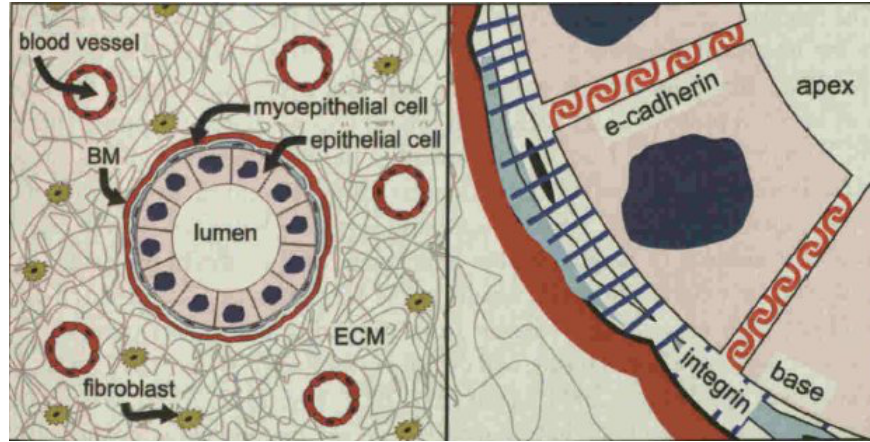


Figure 2.2: (left) Breast duct micro-architecture; (right) breast duct epithelial cell polarization (Image taken from [48]).

orientation. These observations at the cell level are expected to be a direct consequence for particular tumor shapes observed in ductal carcinoma in situ biopsy. Fig. 2.2 depicts the duct anatomy.

## 2.1.2 Breast cancer biology

In this subsection we provide a description of breast cancer classification, this is followed by a microscopic description of the breast cancer biology.

### 2.1.2.1 Breast cancer types and grade

A tumor is an overgrowth of cells. It can be made of normal cells or cancer cells. Cancer cells are cells that have grown in an uncontrolled way. The cancerous cells



may stay confined in the place of initial growth or they can start to grow in the tissue around them. The fact that the cells are invading the tissue around them is proof that the tumor is aggressive and that is generally not a good sign. Therefore, breast cancer is first classified into two types of cancers:

- In situ, which is confined in the place that they grow,
- Invasive, which grow in an uncontrolled way out of the tissue.

However, with this classification, many types of breast cancer remain. Pathologic classification of mammary carcinomas are confusing to the individual who is not a specialist in breast disease. Therefore to simplify the description of breast cancer, the pathology community separates them into 4 types:

- **DCIS**; Ductal Carcinoma In Situ, takes birth in the duct, stays confined in the duct and does not invade the adipose tissue. Necrosis can appear for this type of cancer, they may sometimes contain calcium bits inside. These types of carcinoma can become an infiltrated lesion. DCIS is not life-threatening, but having DCIS can increase the risk of developing an invasive breast cancer later on in life.
- **LCIS**; Lobular Carcinoma In Situ, first takes place in the lobule. It is a far more benign carcinoma than DCIS. LCIS is not a true cancer; it is a warning sign for an increased risk of having invasive cancer in the future, in either breast.

- **IDC**; Invasive Ductal Carcinoma, originates from the duct epithelial that crossed the membrane and invaded the stroma tissue of the breast. Once the stroma tissue is infiltrated, cancer cells can penetrate the lymphatic networks and blood vessels. Metastasis then occurs. 80 % of carcinoma are IDC.
- **ILC**; Invasive Lobular Carcinoma, originates from the breast lobule that invades the surrounding tissue. Particularly, when it invades the surrounding tissue, it invades by waves forming indian files which is of fibrous tissue, forming concentric patterns of cells around the lobular carcinoma. LCIS are much more benign than DCIS, however when it invades and infiltrates it is worse than IDC. 10 % of carcinoma are ILC, and they are much more difficult to detect.

Pathologists often assign a histological grade to the patient's cancerous breast tumor to identify the type of tumor present and help determine the patient's prognosis. The Scarff-Bloom-Richardson system is the most common type of cancer grade system used today. The histological grade of a tumor is determined after examination of the cancer cells and their patterns under a microscope. Pathologists determine a cancer's grade by observing:

- the frequency of cell mitosis (rate of cell division),
- tubule formation (percentage of cancer composed of tubular structures),
- nuclear pleomorphism (change in cell size and uniformity).

Each of these features is assigned a score going from 1 to 3 (1 indicating less aggressive and 3 indicating more aggressive - see table 2.1). Then the score of each feature is added together for a final sum that will range between 3 to 9. Grading of the tumor between 1, 2, and 3 is then done:

- **Grade 1** (Low grade or well differentiated), final sum between 3 and 5, cells generally appear normal and do not grow rapidly; cancer arranged in small tubules.
- **Grade 2** (Intermediate or moderate grade), final sum of 6 or 7, cancer cells do not look like normal cells, they grow somewhat faster than normal cells.
- **Grade 3** (High grade or poorly differentiated), final sum of 8 or 9, cells do not appear normal and tend to grow and spread more aggressively.

Pathologists also look for necrosis when determining a tumor's grade. Cancers with: high grade, necrosis, cancers close to the surrounding margin of breast tissue from a lumpectomy sample, or large areas of DCIS, are more likely to recur after breast cancer treatment than other breast cancers.

Tubule Formation (% of Carcinoma Composed of Tubular Structures)	Score
75%	1
10-75%	2
less than 10 %	3
Nuclear Pleomorphism (Change in Cells)	Score
Small, uniform cells	1
Moderate increase in size and variation	2
Marked variation	3
Mitosis Count (low power scanning (X100), find most mitotically tumor area, proceed to high power (x400))	Score
Up to 7 in 10 high-power fields	1
8 to 14	2
15 or more per 10 high power fields	3

Table 2.1: Histologic grade system

### 2.1.2.2 Getting a microscopic description of the breast cancer

In the following division we will take time to describe breast cancer at the microscopic level. We will introduce the functioning of a normal cell-cycle, then we will give a description of the hormone and growth factors, and their role in breast cancer. We will follow this with a description of breast cancer oncogenes: genes that are capable when activated of transforming a cell and contributing to the production of cancer. We will give a description of mutated tumor suppressor genes that are present in breast cancer. A tumor suppressor gene is a gene that normally restrains cell growth but when missing or inactivated by mutation, allows cells to grow uncontrolled. Finally, we will describe the metastasis mechanism in breast cancer and point out its close relationship with cell adhesion properties and degrading enzymes.

**Description of normal cell-cycle:** In order to fully understand the mechanisms underlying tumor proliferation, it is key to first comprehend the regular cell cycle. Cell division is essential for body growth and tissue repair. Individual cells must increase in size, make exact replicas of all their genetic material, and then go through a process of division. This process is commonly named the cell cycle and it is characterized by four distinct phases:  $G_1$  phase, S phase,  $G_2$  phase, and M phase. Activation of each phase is dependent on the proper progression of the previous one. Cells that have temporarily or reversibly stopped dividing are said to have entered a state of quiescence and are thus called quiescent cells. Following is a brief description of each one of these phases:

- **Quiescence -  $G_0$  phase:** Cells which are not proliferating are said to be quiescent or in “ $G_0$ ” phase. Generally cells enter the  $G_0$  state from  $G_1$  and may remain quiescent for long periods, possibly indefinitely. The metabolic demands of  $G_0$  phase varies according to the specialized functions being carried out by the quiescent cell, but there is often lower levels of energy consumption compared to actively dividing cells.
- **Interphase:** Before a cell can enter cell division, it needs to take in nutrients. All of the preparations are done during the interphase phase. Interphase is regrouped into 3 states,  $G_1$ , S,  $G_2$ .
- **Gap 1 -  $G_1$  phase:** This is the first phase within interphase. It starts from the previous M phase until the beginning of DNA synthesis. During this phase the cell increases in size. The phase is marked by the synthesis of various enzymes that are required in the S phase, mainly those needed for DNA replication. The  $G_1$ 's checkpoint is located at the end of the cell cycle.  $G_1$ 's make the key decision of whether the cell should divide, delay division, or enter a resting stage. Duration of  $G_1$  is highly variable, even among cells of the same species.
- **Synthesis - S phase:** The S phase starts when DNA synthesis begins, soon after the  $G_1$  checkpoint; when it is complete all of the chromosomes have been replicated. Thus, during this phase the amount of DNA has doubled.
- **Gap 2 -  $G_2$  phase:** At the completion of the S phase DNA replication ceases and cells enter the  $G_2$  phase. This phase lasts until the cell enters the mitosis - M phase. During this phase the cell will grow. A second checkpoint is located

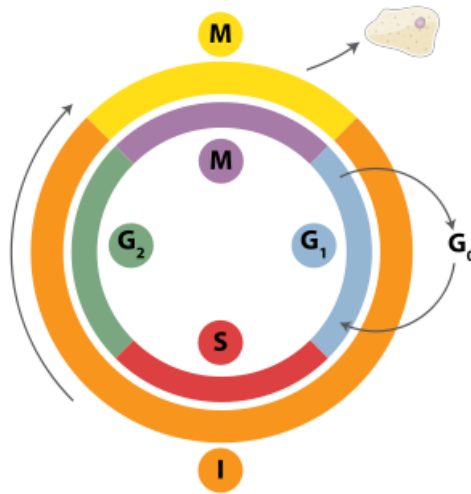


Figure 2.3: Schematic of the cell cycle. Outer ring: I = Interphase, M = Mitosis; inner ring: M = Mitosis,  $G_1$  = Gap 1,  $G_2$  = Gap 2, S = Synthesis; not in ring:  $G_0$  = Gap 0/Quiescence. The duration of mitosis in relation to the other phases has been exaggerated in this diagram. Picture taken from [7]

at the end of the  $G_2$  phase, triggering the start of the M phase. In order to pass this checkpoint, the cell checks a number of factors to ensure the cell is ready for mitosis.

- **Mitosis - M phase:** Cell growth stops at this stage and cellular energy is focused on the orderly division into two daughter cells. A metaphase checkpoint is in the middle of mitosis, it ensures that the cell is ready to complete division. After the cell has split into two daughters cells, the cell enters  $G_1$ .

As we can see, the cell cycle completes a loop where each step is controlled by checkpoints. Figure 2.3 is a graphic description of the cell cycle phase.

**Hormone regulation in breast cancer and growth factors:** Normal breast growth and development is regulated by complex interactions of many hormones and growth factors. For instance, in a normal cycle of breast estrogen, a hormone stimulates the breast growth and interaction between estrogen and cyclin-D1 stimulates cell-cycles. Because hormones and their receptors regulate normal breast tissue, it is not surprising that malignant cells arising from breast tissue, might also express receptors for many of these hormones and might retain some degree of hormonal dependence. For instance, estrogen plays a critical role in the etiology of breast cancer, when estrogenic stimulation does not occur the incidence of breast cancer is only 1% of that in normal women. Recent studies suggest that breast cancer cells under estrogen control can synthesize and secrete their own growth factors that could auto-stimulate breast cancer cells or adjacent stromal tissues through autocrine or paracrine mechanisms [64].

Also, observations dating back nearly a century show that some human breast cancers will regress following ovariectomy, however by the time breast cancer has reached the stage of a metastatic disease it retains the hormone dependent phenotype of the normal breast approximately one-third of the time.

Studies showed that not all cancers were dependent on hormones, therefore a classification of breast cancer type is given regarding hormone dependency. Tumors that are Estrogen Receptor positive (ER+) is more likely to grow in high estrogen environments. Estrogen Receptor negative (ER-) are usually not affected by the levels of estrogen in the body. The same classification is made for progesterone (PR+ / PR-). ER+ are more likely to respond to anti-estrogen therapies such as tamoxifen,



a drug that works by blocking the estrogen receptor of the breast tissue cell, and slowing their estrogen fueled growth. Note that even menopausal women can face an ER+ tumor, since estrogen can be stimulated by other parts of the body other than ovaries. 70% of breast cancer in women are ER+. Since anti-estrogen therapies are inefficient in ER-, chemotherapy will be assigned to ER- cases.

Estrogen is not the only source of growth factors, breast cancer cells can synthesize their own major growth factors. Also, stromal tissues may secrete insulin like Growth Factors (IGF-1 and IGF-2) that can stimulate breast cancer cells. The major potential autocrine/paracrine growth factors identified for breast cancer include Epidermal Growth Factor (EGF), Transforming Growth Factor alpha ( $TGF\alpha$ ), IGF-2, platelet-derived growth factor, and fibroblast growth factor.

These growth factors play a critical role in regulating the cellular process, since they are capable of stimulating cellular growth, proliferation, and cellular differentiation.

**Oncogene** Oncogenes refer to genes whose activation can contribute to the development of cancer. Numerous oncogenes have been characterized in human cancers, but relatively few have been found to be crucial in the progression of breast cancer. Amplification and over-expression of these oncogenes and oncogene products are the major mechanism through which these genes participate in carcinogenesis. Many cancer drugs target the proteins encoded by oncogenes. Here is a non-exhaustive list of oncogenes present in breast cancer:

- **The HER-2 oncogene:** The HER-2 (Human Epithelial Receptor 2, also known as HER/neu or erbB-2) gene encodes a transmembrane tyrosine kinase

growth factor receptor. A growth factor receptor's activation is initiated by binding to specific ligands, or autonomously, if present in sufficient receptor density on the cell membrane, followed by dimerization and receptor autophosphorylation, which leads to multiple transduction cascades acting through a variety of pathways. The HER-2 gene is rarely amplified in benign breast disease, and its expression varies by histologic subtypes, as it is almost exclusively found in the primary breast cancers of ductal origin, in contrast to those of lobular origin. The HER-2 gene is amplified and over-expressed in 20%-30% of invasive breast cancer and, interestingly, in the majority of high grade DCIS cases [98]. Cancers with too many copies of the HER-2 gene or too many HER-2 receptors tend to grow fast. They are also associated with an increased risk of spreading. However they may respond to treatment that works against HER-2. This treatment is called anti-HER-2 antibody therapy. Usually, a precise breast diagnosis would inform on the HER-2 status, acknowledging if it is positive(HER-2+) or negative(HER-2-). In this work, we will build a tumor growth model for this particular type of tumor, containing a further description of the chemical mechanism involved.

- **Other HER family members:** Other HER family genes, such as the one encoding the Epidermal Growth Factor Receptor (EGFR, also known as HER-1), are relevant in breast cancer. In actuality, EGFR is expressed very commonly in lung, head, neck cancer, and to a lesser extent in breast cancer. However, it is important to note that expression of EGFR has been associated with a bad clinical outcome as well as ER-.

- **Downstream signal transduction modulators:** Cancer cells receive signals from their environment, stimulating them to grow and to proliferate. To translate activation of a membrane-bound receptor into a biological response, the signal generated by receptor activation needs to be carried to the nucleus to trigger protein synthesis. This is achieved by the activation of a cascade of intracellular biochemical reactions, the so-called signal transduction pathways. In cancer cells, elements of signal transduction pathways are often mutated or over-expressed compared with normal cells. Oncogenic gene mutations frequently lead to constitutive activation of signal transduction elements, such as growth factor receptor tyrosine kinases, mimicking a situation of continuous activation of the receptor, even in the absence of the relevant growth factor. Also, more downstream signal transduction elements may be mutated or over-expressed, contributing to the malignant phenotype.
- **Cyclins:** Entrance into cell cycling and active proliferation is a tightly regulated process. Cyclin-Dependent Kinases (CDKs) are a group of proteins placed strategically throughout this phase of the cell cycle. When CDKs are activated it promotes phosphorylation of other proteins, especially retinoblastoma protein (pRb), a primary gatekeeper that allows the cell to pass from a resting state  $G_0$ , into an active cyclin and mitosis. CDKs are regulated positively by cyclin-dependent kinase inhibitors (CKIs). Cyclin D1 and cyclin E expression levels oscillate according to the cell cycle and both play a key role in the progression of the cell from  $G_1$  to S phase.

The gene encoding cyclin D1 has been found to be over-expressed in 40%-50%

of invasive breast cancers and amplified in 10%-20% of cases [98]. When cyclin D1 is complexed with its CDK partner, the pRb tumor suppressor protein is phosphorylated, releasing the transcriptional factor E2F, and inducing proteins required for DNA synthesis. High cyclin D1 expression levels appears to be positively associated with ER+ and an increased proliferative index.

The gene encoding cyclin E is rarely amplified in breast cancer ( $\sim 2\%$ ); however, over-expression and alteration of the degradation pathway resulting in the accumulation of low-molecular weight isoforms have been demonstrated in 20%-30% of breast cancers [98]. Nevertheless, it is rare to find both cyclin D1 and E concomitantly over-expressed. In the same pathway of cyclin D1, over-expressed cyclin E results in hyperphosphorylation of pRb and increased proliferation, however in contrast to high cyclin D1 tumors, high cyclin E tumors are additionally able to induce the S phase independently of pRb phosphorylation and E2F activation. The overall result of this is a marked reduction in cell cycle control and a significant dysregulation of proliferation. High cyclin E tumors are more likely to be of a higher grade than high cyclin D1 tumors which are typically hormone-receptor negative: ER-, have a more marked proliferative index and are associated with a worse outcome. There are many reasons why cyclin E is associated with an aggressive phenotype:

- cyclin E over-expressed tumors are able to bypass the pRb node, allowing for pronounced active cell cyclin;
- high cyclin E levels, in contrast to high cyclin D1 levels, are associated with increased genomic instability;

- the enzyme that cleaves E into its low-weight-molecular isoform, has also been associated with an increased propensity for invasion and metastases and may, in part explain the more aggressive phenotype.

However the routine use of cyclins or their isoforms for prognostic or therapeutic decisions remain unproven.

- **c-myc oncogene:** The c-myc oncogene acts as a transcriptional regulator that is involved in the cellular proliferation, differentiation, and apoptosis. Over-expression and amplification is observed in 6%-32% of breast tumors. However, it is not well defined how this oncogene affects cancer growth, even though in some cases it is associated with the worse prognosis or more aggressive clinical features [106].

**Tumor suppressor gene** Tumor suppressor genes refer to those genes whose loss of function results in the promotion of malignancy. They are usually negative regulators of growth or other functions that may affect invasive and metastatic potential, such as cell adhesion and regulation of protease activity. Tumor suppressor genes have not been extremely useful in diagnostic applications, with the exception of inherited susceptibility genes. Here is a non exhaustive list of tumor suppressor gene activity in breast cancer:

- **p53 oncogene:** p53 is possibly the most-studied tumor suppressor gene; mutation of p53 is estimated to occur in up to half of all human cancers and in approximately 20%-30% of breast cancers. It codes a protein that has multiple

functions that are regulated via phosphorylation at different sites. Normally p53 acts as a regulating mechanism for cell division. When activated, p53 can directly interact with DNA to yield transcription of a number of genes, including CKI (Cyclin-dependent kinase inhibitor), and lead to a temporary arrest of the cell cycle in the G1 or G2/M phase prior to mitosis to allow for DNA repair. p53 has also been shown to factor in the expression in other tumor suppressors or regulators of angiogenesis and metastasis [98].

Abnormalities of p53 expression have been associated with some of the worst prognoses in breast cancer cases. Its over-expression has been strongly linked with ER-. Independent of ER status, mutation of p53 increases the relative risk of relapse by roughly 33% [98].

- **p27 and Skp2:** p27 belong to the family of cyclin-dependent proteins kinase inhibitors (CKIs) known as Cip/Kip. Generally, CKIs slow the progression of the cell cycle. p27 is capable of binding to a number of unique cyclin/CDK complexes to attenuate their activity, typically directing the cell towards arrest in the G1 phase. Mutation of p27 appears to be a uncommon event in malignancy, occurring in only 1% of tumors in one study [98]. In breast cancer, diminished expression of p27 is associated with shorter overall survival and shorter time to progression and seems to be a stronger independent predictor of outcome than either p53 alterations or tumor grade. Some degree of the poor prognosis conferred by loss of p27 expression may be related in part to a role in modulating cell-cell adhesion, and thus a tendency for metastatic spread. Skp2 is required for the degradation of p27, preferentially Skp2 is over-expressed

in ER- and HER2- breast cancers, these are defined as a subset of breast cancer recently defined as the “basal phenotype”.

- **BRCA-1:** BRCA-1 is a gene associated with familial breast cancer. It is classified as a tumor suppressor gene that is hereditary (0.12% of the population carries a mutation of BRCA-1), with very few sporadic cases. BCRA-1-related cancers are less likely to show ER positivity. The functions associated with BRCA-1 is to localize areas of damaged DNA, support a role in regulation of transcription, as well as repair of double-stranded DNA.
- **BRCA-2:** The BRCA-2 gene shares many features with BRCA-1. It is needed for the high fidelity phase of DNA repair. BRCA-2 mutation has been strongly associated with high tumor grade as has BRCA-1, but the malignant cells show a less tubule formation. As with BRCA-1, sporadic mutations of BRCA-2 are very rare.
- **Other tumor suppressor genes:** A number of other tumor suppressors of importance in breast cancer are known, and still others are being identified. Here is a few of the known genes:
  - BRCA-3 gene;
  - PTEN;
  - Cell cycle checkpoint kinase(CHK2);
  - ATM gene;
  - Retinoblastoma (Rb).

## **Mechanism of metastasis in breast cancer - cell adhesion properties &**

**MMP enzyme** Tumor cells separate themselves from a solid tumor mass more easily than their counterparts, normal cells from surrounding tissue. Detachment of cells are regulated by the property of tumor cell “adhesiveness”. This mobility provides tumor cells with the capability of metastasis. Cadherins are the family of functionally related transmembrane proteins responsible for the cell-cell adhesion mechanism that is crucial for the mutual association of cells (see figure 2.2).

Cadherins bind cell’s tightly by homophilic, identical type binding, interaction, noting that the inactivation of other adhesion systems have little effect on cell-cell adhesion when cadherins are functioning. However treatment of cell layers expressing cadherins with anti-cadherins antibodies, induces the dispersion of cells. These properties indicate that cadherins play a major role in inter-cellular physical adhesion, and that the number of cadherin molecules expressed in a cell directly affect its adhesiveness.

It is believed that the suppression of E-cad activity might trigger the release of tumor cells from the primary lesion in cancerous tissue. It was demonstrated that inhibition of cadherins by antibodies promotes cell invasion in a model system in vitro [21]. Furthermore, more recent studies with transfected cell lines have shown that selective loss of E-cadherin expression can generate differentiation and invasiveness of human carcinoma cells [53]. Following this path, Oka et al. [92] suggested that E-cadherin may play an important role in invasion and metastasis of human breast cancer.

Metastasis represents a critical event in the course of tumor progression, usually



leading to the worse prognosis for patients. Invasion and metastasis of tumor cells into their surrounding connective tissue and to distant sites is a multistep process. Carcinoma cells must first detach from neighboring tumor cells, invade through the basement membrane, and migrate into surrounding tissue. The invading cells may then enter the vascular or lymphatic circulation. Finally, the cells may then attach to the wall of the capillary at a second site and pass through the basement membrane into a target organ, where growth resumes. As we mentioned earlier cellular adhesion molecules may play a role both in the detachment of tumor cells from a primary tumor and in reimplantation at a distant site. Another key factor reported for metastasis to occur is the secretion of the matrix metalloproteinases (MMPs) enzymes.

Indeed, for breast cancer cells to manifest their malignant potential, they must develop the ability to break through and dissolve extracellular matrices (ECM), particularly the delimiting basement membrane (BM). The degradation of the BM and ECM is catalyzed by the concerted action of several classes of ECM-degrading enzymes. One important class of ECM-degrading enzymes includes the matrix metalloproteinases.

This biological description is important to understand the origin and mechanism of breast cancer. We will now describe how this disease is treated.

### **2.1.3 Breast cancer treatment**

It is considered that 1 in 8 women will face breast cancer during their lives. Early detection resides the best solution with the assumption being that early detection

will improve outcome. In this subsection, we will describe the general principle of management available for breast cancer and detail in more depth the surgery procedure effective for breast cancer.

#### **2.1.3.1 Principle of management**

In order to improve early detection for breast cancer, a number of screening tests have been employed including: clinical and self breast exams, mammography, genetic screening, ultrasound, and magnetic resonance imaging (MRI). Patient of age 20 are invited to proceed for a breast self exam, reporting to their doctor any abnormality, patient of age 30 are also invited to go under a clinical breast exam every three years. Although genetic testing does not detect cancers, it may reveal susceptibility to developing cancer. Women who are known to have a higher risk of developing breast cancer usually undertake more aggressive screening programs. National health screening programs are also established in most developed countries: in the United States the screening policy recommends a yearly mammogram starting of age 40 and continuing for as long as a woman is in good health, in Europe the screening policy starts at age 50.

A mammogram is a mammography exam which is a specific type of imaging that uses a low-dose x-ray system to examine breasts. It gives a 2D representation of the projected X-rays. During this procedure the breast is compressed in order to reduce the dosage of x-rays transmitted. This tool is also used for the diagnosis of breast diseases in women. Mammography plays a central part in early detection of breast cancers because it can show changes in the breast up to two years before a

patient or physician can feel them. Mammograms have a sensitivity ability to detect true-positives of up to 90% in women over the age of 50 years [96]. Analysis of these images can be challenging and sometimes can require an adjunct scanning method such as ultrasound scanning. Ultrasound uses harmless, high frequency sound waves to form an image (sonogram). The sound waves pass through the breast and bounce back or echo from various tissues to form a picture of the internal structures. It is not invasive, does not involve radiation, and is effective for imaging soft tissues of the body. Breast MRI is prescribed if there is a discrepancy between the clinical, mammographic, and ultrasound measure of the tumor [96]. MRI is also a powerful tool for screening patients with high genetic risk, dense breast, or to assess the size of the the tumor if breast conserving surgery is being contemplated. Any patient showing a significant abnormality will then undergo a biopsy.

A biopsy is the removal of a piece of breast tissue for examination by a pathologist. There are several kinds of biopsies available for breasts, each one presenting their own advantages and disadvantages. The tissue sample will be analyzed by a laboratory confirming or discrediting the presence of a tumor, and returning as well the classification and grade of the tumor. A complete analysis of the disease will contain microscopic and macroscopic information about the disease. Recalling descriptions we provided from the previous section, the report would contain answers to the following questions:

- What is the size of the tumor: cm?
- What type of cancer is it: DCIS, IDC, LCIS, ILC?

- If there is lymphatic or vascular invasion?
- How many lymph nodes are involved?
- What is the cancer cell grade: 1,2,3?
- Is the tumor ER+ or ER-?
- Is the tumor PR+ or PR-?
- Is the tumor HER-2+ or HER-2-?

Following diagnosis of breast cancer, the majority of patients will undergo surgical treatment. This may be followed by adjuvant therapy such as radiotherapy, chemotherapy, and/or hormone therapy. For most of the patients, a range of surgical options will be offered and discussed in correlation with their diagnosis. This appears to be a challenging moment for patients who need to take on a load of information. Although there is a wide range of surgery available to treat breast cancer, traditionally the surgical options consists of breast conserving therapy or a mastectomy, the other types of surgery offered usually derives from these two. A range of oncoplastic breast-conserving procedures can be added to these two surgeries. We will now give a more in depth description of these two surgical procedures: breast conserving therapy and mastectomy.

#### **2.1.3.2 Surgery for breast cancer**

Surgery remains to this day the mainstay to treat breast cancer. The goal of the surgery procedure is to remove the cancerous tissue inside the breast. Since the

breast is not a vital organ and its only biological role is to provide milk for a newborn, breast surgery remains one of the safest surgery procedures. Mastectomy and breast conserving therapy are the two surgical procedures conventionally proposed for breast cancer.

**Mastectomy:** Mastectomy is the medical term for the surgical operation that removes one entire breast, or both, usually including the nipple and the areola. Depending on the patient case, there are a variety of types of mastectomy. It will usually include removal of the axillary lymph nodes or the first removal of the sentinel lymph nodes for a biopsy. A patient will opt for a mastectomy if the tumor is relatively big compared to the patient breast size, if the patient would rather avoid anxiety of cancer local recurrence, or to avoid undergoing radiation therapy. This surgery however comes with an aesthetic drawback since the breast is completely removed. Some mastectomy procedure, will take into account the possibility of a breast reconstruction procedure.

**Breast conserving therapy:** Breast conserving surgery, lumpectomy, is less radical than a mastectomy. Lumpectomy consists of the removal of a part of the breast, usually the tumor including a positive margin, as opposed to the entire breast. Lumpectomy followed by radiotherapy is labeled as breast conserving therapy (BCT). Appropriate radiotherapy is needed in order to completely eliminate residual cancerous tissue. Whelan et al. [142] reported that the risk of local recurrence for lumpectomy, decreases by 24% when appropriate radiotherapy is applied. The advantage of BCT over mastectomy is that it may offer faster recovery and better cosmetic

outcome for patients. Nevertheless the patient needs to undergo radiation therapy in order to reduce local recurrence to the same rate of the mastectomy procedure.

## 2.2 Elements of soft tissue biomechanics modeling

This section presents an introduction for the subsequent mechanical modeling of breast tissue. The description below is mainly based on the books by Malvern [85] and Holzapfel [63]. This section first outlines the kinematics necessary to set the equations relating strain tensors to displacement gradients, we then present the stress equilibrium equations derived from conservation laws, then we introduce the constitutive equation for a non-linear elastic material: hyperelastic material. These equations constitute the connection between stress and strain of a material. We conclude with a brief discussion on the computational implementation of these non-linear mechanical models.

### 2.2.1 Kinematics

In this work we only consider Cartesian coordinate sets. We consider a continuous body  $\Omega_0$  that has been subjected to deformation and is now in a deformed state  $\Omega_x$  (see figure 2.4). We identify the current state of the deformed body as the *current configuration* and the original, initial state, as the *reference configuration*. For those two types of configurations, two types of coordinate systems are used to analyze stresses and strains:

- **material coordinates**  $(X_1, X_2, X_3)$  refers to the behavior of a material point, this material coordinate system is often called a *Lagrangian* description;
- **spatial coordinates**  $(x_1, x_2, x_3)$  refers to the material behavior at a particular spatial position.

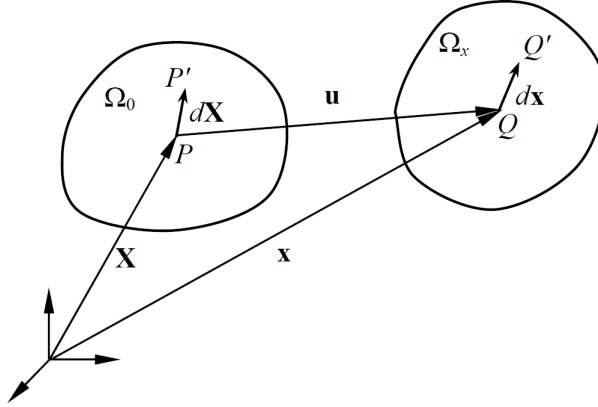


Figure 2.4: Configuration of a deformed body (image taken from [76]).

As the body deforms, the material coordinate axes deforms with it, and hence the coordinate values of a material point does not change during the deformation, whereas with the spatial coordinates of a material point can be associated with a different material point after deformation. The measure of strain requires a relationship between the spatial coordinates of material points in a deformed body and the material coordinates of the material points in the reference configuration. It is then possible to measure a change in the length of a material line segment using this relationship.

Let us consider an initial state of a body (*reference configuration*),  $\mathbf{x}$ , deform to the *current configuration*,  $\mathbf{X}$ . The deformation can be represented by mapping

$\chi : \Omega_0 \mapsto \Omega_x$  which takes points  $\mathbf{X}$  in  $\Omega_0$  to points  $\mathbf{x}$  in  $\Omega_x$  :  $\mathbf{x} = \chi(\mathbf{X})$ . Suppose now that two particles of the body are located at points  $\mathbf{X}$  and  $\mathbf{X} + d\mathbf{X}$  in the undeformed configuration, after deformation they are positioned at  $\mathbf{x} = \chi(\mathbf{X})$  and  $\mathbf{x} = \chi(\mathbf{X} + d\mathbf{X})$  respectively. Then the *deformation gradient tensor*,  $\mathbf{F}$ , relating the line element in the initial state to the line element in the current state is defined by the relationship  $d\mathbf{x} = \mathbf{F}d\mathbf{X}$ , where:

$$\mathbf{F} = \frac{\partial \mathbf{x}}{\partial \mathbf{X}} \quad (2.1)$$

Note that the Jacobian  $J = \det(\mathbf{F})$  is a measure of the volume change of the material due to deformation  $dv = JdV$ , where  $dV$  is the volume in the *reference configuration* and  $dv$  is the corresponding volume in the *current configuration*. Similarly, an area in the *reference configuration* is referred to as  $dA$ , and in the *current configuration* as  $da$ .

The deformation gradient tensor represents the entire deformation, including rigid body motion and the strain, that the material experiences. It can be decomposed according to the polar decompositions  $\mathbf{F} = \mathbf{R}\mathbf{U}$  where  $\mathbf{R}$  is a proper orthogonal tensor, representing the rigid body rotation, and  $\mathbf{U}$  a positive definitive and symmetric tensor, representing the material strain independent of the rigid body rotation. Because  $\mathbf{U}$  is a positive and symmetric tensor, there exists a basis in which  $\mathbf{U}$  is diagonal. These are the principal directions of  $\mathbf{U}$  and by definition, the positive diagonal components,  $\lambda_1, \lambda_2, \lambda_3$  of  $\mathbf{U}$  in the principal axes called the principal values of  $\mathbf{U}$ , representing the principal stretches. Since a pure rotation should not induce any stresses in a deformable body, it is often convenient to use rotation-independent measures of deformation in continuum mechanics. We derive a tensor that is independent of the



rigid body rotation, the *right Cauchy Green tensor*,  $\mathbf{C}$ , defined as:

$$\begin{aligned}\mathbf{C} &= \mathbf{F}^T \mathbf{F} \\ &= \mathbf{R} \mathbf{U}^T \mathbf{R} \mathbf{U} \\ &= \mathbf{U}^T \mathbf{U}\end{aligned}$$

since  $\mathbf{R}$  is an orthogonal tensor:  $\mathbf{R}^T \mathbf{R} = \mathbf{I}$ , where  $\mathbf{I}$  is the identity tensor . In three-dimension,  $\mathbf{C}$  is a  $3 \times 3$  matrix and possesses 3 invariants under coordinate change:

$$I_1 = \text{tr}(\mathbf{F}) = \lambda_1^2 + \lambda_2^2 + \lambda_3^2 \quad (2.2)$$

$$I_2 = \frac{1}{2}[(\text{tr} \mathbf{C})^2 - \text{tr}(\mathbf{C}^2)] = \lambda_1^2 \lambda_2^2 + \lambda_2^2 \lambda_3^2 + \lambda_3^2 \lambda_1^2 \quad (2.3)$$

$$I_3 = \det(\mathbf{C}) = \lambda_1^2 \lambda_2^2 \lambda_3^2 = J^2 \quad (2.4)$$

often used in the expressions for strain energy density functions. When there is no motion or deformation, the deformation gradient tensor will be equal to the identity tensor, and hence the right Cauchy Green deformation tensor is as well. In order to get a strain tensor such that no motion or deformation yields the zero tensor,  $\mathbf{0}$ , the *Green Strain tensor*,  $\mathbf{E}$ , was introduced, satisfying this property:

$$\mathbf{E} = \frac{1}{2}(\mathbf{C} - \mathbf{I}) \quad (2.5)$$

### 2.2.2 Stress equilibrium

Lets consider a quasi-static equilibrium state of a body (inertia effect neglected), under the body force,  $\mathbf{b}$ , per unit of volume and the traction forces,  $\mathbf{t}$ , per unit of

area, one can establish the momentum balance:

$$\int_a \mathbf{t} da + \int_v \mathbf{b} dv = 0 \quad (2.6)$$

using the Gauss theorem and definition of the Cauchy stress tensor  $\sigma$  (defined through the constitutive equations) we can write

$$\int_v (\nabla \cdot \sigma + \mathbf{b}) dv = 0 \quad (2.7)$$

The Cauchy stress tensor refers to the force measured per unit area in the deformed configuration with respect to the deformed coordinate system. Other measures of stress include  $\mathbf{P}$  and  $\mathbf{S}$ , respectively the 1<sup>st</sup> and the 2<sup>nd</sup> *Piola-Kirchhoff* stress tensor defined by:

$$\mathbf{P} = J\sigma\mathbf{F}^{-T} \quad (2.8)$$

$$\mathbf{S} = J\mathbf{F}^{-1}\sigma\mathbf{F}^{-T} \quad (2.9)$$

A strong form of the equilibrium state can be written :

$$\nabla \cdot \sigma + \mathbf{b} = 0 \quad (2.10)$$

For numerical purposes we write the weak form of equation 2.10 using the principle of virtual work, by introducing an arbitrary virtual displacement  $\delta \mathbf{u}$ :

$$\delta W = \int_v J \sigma : \frac{\partial(\delta \mathbf{u})}{\partial \mathbf{x}} dv - \int_s \mathbf{t} \cdot \delta \mathbf{u} ds - \int_v \mathbf{b} \cdot \delta \mathbf{u} dv = 0$$

For incompressible materials, introducing  $\delta p$  an arbitrary variation of the hydrostatic pressure term, the volume conserving constraint  $J = 1$  is weakly enforced explicitly by:

$$\int_v \delta p (J - 1) dv = 0.$$

$\delta p$  can be interpreted by the physical hydrostatic pressure required to enforce the constraint  $J = 1$ .

### 2.2.3 Constitutive equations: hyperelastic material

The fundamental equations introduced in section 2.2.2 - 2.2.1 are essential to characterize the kinematics, stresses, and balance principles, and hold for any continuum body for all times. However they are not a complete set since they do not distinguish one material from another and remain valid in all branches of continuum mechanics. Hence we must establish additional equations, connecting the forces or stresses ( $\sigma$ ,  $\mathbf{S}$ , or  $\mathbf{P}$ ) to the deformation or strain ( $\mathbf{F}$ ,  $\mathbf{C}$ , or  $\mathbf{E}$ ). This relationship is known as the *constitutive relation*.

A material is called *Cauchy-elastic* (or elastic) if the Cauchy stress at each material point is determined only by the current state of deformation (with respect to any arbitrary reference configuration). In other words, the Cauchy stress,  $\sigma$ , does not depend on the deformation history. Neglecting the effect of temperature and assuming the body to be homogeneous, a constitutive equation for the Cauchy stress tensor can be formulated based on the deformation gradient:  $\sigma = f(\mathbf{F})$ . Frame indifference requires that the constitutive relationship should not change when the location of the observer changes, therefore it is independent of rigid-body rotations and it can be regarded as a function of any strain measure introduced earlier:  $\mathbf{C}$  or  $\mathbf{E}$ . While Roose et al. [117] simulated breast tissue mechanics using linear-elastic material, it is commonly said that hyperelastic material provides a more coherent model to describe breast tissue [121, 123, 17, 18, 19, 131, 132, 133, 100, 108, 32].

The hyperelastic material is a special case of a Cauchy elastic material with a type of constitutive model for which the stress-strain relationship derives from a strain energy density function,  $W$ . This strain energy function represents the work done by the stresses from the initial to the final configuration. Stresses are calculated by differentiating the strain energy function with respect to a measure of deformation or strain, i.e.

$$\mathbf{S} = \frac{\partial W(\mathbf{E})}{\partial \mathbf{E}} = \frac{\partial W(\mathbf{C})}{\partial \mathbf{C}} \frac{\partial \mathbf{C}}{\partial \mathbf{E}} = 2 \frac{\partial W(\mathbf{C})}{\partial \mathbf{C}} \quad (2.11)$$

Additionally, if the material behaves isotropically with respect to the undeformed configuration, then the strain energy function,  $W$ , may be expressed in terms of the principal invariants of its argument:

$$W = W(\mathbf{E}) = W(I_1, I_2, I_3) \quad (2.12)$$

The majority of strain energy functions used in the literature to model the behavior of breast tissue was initially developed for the characterization of rubber-like materials. The polynomial hyperelastic material model [115] is a phenomenological model of rubber elasticity. In this model, the strain energy density function is in the form of a polynomial in the two invariants  $I_1, I_2$  of the left Cauchy-Green deformation tensor and an additional dependence on volume is added for compressible materials:

$$W = \sum_{i,j=0}^n C_{ij} (\bar{I}_1 - 3)^i (\bar{I}_2 - 3)^j + \sum_{k=0}^m D_k (J - 1)^{2k} \quad (2.13)$$

where:

$$\bar{I}_1 = J^{2/3} I_1$$

$$\bar{I}_2 = J^{2/3} I_2$$

$C_{ij}$  and  $D_k$  are the material constant expressed in Pa. If we only consider in equation 2.13,  $n = 1$ ,  $m = 1$ , and  $C_{00} = C_{01} = C_{11} = 0$  the polynomial reduces to the compressible Neo-Hookean solid model:

$$W = C_{10}(\bar{I}_1 - 3) + D_1(J - 1)^2 \quad (2.14)$$

If we consider  $n = 1$ ,  $m = 1$ , and  $C_{00} = C_{11} = 0$  the polynomial reduces to the compressible Mooney-Rivlin material

$$W = C_{01}(\bar{I}_2 - 3) + C_{10}(\bar{I}_1 - 3) + D_1(J - 1)^2 \quad (2.15)$$

The material parameters are fit by performing tension compression tests. In these two models the compressibility part is identified by the last term of the polynomial.  $D_1$  is representing the bulk modulus of the material, an analogy of such a term would be the hydrostatic pressure necessary to compress the volume by a factor of  $1/e$ . The values of these parameters will be discussed later.

## 2.2.4 Computational implementation

In order to simulate soft tissue mechanics using the computer we will use the commercial software ANSYS<sup>TM</sup> [8] using the Finite Element Method (FEM). ANSYS<sup>TM</sup> employs the “Newton-Raphson” approach to solve non-linear problems. In this approach, the load is subdivided into a series of load increments. The load increments can be applied over several load steps. Figure 2.5 illustrates the use of Newton-Raphson equilibrium iterations in one-dimension non-linear analysis.

Before each solution, the Newton-Raphson method evaluates the out-of-balance load

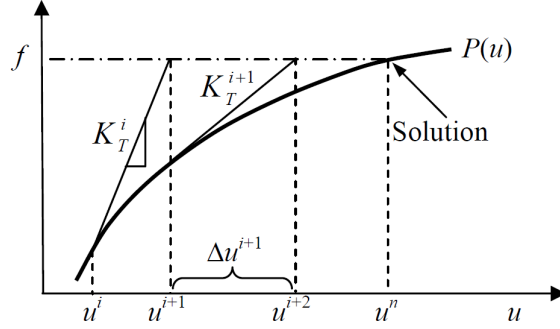


Figure 2.5: Newton-Raphson method for non-linear equation  $P(u) = f$  (image taken from [76]).

vector, which is the difference between the restoring forces (the loads corresponding to the element stresses) and the applied loads [8, 76]. ANSYS<sup>TM</sup> then performs a linear solution, using the out-of-balance loads, and checks for convergence. If convergence criteria is not satisfied, the out-of-balance load vector is reevaluated, the stiffness matrix is updated, and a new solution is obtained. This iterative procedure continues until the problem converges.

## 2.3 Image segmentation

This section presents an introduction for image segmentation. The description below is mainly based on the books by Gonzalez & Woods [61], Blake & Isard [24], the PhD dissertation of Bresson [26], and Lankton [81], and the technical memo of Ivins & Porrill [69]. We provide the mathematical background to perform active contour models and more particularly the implementation of the level set method. We will

then describe the specific active contour model developed by Lankton [81], that we implemented to perform medical image segmentation.

### 2.3.1 Active contour models

The process of segmentation is to split the image into meaningful parts. The result of image segmentation is a set of segments that collectively cover the entire image, or a set of contours extracted from the image. Each of the pixels in a region are similar with respect to some characteristics or computed properties, such as color, intensity, or texture. This is a necessary initial step for subsequent image processing tasks such as tracking, detection, object recognition, and shape analysis. When applied to a stack of images, typical in medical imaging, the resulting contours after image segmentation can be used to create 3D reconstruction.

Active contour models (snake) is one of the tools to proceed image segmentation. It is a variational method performing energy-minimization on curves that deform to fit the image features (see figure 2.6). Active contour models are typically driven by a potential energy generated by processing the image data, and this energy is minimized by iterative gradient descent. In addition, other energy sources can be implemented such as internal forces, producing tension and stiffness, or external forces, specified by human operator, constraining the behavior of the model. If the energy function is well chosen, the curve will come to rest when a meaningful segmentation has been achieved.

In this work, we consider that active contour model are regular parameterized closed curves. In  $\Omega \in \mathbb{R}^2$  a curve  $\mathbf{x}(s)$  parameterized by the parameter  $s$ , is a mapping:

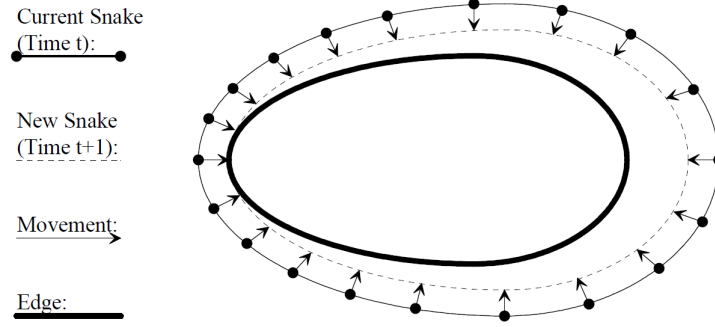


Figure 2.6: A Closed Active Contour Model: This diagram shows a snake with its ends enjoined so that it forms a closed loop. Over a series of time steps the snake moves into alignment with the nearest salient feature, here an edge (image taken from [69]).

$$\mathbf{x}: [a, b] \in \mathbb{R} \longrightarrow \Omega \in \mathbb{R}^2$$

$$s \longrightarrow \mathbf{x}(s) = (x_1(s), x_2(s))$$

A curve is regular if  $\forall s \in [a, b]$ ,  $\mathbf{x}'(s)$  exists and  $\mathbf{x}'(s) \neq 0_{\mathbb{R}^2}$ ; and is considered closed if  $\mathbf{x}(a) = \mathbf{x}(b)$  and  $\mathbf{x}(a) = \mathbf{x}(b)$ . Also as we mentioned earlier, active contour model is a moving curve, therefore active contour can be modeled by indexing an artificial parameter,  $t$ . The active contour motion between two time steps can be described by the following equation:

$$\mathbf{x}(s, t + \Delta t) = \mathbf{x}(s, t) + \frac{\partial \mathbf{x}(s, t)}{\partial t} \Delta t. \quad (2.16)$$

We define the vector field  $\vartheta : \mathbb{R}^2 \times \mathbb{R}^+$  describing the motion of each point along the active contour:

$$\frac{\partial \mathbf{x}(s, t)}{\partial t} = \vartheta(\mathbf{x}(s, t), t) \quad (2.17)$$



This vector field can be decomposed into a unique linear combination of the tangent and the inward normal normed vectors, respectively  $\mathbf{t}(s, t)$  and  $\mathbf{n}(s, t)$ :

$$\frac{\partial \mathbf{x}}{\partial t} = \langle \vartheta, \mathbf{t} \rangle \mathbf{t} + \langle \vartheta, \mathbf{n} \rangle \mathbf{n} \quad (2.18)$$

where  $\langle \cdot, \cdot \rangle$  is the inner product. Also, any motion in the tangent direction,  $\mathbf{t}$ , is equivalent to a re-parametrization of the curve, not resulting in any change of the curve. This term can be reduced to zero allowing only the normal component to contribute to the motion of the contour at each time step:

$$\frac{\partial \mathbf{x}}{\partial t} = \langle \vartheta, \mathbf{n} \rangle \mathbf{n} \quad (2.19)$$

We define the potential energy,  $E$ , of the active contour model such as it is only dependent on the geometric property of the contour (i.e.  $E(\mathbf{x})$ ), such an energy is said to be *geometric* [81]. The active contour model motion is driven by energy minimization of the curve using a gradient descent method on the following equation:

$$\frac{\partial \mathbf{x}}{\partial t} = \nabla_{\mathbf{x}} E = \langle -\nabla_{\mathbf{x}} E, \mathbf{n} \rangle \mathbf{n} \quad (2.20)$$

The advantage of geometric energies is that the behavior of the active contour,  $\mathbf{x}$ , is independent of any arbitrary choice of parameterization.

### 2.3.2 Level set methods

In order to implement active contour models, a choice needs to be made in order to describe the parametric representation of the curve. Initially most of the active contours used control points connected with spline. More recently, the level set

method for tracking moving fronts was introduced by Osher and Sethian in [99]. This method have had great success because it has been used in many applications from physics, by capturing multiphase fluid dynamic flow, to graphics such as special effects in Hollywood, visualization, image processing, computer vision, control, epitaxial growth, visibility, ray tracing, segmentation, restoration, and many others becoming the standard choice representation due to four advantages over the initial one [81]:

1. inherent support of topology change
2. natural representation of surface  $\mathbb{R}^N$
3. simple estimation of geometric properties
4. straightforward numerical implementation

The core idea in the level set method is to implicitly represent an interface  $\mathbf{x}$  in  $\mathbb{R}^2$  as a level set of a function  $\Phi : \mathbb{R}^2 \longrightarrow \mathbb{R}$ , called level set function, of higher dimension and compute the geometric characteristics and the motion of the front with this level set function. The level set function  $\Phi$  of the closed front  $\mathbf{x}$  is defined as follows:

$$\forall \mathbf{u} \in \Omega \subset \mathbb{R}^2 \quad \Phi(u) = \begin{cases} -d(\mathbf{u}, \mathbf{x}) & \text{for } \mathbf{u} \text{ inside } \mathbf{x} \\ 0 & \text{otherwise} \\ d(\mathbf{u}, \mathbf{x}) & \text{for } \mathbf{u} \text{ outside } \mathbf{x} \end{cases} \quad (2.21)$$

where:

$$d(\mathbf{u}, \mathbf{x}) = \inf_{\mathbf{v} \in \mathbf{x}} (\|\mathbf{u} - \mathbf{v}\|)$$

This representation provides a simple and smooth function, and the active contour can easily be recovered as:

$$\mathbf{x} = \{\mathbf{u} \in \Omega | \Phi(\mathbf{u}) = 0\} \quad (2.22)$$

In Fig. 2.7 several visualizations can be seen on two-dimensional curves and their corresponding signed distance function, from this figure it is obvious to observe that the level set method allows us natural curve topological changes, such as breaking or merging, while the level set function remains unchanged. It is worth to notice, that this representation can be extended to represent surfaces in  $\mathbb{R}^3$ . The geometric characteristics of the interface can be computed with the level set function, the unit normal,  $\mathbf{n}$ , and the mean curvature  $\kappa$  to  $\mathbf{x}(s, t)$  are given by:

$$\begin{cases} \mathbf{n} = -\frac{\nabla\Phi}{\|\nabla\Phi\|} \\ \kappa = \nabla \cdot \mathbf{n} = \nabla \cdot \left(-\frac{\nabla\Phi}{\|\nabla\Phi\|}\right) \end{cases} \quad (2.23)$$

The definition of the curvature is essentially used in the numerical implementation for regularization of the curve by penalizing high curvature. One can use the level set to represent the energy function (i.e  $E(\Phi)$  instead of  $E(\mathbf{x})$ ), therefore the equation to minimize 2.20 becomes:

$$\frac{\partial\Phi}{\partial t} = \nabla_{\Phi} E = \langle -\nabla_{\Phi} E, \mathbf{n} \rangle \mathbf{n} \quad (2.24)$$

deforming the curve  $\mathbf{x}$  implicitly, as  $\Phi$  is deformed. The definition of the energy function is key since it fuels the motion of the curve.

### 2.3.3 Energy functions

As we mention earlier, active contour models is a variational method that minimizes energy function of the curve. Two main categories of energy function exists: edge-based and region-based.

Edge-based active contour model, also known as the geodesic active contours model, was introduced by Caselles et al. [29]. It uses image gradients to identify object boundaries. Their approach is based on the relationship between active contours and the computation of minimal distance curves. The minimal distance curve lies in a Riemannian space whose metric is defined by the image content. An example of this type of energy is [81]:

$$E(\mathbf{x}) = \oint_0^L \Psi(\mathbf{x}(s)) ds, \quad (2.25)$$

where  $s \in [0, L]$  is a parameter chosen to correspond exactly with the length,  $L$ , of the active contour and  $\Psi$  is a weight function that reach the smallest value where strong edges exist within the image, commonly  $\Psi$  would be:

$$\Psi = \frac{1}{1 + |\nabla(G * I)|^2}, \quad (2.26)$$

where  $I$  represents the image,  $G$  represents a Gaussian smoothing kernel, and  $*$  represents the convolution operator. This approach assumes that the segmented object will display rapid change of intensity at the object boundaries. Edge-based segmentation only considers information at the contour, taking no consideration into the inside of the region segmented.

Zhu &Yuille [150] proposed a variational and statistical image segmentation model based on the snake model and the region-growing algorithm. Their main contribution

was the introduction of a region-based criterion into the snake model. Region-based method model images regions statistically and looks for an energy optimum where the model best fits the image. In these models the energy to minimize is:

$$E(\mathbf{x}) = \int_R f(u) du \quad (2.27)$$

where  $f$  is the function to minimize and  $R$  the region enclosed by the active contour in model  $\mathbf{x}$ . The advantage of such a method is its robust initialization and insensitivity to image noise. However this method can show some limits when segmenting non heterogeneous objects which often happens in medical imagery. Therefore to accurately segment medical images Lankton [81] developed a new hybrid class of active contour energies which utilizes local information and also incorporates the benefits of region-based techniques.

### 2.3.4 Localized active contour model

Lankton [81] developed a framework, where segmentation is based on information from local interior and exterior regions along the contour rather than global regions. This replaces the assumption that the foreground and background regions are distinguishable based on their global statistics by the assumption that interior and exterior regions will be different locally. The analysis of local statistics leads to the construction of a family of local regions at each point of the curve. Optimization of the local energy is achieved by motion of each point in order to optimize the energy added from its local region. Each point's component of the overall energy is computed by splitting the local neighborhoods into local-interior and local-exterior using the

evolving curve and a characteristic function.

Considering an image  $I$  defined on  $\Omega$ ,  $\mathbf{x}$  the active contour defined by the level set function  $\Phi$  such that  $\mathbf{x} = \{\mathbf{u} | \Phi(\mathbf{u}) = 0\}$  and the following smooth Dirac function specifying the curve:

$$\delta\Phi(\mathbf{u}) = \begin{cases} 1 & \Phi(\mathbf{u}) = 0 \\ 0 & |\Phi(\mathbf{u})| < \epsilon \\ \frac{1}{2\epsilon}(1 + \cos(\frac{\pi\Phi(\mathbf{u})}{\epsilon})) & \text{otherwise} \end{cases} \quad (2.28)$$

where  $\epsilon \ll 1$ . Using these notations Lankton [81] defined the energy function for a generic region-based function,  $f$ , as such:

$$E(\Phi) = \int_{\mathbf{u} \in \Omega} \delta\Phi(\mathbf{u}) \int_{\mathbf{v} \in \Omega} B(\mathbf{u}, \mathbf{v}) f(\Phi, I, \mathbf{u}, \mathbf{v}) d\mathbf{v} d\mathbf{u} \quad (2.29)$$

where  $B(\mathbf{u}, \mathbf{v})$  is a characteristic function defined by:

$$B(\mathbf{u}, \mathbf{v}) = \begin{cases} 1 & \|\mathbf{u} - \mathbf{v}\| \leq r \\ 0 & \text{otherwise} \end{cases} \quad (2.30)$$

with  $r$  as a predefined radius value. As we can see such a model will only consider the local region to compute the energy. An appropriate choice of the region-based function,  $f$ , could be the Yezzi et al. [148] model assuming that foreground and background regions should have maximally separate mean intensities, or the Chan-Vese [30] model assuming that the foreground and background are constant intensities represented by their means.

This PhD dissertation used an adapted version of Lankton [81] model implemented in Matlab<sup>TM</sup> [10] to segment breast MRI.

## 2.4 Mathematical tools element for tumor growth model

Mathematical modeling has a major role in the resolution of engineering and physical problems. It is therefore a valuable tool to be used for biological problems and more specifically to model the development of tumor growth models. Building a mathematical model for tumor growth will help clinicians obtain a better prognosis, plan a more effective treatment, validate experimental hypotheses on tumors, as well as understand or output relevant interaction phenomena at the microscopic and macroscopic level. An ideal tumor growth model should be a model that replicates reality with few relevant and easy to fit parameters that provide a good prediction and an understanding of behavior.

Cancer is a generic term for a large class of diseases that can affect any part of the body. There is a lot of controversy over how exactly cancer is initiated, but it is a generally accepted view that it requires several gene mutations to turn a normal cell into a cancer cell [89]. While normal cells will have typically controlled growth, due to these mutations, cancerous cells will allow cells to grow in an uncontrolled manner forming a tumor. Tumor cells will enter three main stages:

- Avascular stage
- Vascular stage
- Metastasis

The avascular stage corresponds to the phase where tumor cells acquire nutrients through diffusion from outside the tumor. After this initial stage the tumor will enter the vascular stage in which cells stimulate blood vessel production by secreting tumor angiogenesis factor. Finally the tumor will enter the metastasis stage in which the cell breaks free from normal control and begins to spread uncontrollably throughout the body. Each stage increases in complexity involving more entities from the environment, requiring more equations, more parameters, but mostly more sophisticated mathematical tools.

In this section we intend to give a small review of the three main categories of tools to model tumor growth. We will first describe the ordinary differential equation model to simulate the avascular tumor stage, then we describe the tumor model that will include greater complexity using either the partial differential equation or the cellular automata and agent-based model.

### 2.4.1 Ordinary differential equation model

Earliest tumor growth models considered no spatial variables, the growth was governed by a simple ordinary differential equation (ODE) [82, 88, 97]. At the initial stage, the avascular stage tumor faces no environmental limitations, for this reason using in-vitro data, it was well establish that the human tumor approximated exponential growth rates at their developmental stage. First intuitive tumor models only considered the number of tumor cells and described the growth equation given by the exponential:

$$n(t) = N_0 e^{\lambda t} \tag{2.31}$$



where  $n(t)$  is the number of tumor cells at time  $t$ ,  $N_0$  the initial number of cells, and  $\lambda$  is the growth constant. Such an equation is the solution of the following ODE:

$$\begin{cases} \frac{\partial n}{\partial t} &= \lambda n(t) \\ n(0) &= N_0 \end{cases} \quad (2.32)$$

Such a system implies that each cell divides and grows at a rate of  $\lambda$  with no restriction or limitation. However, the exponential function does not describe the rate of tumor growth *in vivo*, which will slow down when the tumor size increases due to the limited environment provisions and natural tumor cell degradation [149]. This required a more sophisticated equation allowing proliferation as well as degradation of cells. In the mid century Ludwig von Bertalanffy proposed a general form for such growth model, known as the *generalized Bertalanffy model* [94]:

$$\frac{\partial n}{\partial t} = an^\alpha - bn^\beta \quad (2.33)$$

with  $a$ ,  $b$ ,  $\alpha$ , and  $\beta$  parameters. In this set of equation if  $a$  and  $b$  are positive then the second term represents the loss of cells. The special case  $\alpha = 1$ ,  $\beta = 2$  gives the logistic equation, a widely used equation to model population growth. Such ODE model gives a first good model to simulate tumor growth [139, 94], in 1994 Olea et al. used this model as well as the Gompertz model to evaluate the growth rate of MCF-7 breast cancer multicellular spheroids [93].

In 1825 Benjamin Gompertz proposed an equation that was widely used as a growth curve for a biological model including various tumor growth models [79, 82, 149, 93, 86, 94]:

$$\frac{\partial n}{\partial t} = An + Bn \ln n \quad (2.34)$$

with  $A$  and  $B$  parameters. The solution of this equation is known as the Gompertz curve or Gompertz function, and fits better tumor dynamics. It is a type of mathematical model for a time series, where growth is slowest at the end of a time period:

$$n(t) = N_0 e^{\ln(\frac{N_\infty}{N_0})[1-e^{-bt}]} \quad (2.35)$$

where  $N_\infty$  is the plateau cell number which is reached at large values of  $t$  and the parameter  $b$  is related to the initial tumor growth rate. In Fig. 2.8 we can see *in vivo* tumor dynamics is best fitted by Gompertz's equation in comparison to a logistic equation.

Although this model gives a first good prediction, it appears that cancer is a complex disease and clinical data cannot possibly be described by a single set of growth parameters. Tumor cells almost certainly have different growth characteristics in different patients, individual micro-metastases, and within a single patient may have different growth parameters. To address this issue, more complex ODE model will incorporate some variation in the tumor growth by using distribution on growth parameters. Nonetheless tumor entering the vascular stage and metastasis requires a more sophisticated mathematical tool since they need to take into account the tumor environment. In particular this requires that the model includes spatial variables. And last but not least, ODE models only describes the tumor as a volume quantity, this leads mathematicians to assume only spheric tumors and radial progression [86], leading to the conclusion that ODE provides no information on a tumor shape itself. In the two next subsections we will describe models that fulfill these constraints using a partial differential equation, cellular automaton, or agent-based model. We

will first describe continuous tumor growth models using partial differential equation (in subsection 2.4.2) then we will look into a discrete growth model using cellular automaton and agent-based models (in subsection 2.4.3).

## 2.4.2 Partial differential equation model

In order to bring tumor growth models to another level, it is key to consider the spatial environment. Indeed modeling tumor volume through ODE is useful to understand the growth rate but this does not provide spatial information on tumors. Partial differential equations (PDE) are a type of differential equation of several independent variables and their partial derivatives with respect to those variables, they allow the incorporation of the spatio-temporal model. In 1972, Greenspan was the first to implement spatial variable proposing a diffusion-limited growth model for tumors [62]. More recently Byrne & Chaplain [27] developed a growth model limited by the influence of inhibitors. Today there are an extensive use of tumor growth models using complex PDE, simulating multi-species of cancer cells [145], giving predictions to drug responses [46, 114], or simulating microscopic and macroscopic effects by developing multiscale models [113, 25, 23, 45].

The importance of including spatial variables was key in order to efficiently use clinical tumor growth models. The Swanson et al. [129, 130] model was a pioneer example: developing a simple diffusion model used for the clinical outcome of brain tumors. They proposed a mathematical model of gliomas based on proliferation and diffusion rates to incorporate the effects, reported by Giese et al. [60], of augmented cell motility in white matter as compared to gray matter. The model defined the

evolution of the glioma cell population solely by proliferation and diffusion. In this model the rate of change of tumor cell density is equal to the diffusion (motility) of tumor cells plus the growth cell division of tumor cells. Lets consider a domain  $\Omega$  ( $\subset \mathbb{R}^2$  or  $\mathbb{R}^3$ ), if we let  $c(\mathbf{x}, t)$  be the number of cells at any position  $\mathbf{x} \in \Omega$  and time  $t$ , such a model can be written mathematically as a reaction-diffusion equation:

$$\frac{\partial c}{\partial t} = \nabla \cdot (\mathbf{D}(\mathbf{x}) \nabla c) + \rho c \quad (2.36)$$

where  $\rho$  (1/day) represents the net rate of growth of cells including proliferation and death (or loss),  $\mathbf{D}(\mathbf{x})$  ( $\text{cm}^2/\text{day}$ ) is the diffusion coefficient map of cells in brain tissue, and  $\nabla$  represents the spatial gradient. The diffusion term  $\mathbf{D}(\mathbf{x})$  depends on the space variable in order to take into account the heterogeneity of brain tissue. If we consider a simple case where  $\mathbf{D}(\mathbf{x}) = D_1$ , a constant  $\forall x \in \Omega$ , we can break down equation 2.36 in an explicit way by time:

$$c^{n+1} = c^n + \Delta_t (D_1 \nabla^2 c^n + \rho c^n) \quad (2.37)$$

with  $\Delta_t$  the discrete time step. If we consider  $\Omega \subset \mathbb{R}^2$ , using the finite difference numerical method to discretized the two-dimensional diffusion term (assuming a uniform spatial discretization  $h_x = h_y = h$ ) we get:

$$(\nabla^2 c)_{i,j} = \frac{1}{h^2} (c_{i,j+1} + c_{i,j-1} + c_{i+1,j} + c_{i-1,j} - 4c_{i,j}) \quad (2.38)$$

Compiling equation 2.37 and 2.38 we obtain the following:

$$c_{i,j}^{n+1} = c_{i,j}^n + \frac{\Delta_t D_1}{h^2} (c_{i,j+1}^n + c_{i,j-1}^n + c_{i+1,j}^n + c_{i-1,j}^n - 4c_{i,j}^n) + \Delta_t \rho c_{i,j}^n \quad (2.39)$$

Such a simple model appears to be very useful and provides the potential of a direct clinical implication: as we can see in figure 2.9 Swanson et al. performed simulation

of real patient brain tumor and mapped it on the patient brain CT (computed tomography) scan.

As mentioned earlier a wide range of tumor models are using PDEs to simulate cancer proliferation at the avascular and vascular stage, as well as angiogenesis and metastasis phenomena. PDEs appear to be a powerful tool to simulate tumor growth, however such a tool will usually consider tumors as a global entity/density in comparison to considering each cell as an individual or a group of individuals, a property that cellular automata and agent-based models are able to provide.

### **2.4.3 Cellular automata model**

Cellular automata (CA) and agent-based modeling (ABM) are two methodologies widely used to simulate tumor growth. CA consists of discrete agents or particles, which occupy a grid of specified shape with one or more discrete or continuous internal state variables. A set of rules describes the evolution of their state and position depending on the current state of the particle and those of neighboring particles. These rules may either be discrete or continuous in the form of deterministic, probabilistic rules, or ODEs. These rules can be manipulated to obtain well known continuous PDEs such as the diffusion equation, or discrete logical interactions of simple Boolean system [14]. One motivation for using CA is the enormous range of length scales demonstrating the typical biological phenomena. Organisms may contain dozens of organs composed of tissues containing tens of billions of cells. This allows the model the flexibility to treat more realistically complex situations. ABM is defined in a similar way, it is a system modeled as a collection of autonomous

decision making entities called agents. Each agent individually assesses its situation and makes decisions on the basis of a set of rules.

CA for tumor growth models was first used in 1985 by Duchting and Vogelsaenger [37] to simulate aspects of tumor growth and therapy. These automaton rules were designed to reflect nutritional needs for tumor growth. Other important factors, such as surrounding cells and mechanical pressure, however, remained unconsidered. Qi et al. [107] considered a two-dimensional cellular automaton tumor model that reproduced idealized Gompertz results. The model only allowed cells to divide if one of their nearest neighbors was empty. More recently, Kansal et al. [74, 73] have developed a CA for avascular tumor growth on a Voronoi lattice, with each of their new automaton cell taking the form of a polyhedra in a three-dimensional space. The use of this type of lattice preserves the discrete nature of cells but removes the anisotropy introduced by the use of a regular lattice. Patel et al. [104] have developed a CA model to study the role of acidity in tumor growth. Tumor-induced angiogenesis has also been modeled using a CA approach coupled with PDEs [16, 87]. CA and ABM remain an excellent tool to simulate tumor growth, although the bottleneck of such a method could have been the clinical implementation/application due to the necessity of individual element initialization. Macklin et al. [83, 84] recently developed an ABM of a ductal carcinoma patient calibrated thanks to breast biopsy. This recent breakthrough gives a first direct clinical application and opens up great opportunities for CA and ABM tumor growth model to be implemented for clinical use.

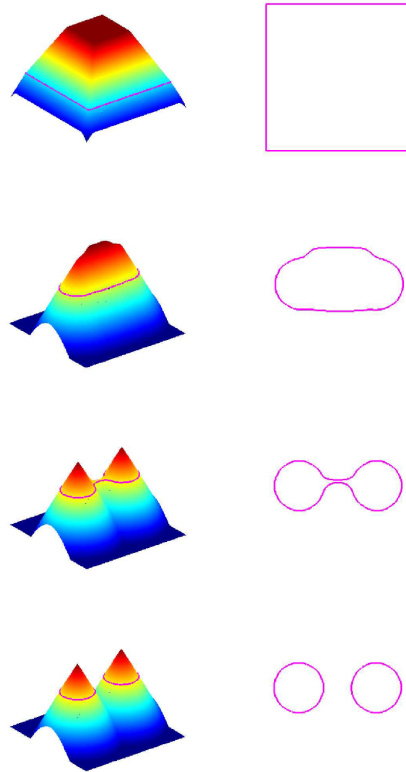


Figure 2.7: Natural changes of topology in the level set framework. The right column presents the evolution of the curve and the left column shows the evolution of the associated level set function. We note that the curve changes its topology but not the level set function. (image taken from [26]).

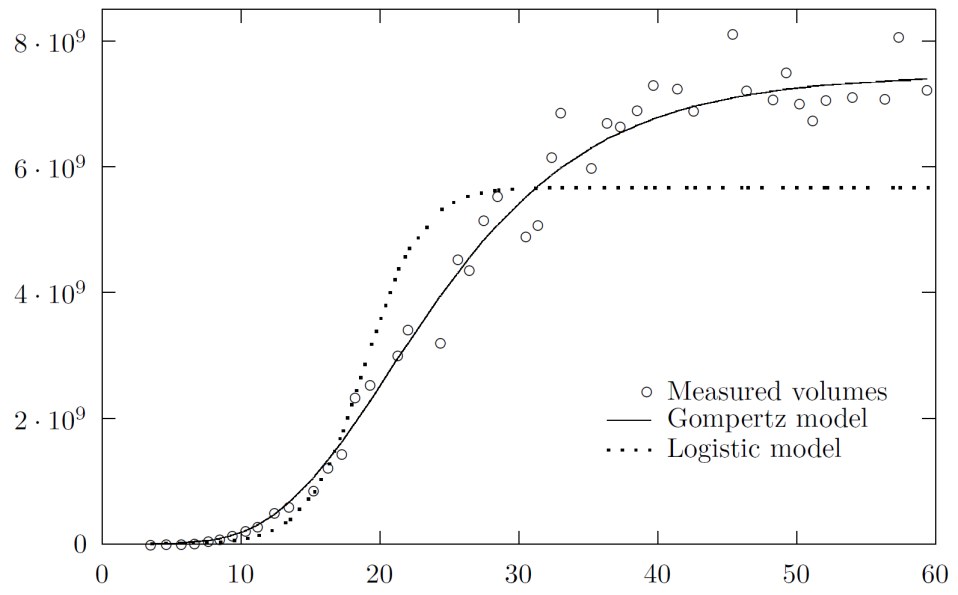


Figure 2.8: Best-fit curves by Gompertz and logistic models with *in-vivo* results of tumor growth volumes in  $\mu m^3$ / time in days) (image taken from [86]).



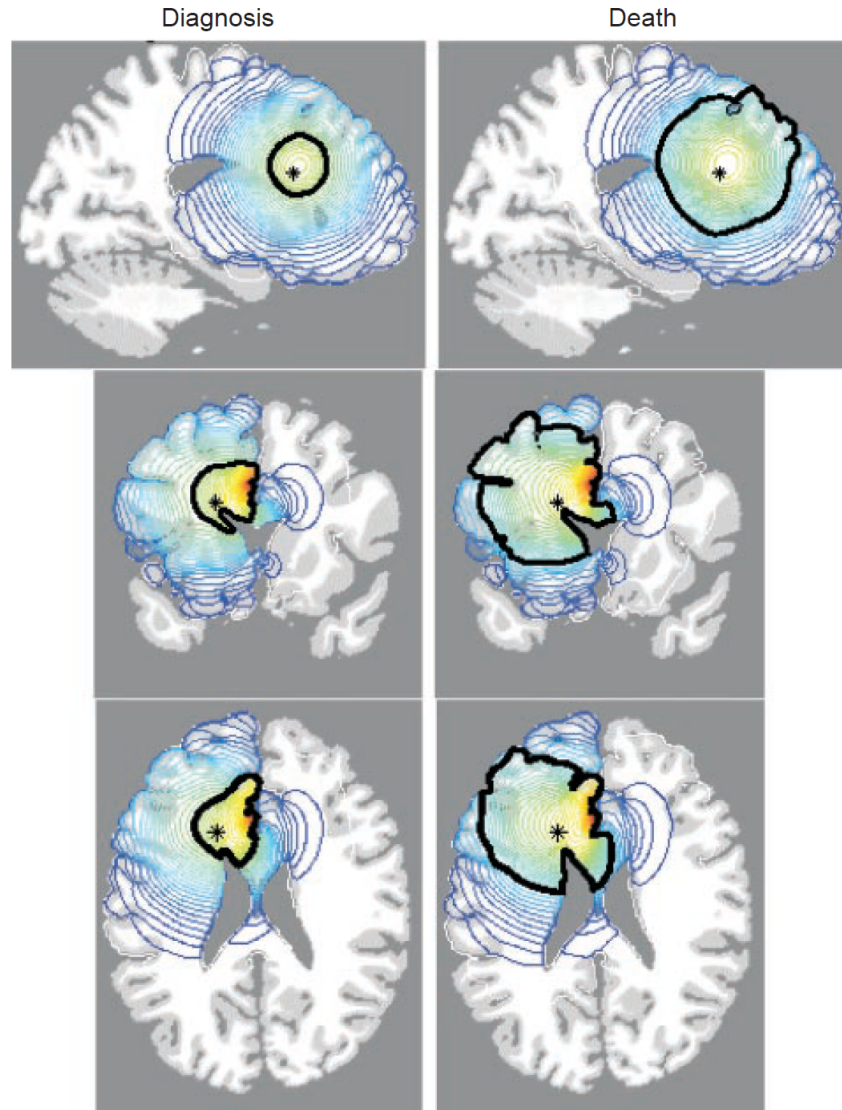


Figure 2.9: Sections of the virtual human brain intersecting the site of the glioma originating in the superior frontal region denoted by an asterisk (\*). The left column of brain sections corresponds to the tumor at diagnosis whereas the right column represents the same tumor at death. Red denotes a high density of tumor cells while blue denotes a low density. A thick black contour defines the edge of the tumor detectable by enhanced CT. Cell migration was performed in a truly three-dimensional solid representation of the brain. The elapsed time between diagnosis and death for this virtual glioma is approximately 158 days. (image taken from [130]).

## Part II

### Tumor growth modeling

In 2011, the American Cancer Society [2] estimated 230,480 new cases of invasive breast cancer will be diagnosed among women, as well as an estimated 57,650 additional cases of in situ breast cancer. The majority of in situ breast cancers are DCIS, which accounted for about 83% of in situ cases diagnosed during 2004-2008. While DCIS in itself is not considered by clinicians as a tumor, it has the potential to turn into an invasive carcinoma. In fact it was suggested by Page et al. [101] that 28% of women presenting DCIS will develop invasive carcinoma in a follow-up period of approximately 15 years. This study was consolidated by similar reports more recently [75, 124] suggesting that DCIS is a potential precursor for invasive carcinoma. Hence, an understanding of the DCIS behavior and potential to progress into an invasive carcinoma will help the patient avoid over-treatment.

Until a quarter century ago, a mastectomy was the only surgery option. The 1980s brought considerable advances in lumpectomies and other forms of BCT, and have been increasingly utilized in the US. Today in the US patients diagnosed with DCIS are more likely to choose lumpectomy over mastectomy. One of lumpectomy's shortcomings is the evaluation of tissue to resect: it is reported that at least 10% of DCIS treated by lumpectomy result in a negative margin, requiring patient to undergo a re-excision surgery [36, 31, 28]. Another shortcoming of the lumpectomy procedure when treating DCIS is the potential risk of local recurrence at the same location. Studies reported a local recurrence around 27% for lumpectomy, and approximately 10% for lumpectomy if followed by radiation therapy, other studies reported a lower risk of local recurrence for greater excision margin [103]. It is more likely that these recurrences occur due to residual cancerous cells left after surgery. This shows the

importance of a thorough evaluation of the tumor in terms of shape and size as well. We believe that these shortcomings could be solved by building a tumor growth model for breast cancer, allowing clinicians to be able to estimate the size and shape as well as understanding the potential invasiveness of the tumor.

This part focuses on developing a tumor growth model adapted for breast cancer and more particularly DCIS. We build a continuous model using PDEs. Our model is a multiscale simulation taking into account macroscopic and microscopic environmental phenomena. We will first give an introductory chapter (chapter 3) where we extend a description of DCIS biology in section 3.1, detailing some specific DCIS abnormalities (in section 3.2), we will conclude chapter 3 with a literature review of a tumor growth model developed for breast cancer (section 3.3). In chapter 4 we present the multiscale tumor growth model adapted for breast cancer that we developed. Finally chapter 5 concludes part II, presenting and discussing some results of our tumor growth model and discussing the potential improvements to the model.

# Chapter 3

## Biology model

### 3.1 Ductal carcinoma in situ (DCIS) pathology

DCIS is the grouping of the whole family of intraductal tumors and was introduced in subsection 2.1.2. Since it is not an invasive lesion, DCIS are not usually recognized as a type of cancer. Nevertheless due to its potential to progress into an invasive carcinoma DCIS are classified as having a cancerous pathology. Among the medical community there is still debate on whether DCIS can be classified into two groups, invasive or non-invasive, or whether all DCIS are non invasive at first and mutations lead DCIS to progress into an invasive carcinoma.

In terms of pathology DCIS can be classified in different types, these classifications are made through observation of the DCIS tumor under the microscope after a biopsy. This classification divide DCIS into two groups:

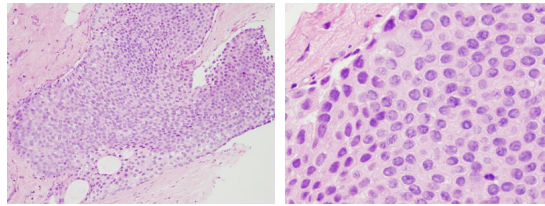


Figure 3.1: Solid DCIS sample: (left) general view; (right) zoomed on a fern like projection. Picture taken from [1]

- **The non-comedo types:** The term non-comedo is suggesting that there are not many dead cancer cells, necrosis, in the tumor. This is often associated with the hypothesis that the cancer is growing slowly, and that there is enough nutrients to feed all of the cells. Pathologists sub-divide non-comedo DCIS into 3 class:
  - **Solid DCIS:** cancer cells completely fill the affected breast ducts, see figure 3.1;
  - **Cribiform DCIS:** cancer cells do not completely fill the affected breast ducts; giving birth within the tumor to distinctive holes in between the cancer cells, making it look like Swiss cheese see figure 3.2;
  - **Papillary and micropapillary DCIS:** the cancer cells arrange themselves in fern-like projections of cells into the center of the duct; micropapillary type projections are smaller than the papillary type see figure 3.3 for micropapillary DCIS.
- **The comedo type:** Comedo-type DCIS tends to be more aggressive than the non-comedo types of DCIS. Pathologists are able to easily distinguish between

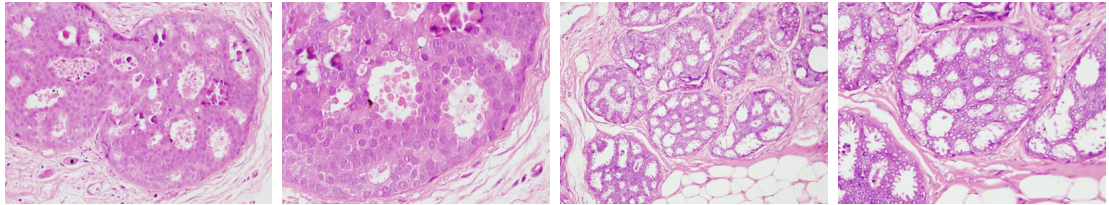


Figure 3.2: Cribiform DCIS sample. Pink represents the tumor cells and white spots represents the non tumor area (lumen). Picture taken from [1]

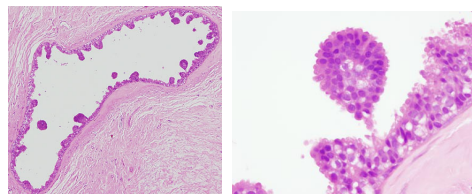


Figure 3.3: Micropapillary DCIS example: (left) general view; (right) zoomed on a fern like projection. Pink represents the tumor cells and white spots represents the non tumor area (lumen). Picture taken from [1]

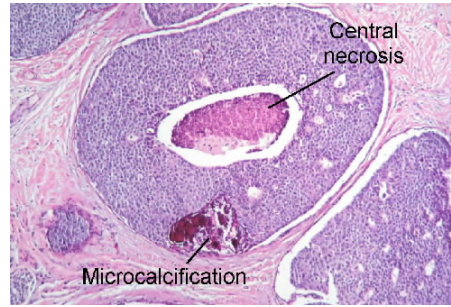


Figure 3.4: DCIS - comedo type with microcalcification [4]

comedo-type DCIS and other non-comedo types when examining the cells under a microscope because comedo-type DCIS tend to plug the center of the breast ducts with necrosis (dead cells). When necrosis is associated with cancer, it often means that the cancer is able to grow quickly. Necrosis is often seen with microcalcifications (tiny calcium deposits that can indicate cancer). Figure 3.4 is the perfect illustration of such DCIS type.

Presence of comedo and non-comedo DCIS is not directly linked with the potential invasiveness of DCIS. Necrosis also depends on the tumor neighborhood environment, a poor nutrition environment could easily lead to comedo DCIS types, with this tumor being a fast growing tumor. It is generally accepted that comedo DCIS tends to be more aggressive. In the next section we will give a description of DCIS pathology and mechanisms that lead to carcinoma. This section is key in order to correctly build our growth model.



## 3.2 DCIS abnormality

DCIS is a heterogeneous entity with a wide range of morphological appearances, leading to different growth patterns. This unbalanced growth phenomena is initiated by the overexpression of oncogenes and underexpression of tumor suppressor genes. Most of the time estrogen and progesterone receptors (ER and PR) or the oncogene products (HER2) are expressed in DCIS. As a matter of fact studies [43] suggest that 2 main groups could be obtained from DCIS lesions:

- low nuclear grade that is commonly ER-positive and characterized by a loss of genetic material on chromosome 16q
- high nuclear grade, ER-negative and HER2 positive that show more complex genetic changes including gains on chromosomes 8q and 17q.

Although it was observed that high nuclear grade and HER2-positive lesions are likely to be larger than low nuclear grade HER2-negative lesion, Erbas et al. suggested in his review [43] that this could be directly linked to the duration of follow up, and simply translate the fact that the growth rate of the former type of lesions are more aggressive.

DCIS abnormalities occur either by accumulations of DNA mutations or hereditary mutations. It is understood that these transformations occur in stages. Poor grade DCIS generally maintain their basic cell proper configuration, in particularly their polarity and an anisotropic distribution of surface adhesion receptors, resulting in finger like growths into the lumen (papillary or cribriform type). In solid-type DCIS,

the cells lack polarity and the micro-structures are lost. Cells will proliferate until they fill the lumen. In this case it appears that the nutrients and growth factors will act as a growth limiting factor. The lack of nutrients will give birth to a necrosis region, usually in the core of the tumor. We will highlight later how our tumor growth model will successfully show this behavior.

Although factors leading to DCIS are understood, the natural history of DCIS remains unclear. One of the reasons for this is that current procedure to treat DCIS is an immediate surgical removal of the lesion. While by definition, DCIS arises first in epithelial cells, whether all ductal cancers go through a prolonged, potentially detectable phase of in situ cancer or whether some cells rapidly invade the surrounding stroma is unknown. Unlike other types of cancer there is a debate about whether in situ breast cancer is an obligate precursor of invasive breast cancer, and what proportion of in situ breast lesions progress to an invasive cancer[43]. Although there is a debate today, DCIS is often regarded as an important precursor of invasive ductal carcinoma (IDC), where a more elaborate gene mutation leads the tumor to extended motility and the secretion of matrix-degrading enzymes. This leads to a deterioration of the basement membrane (BM), leading to an invasion of the surrounding stroma. Erbas et al. [43] illustrates in figure 3.5 a possible model for the different outcomes of a DCIS lesion. After initiation within the duct epithelial cells, Erbas et al. suggested four different scenarios that may happen in an unknown proportion of cases:

- (a) it rapidly becomes invasive without a prolonged DCIS phase. Such rapid invasion could occur due to mutations in critical genes during the initiation phase of the tumor. For instance BCRA1 tumors are rarely associated with in situ

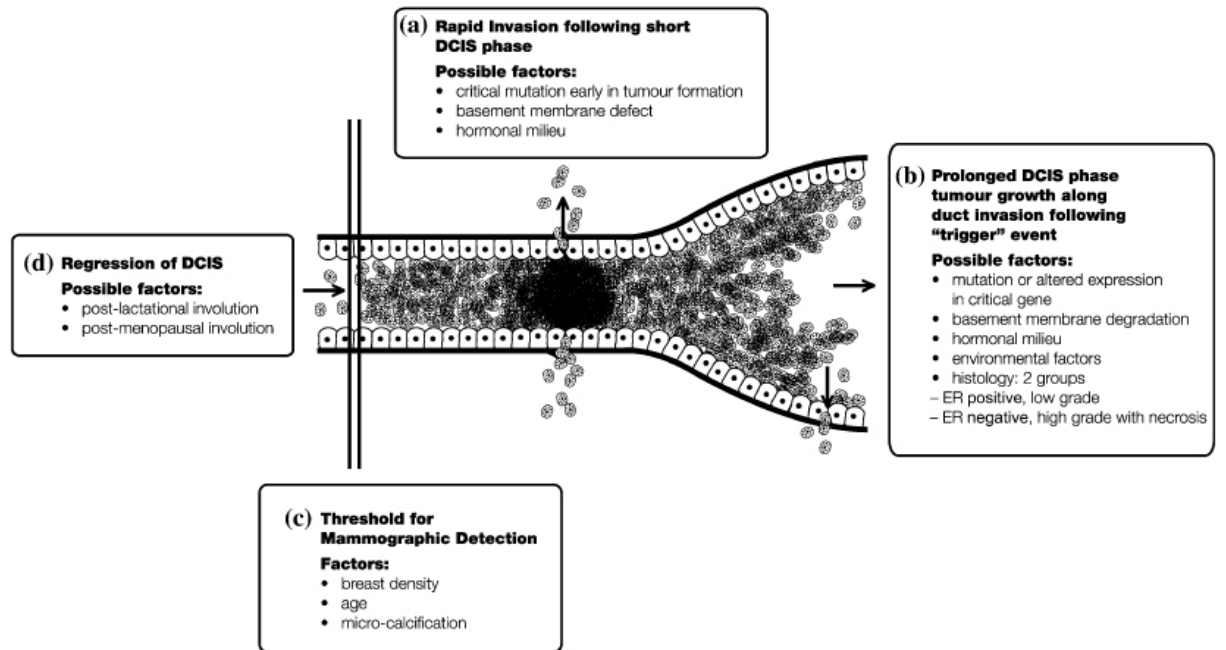


Figure 3.5: Possible pathways for the natural history of DCIS. Cross section of a breast-duct. Figure taken from [43]

carcinoma and could be an example of this type of progression.

- (b) it spreads along the duct and has a prolonged DCIS phase that could even be a dormant phase, till it witnesses a trigger event such as a critical gene mutation leading to the invasion of the BM.
- (c) it spreads along the duct and has a prolonged DCIS phase till it reach a detectable size by mammography.
- (d) it undergoes a regression for example following post-lactational or post-menopausal involution.

### 3.3 DCIS modeling-related work

A wide range of tumor growth models specifically adapted to breast cancer has been submitted using various kind of mathematical tools such as ODEs, PDEs, CA, and ABM. In 2004, Xu [147] adapted a nutrition diffusion limited model [27], including a rigid duct wall radially symmetric to study DCIS. Xu showed that the spatial patterns associated to the stationary solutions of his model were consistent with morphology commonly observed in DCIS (for instance cribriform and comedo). Their model only took into account one uniform cell density. Later, Franks et al. [50, 49, 51] proposed a model of DCIS growth that took into account the local mechanical environment. They illustrated a model where DCIS will grow and deform the duct wall. Their model took into account two types of cells, necrosis and proliferant, and cell motion governed by advection. In order to understand the progression of DCIS to an invasive carcinoma, the model included secretion of matrix-metalloproteinase (MMPs) enzymes, responsible for wall degradation. Their results suggest that the elevated pressure accompanying tumor growth, can in addition to deforming the basement membrane, stimulate MMP enzyme production near the duct wall. Enderling et al. [39, 40, 41] provided a mechanism explaining why breast cancer recurs in a certain percentage of women even after surgical treatment and standard radiotherapy treatment. They suggested that this could be due to the presence of a tumor suppressor gene having a Lost in Heterozygosity (LOH - only one mutation of the tumor suppressor gene), which were considered in their model as invulnerable to radiotherapy. Another study developed a three-dimensional CA model of DCIS pathology. The author [68] considered a stochastic mutation differentiating four different levels of

carcinoma cells. The model did not include a mechanical law to govern cell motion. In 2011, Kim et al. [77] proposed a very complete multiscale model. They were able to study the effect of mechanical properties of the tissue environment on tumor progression as well as the tumor micro environment influence on growth.

Of particular interest to investigators is the ability to reproduce particular micro-structure shapes observed in DCIS. Rejniak et al. [112] proposed a cell-based model, implementing continuum mechanics, reproducing similar micro-structure shapes observed in DCIS. This was achieved due to a polarized arrangement of cells. However their model did not consider different types of cell death such as necrosis or apoptosis, as well as growth limiting factors such as nutrients or growth factor dependence. More recently, Norton et al. [91] proposed a two-dimensional discrete model that implemented mechanical effects such as cellular adhesion, duct wall resistance, as well as biological features such as apoptosis, necrosis, and cell polarity. They were able to successfully reproduce micro-structure features observed in DCIS as we can see in Fig. 3.6.

In an area of personalized medicine, the ultimate golden model will deal with clinical application using patient specific data providing personalized therapy. Macklin et al. [48] brought the first step into this new path for breast cancer treatment. They designed a patient specific calibration ABM for DCIS. The model encompass a wide range of features for each cell: quiescent state, proliferate state, apoptosis state, necrotic state, and calcified debris. Cells are submitted to drag force as well as interaction forces: cell-cell adhesion, cell-BM adhesion, (calcified) debris-(calcified) debris adhesion, cell-cell repulsion, and cell-BM repulsion; cell motion is induced by

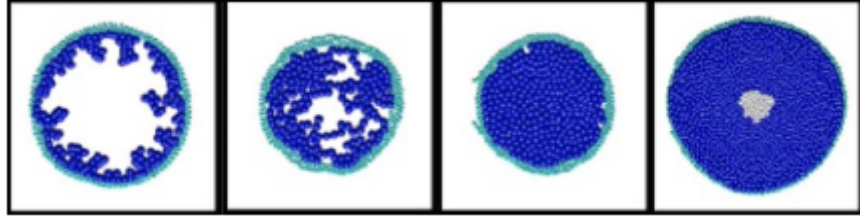


Figure 3.6: Results taken from Norton et al. work [91], from left to right: micropapillary structures, cribriform pathology, solid comedo, non-comedo. In the simulations, the green cells represent myoepithelial cells, the blue cells represent the tumour cells and the gray cells represent the necrotic cells.

the equilibrium of these competing forces. The proposed model was calibrated with help from to formalin-fixed, paraffin-embedded (FFPE) patient tissue. Validation of the model was made by comparing the apoptotic index (AI), the proliferative index (PI), the viable rim thickness, the density in the viable rim, the general tumor morphology, and the spatial distribution. Their model was able to successfully reproduce a comedo DCIS type without the viable rim observed in patient data. They suggested that cell adhesion protein model and speed of cell burst is the reason for this and suggested that in their future work they will adapt the model to fit these observations. This model brings a great contribution to the discipline, inspiring a new era of model targeting clinical applications. We believe that the limitation of their model resides in the use of individual ABM for each cell, requiring a fastidious initialization that cannot, today, satisfy the purpose of personalized treatment. We strongly believe that continuum models can adjust this issue and provide the best fit for clinical solutions. Indeed, although they agglomerate multiple phenomena into a

single parameter they require a significantly lower load of work regarding the calibration and initialization.

We are going to build a continuum tumor growth model using PDEs to simulate DCIS growth. This model will be multiscale including a macroscopic and microscopic phenomena. The purpose of this model will be to include the maximum relevant feature as well as making sure that it can easily be fit for clinical application.

# Chapter 4

## Mathematical model

In this dissertation we build a multiscale mathematical model of DCIS regulated by HER over-expression which represents 30% of DCIS cases. This, allows us to study the impact of HER over-expression on the growth rate using the HER chemical reactions described by Eladdadi and Isaacson's work [38]. This model will be a nutrient-limited growth model, involving the surrounding fluid inside ducts (lumen), healthy cells, proliferant, and dead tumor cell concentrations. The model is embedded in a macroscopic model based on Darcy's law to describe spatial tumor dynamics. The model will enable tumor cells to secrete the MMP enzymes giving the potential for the tumor to progress into an invasive carcinoma. A simplified illustration of the following model description is plotted in figure 4.1. This mathematical model was computed using the numerical toolbox developed by the INRIA MC2 team in Bordeaux [66]. In the following sections we are going to give a detailed description of our model.



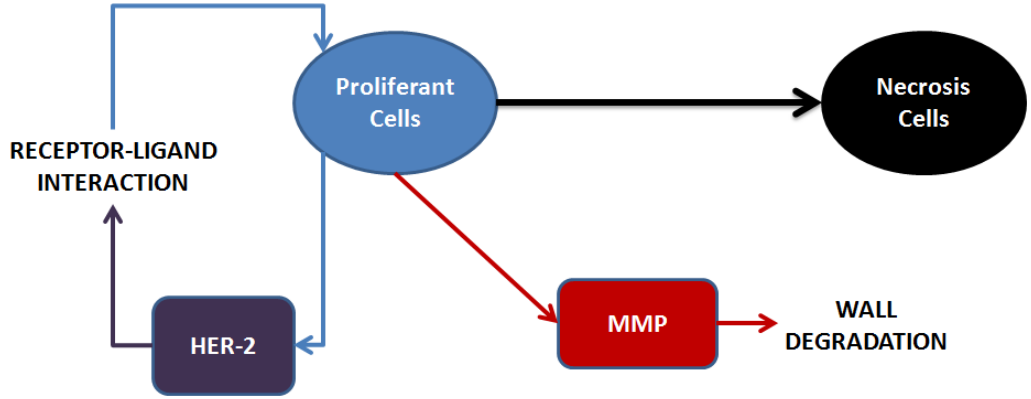


Figure 4.1: Tumor growth model

## 4.1 Environmental conditions

In our model we considered four types of entities: healthy cells, lumen filling the duct, proliferant cells, and necrosis cells. The cycle of reproduction for healthy cells being negligible in comparison to tumor cells, in this model only tumor cells divide, also only tumor cells are subject to death.

Let's consider  $\Omega(\subset \mathbb{R}^2, \mathbb{R}^3)$  the computation domain. Let the concentration (i.e. the volume fraction), at position  $\mathbf{x} \in \Omega$  and time  $t$ , of healthy tissue, lumen, live tumor cells, and dead tumor cells be represented respectively by  $S(\mathbf{x}, t)$ ,  $L_u(\mathbf{x}, t)$ ,  $P(\mathbf{x}, t)$ , and  $N(\mathbf{x}, t)$ . We denote by  $\mathbf{v}_S$ ,  $\mathbf{v}_{L_u}$ ,  $\mathbf{v}_P$ ,  $\mathbf{v}_N$  as their respective internal velocity field. We denote the rate of change of proliferant cells,  $P$ , inside the domain equal to the birth rate of new cells minus the death rate of tumor cells, similarly we quantify the rate of change of the necrosis population,  $N$ , equal to rate of death of proliferant cells.

The continuity equations governing these quantities are then:

$$\begin{cases} \partial_t P + \nabla \cdot (\mathbf{v}_S S) &= (f_P - f_{PN}) \alpha P \\ \partial_t N + \nabla \cdot (\mathbf{v}_N N) &= (0 + f_{PN}) \alpha P \\ \partial_t S + \nabla \cdot (\mathbf{v}_S S) &= 0 \\ \partial_t L_u + \nabla \cdot (\mathbf{v}_{L_u} L_u) &= 0 \end{cases} \quad (4.1)$$

where  $f_N$  is the birth rate,  $f_{PN}$  the death rate, and  $\alpha$  is a positive constant. We assumed that tumor cells, healthy cells, and lumen form an incompressible fluid with no voids present; the sum of these concentrations will always be equal to one:

$$S + L_u + P + N = 1 \quad (4.2)$$

Motion of the system defined is driven by the birth of new cells in  $\Omega$ , therefore we assume that cells are passive and move at the velocity of the “surrounding fluid”  $\mathbf{v}$ :

$$\mathbf{v} = \mathbf{v}_S = \mathbf{v}_{L_u} = \mathbf{v}_P = \mathbf{v}_N$$

Using this equality, we sum up the system in eq. 4.1 and plug in eq. 4.2, we obtain a condition on the velocity:

$$\nabla \cdot \mathbf{v} = \alpha f_P P \quad (4.3)$$

The divergence of the velocity field is non-negative. This corresponds to an increase of the volume of the tissue and will create a movement of the cells from the center of the domain to the boundary. Entities at the boundary of the domain are therefore pushed out through the boundary.

The death of cells is triggered when cells face a lack of oxygen concentration,  $\Theta$ . If this concentration is below a particular threshold value,  $\Theta_N$ , the proliferating cell will die permanently, hence we define  $f_{PN}$  :

$$f_{PN} = \begin{cases} \tanh(K_p(\Theta - \Theta_N)) & \text{if } \Theta < \Theta_N \\ 0 & \text{otherwise} \end{cases} \quad (4.4)$$

where  $K_p$  is a positive constant. This function always remains positive, representing the permanent state of a necrosis cells.

In this model, a proliferant cell is assumed to be HER-2 positive, over-expressing a high level of HER-2 protein, and the proliferation of cells is regulated by a chemical process involving HER-2 entity. The chemical reaction process will be detailed later, for now we know that the outcome of this chemical reaction is a ternary complex, labeled as  $[T]$ , that weighs the proliferation rate. The proliferation function,  $f_P$ , from equ. 4.1, of the HER-2 positive nutrient growth-limited tumor model is then defined by:

$$f_P = \begin{cases} \frac{[T]}{\alpha_T + [T]} \tanh(K_p(\Theta - \Theta_N)) & \text{if } \Theta > \Theta_N \\ 0 & \text{otherwise} \end{cases} \quad (4.5)$$

where  $\alpha_T$  is a positive constant. As demonstrated, our model considered two factors regulating the proliferation of cells: (1) oxygen provision, and (2) the ternary complex signaling due to HER overexpression. We will investigate in the next two sections these regulating factors.

## 4.2 Nutrients distribution

Our model considered the oxygen entity,  $\Theta$ , as the unique element for nutrition cells. From previous equations, our model considered oxygen essential to the division of cells as well as for surviving. Indeed if the oxygen concentration is lower than  $\Theta_N$ ,

our model states that cell starts necrosing at a certain rate.  $\Theta_N$  can be interpreted as a hypoxia threshold. We considered that oxygen molecules are much smaller than cells, and therefore are not affected by the motion created by mitosis of the “surrounding fluid” velocity. Instead, the oxygen undergoes a diffusion process. Since the diffusion process occurs on a much smaller time scale than the cellular division, the adiabatic approximation was considered, assuming that the equilibrium is reached instantaneously. Let’s consider  $O \subset \Omega$  the source of oxygen, this could be a network of blood vessels for instance, collecting these assumptions we can write the following elliptic equation on  $\Theta$ :

$$\left\{ \begin{array}{ll} -\nabla \cdot (K_{diff} \nabla \Theta) = -\phi P \Theta & \text{on } \Omega \setminus O, \\ \Theta = \Theta_0 & \text{on } \partial\Omega, \\ \Theta = \Theta_{max} & \text{on } O. \end{array} \right. \quad (4.6)$$

With  $\phi$  being the rate of consumption by the proliferating cells, and  $K_{diff}$  the coefficient of diffusion. Note that  $\Theta_{max}$  is the concentration of oxygen in the blood, while  $\Theta_0$  is some reference value needed for the computation on the external boundary of the computational domain.

*Remark: For the sake of simplicity, we have considered that healthy tissue does not uptake nutrients (since their consumption is smaller than one of the proliferative cells). However it could be easily added in the model if necessary through Eq. 4.6.*

## 4.3 HER overexpression

In this section we first review the HER overexpression model defined by [38]. Eladdadi and Isaacson [38] developed in 2008 a model based on ODE, to simulate cancer cell population growth. They studied the impact that HER overexpression had on growth rates. To our knowledge this work is the only one that involved chemical interactions for breast tumor growth model, however this model being an ODE based model, did not take into account spatial dependence. Our goal is to produce a breast tumor growth model based on chemical interaction specific to the breast and rewrite it as a multiscale model. Therefore we will first describe Eladdadi and Isaacson's work [38], in order to fully understand the chemical interaction they simulate, and embed this model into our multiscale tumor growth model in subsection 4.3.2.

### 4.3.1 Eladdadi and Isaacson model

Their model considered a homogeneous population of  $P$  cells distributed throughout a medium that contains a large amount of EGF ligands. A monovalent EGF ligand (L) binds reversibly to a monovalent cell surface EGF receptor (R) with forward and reverse rate constants  $k_f$  and  $k_r$ , respectively to form a receptor-ligand EGFR-EGF complex (C). The occupied receptor then hetero-dimerizes with a cell surface HER2 receptor with coupling and uncoupling rate constants  $k_c$  and  $k_u$ , respectively to form a dimer or ternary complex EGF-EGFR-HER2 (T). The schematic representation of a simple ternary complex model (receptor-ligand-receptor) is shown in figure 4.2.

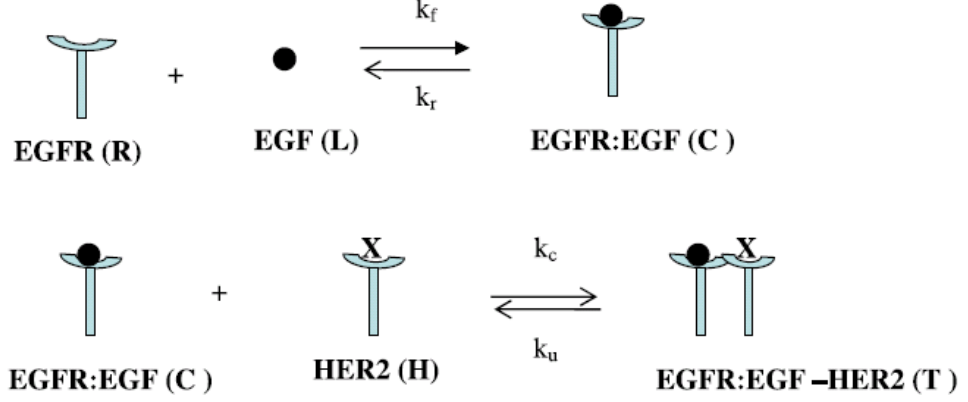


Figure 4.2: Simple ternary complex model (image modified from [38])

Their model can be represented by the following chemical reaction :



Using the law of mass action, they derived the following differential equations describing the time rate of change of the ternary complexes binding reaction:

$$\frac{d[R]}{dt} = -k_f [R] [L] + k_r [C] \quad (4.9)$$

$$\frac{d[C]}{dt} = k_f [R] [L] - k_r [C] - k_c [H] [C] + k_u [T] \quad (4.10)$$

$$\frac{d[H]}{dt} = -k_c [H] [C] + k_u [T] \quad (4.11)$$

$$\frac{d[T]}{dt} = k_c [H] [C] - k_u [T] \quad (4.12)$$

$$\frac{d[L]}{dt} = -k_f [R] [L] + k_r [C] + S_L - \lambda_d [L] \quad (4.13)$$

where  $[L]$  denotes the concentration of EGF ligand in M (molar or moles per

volumes).  $[R]$  and  $[C]$  are the numbers of unbound and bound EGFR receptors (#/volume), respectively.  $[H]$  represents the number of unbound HER2 receptors (#/volume).  $S_L$  (molecule/min) and  $\lambda_d$  (molecule/min) are the ligand source and ligand degradation rate constants, respectively. The source of the whole mechanism is fed by the ligand production, this will be given more attention in next section of the report. *Remark: for the sake of simplicity the sign  $[-]$  will be removed in the next differential equations.*

Assuming there is no cell proliferation at this stage, the conservation laws apply. The sum of Eqs. (4.9), (4.10), and (4.12) is zero, as well then the sum of Eqs. (4.11) and (4.12), this implies that there exists non-negative constants,  $R_T$  and  $H_T$ , such that:

$$R_T = R(t) + C(t) + T(t) \quad (4.14)$$

$$H_T = H(t) + T(t) \quad (4.15)$$

where  $R_T$  is the total, unbound and bound, EGFR receptors per unit volume, and  $H_T$  is the total, unbound and bound, HER2 receptors per unit volume. Using Eqs. (4.14) and (4.15),  $R(t)$  and  $H(t)$  are expressed respectively by:

$$R(t) = R_T - C(t) - T(t) \quad (4.16)$$

$$H(t) = H_T - T(t) \quad (4.17)$$

Substituting these expressions into the system of equations, we get:

$$\frac{dC}{dt} = k_f (R_T - C - T) L - k_r C - k_c (H_T - T) C + k_u T \quad (4.18)$$

$$\frac{dT}{dt} = k_c (H_T - T) C - k_u T \quad (4.19)$$

$$\frac{dL}{dt} = k_f (R_T - C - T) L - k_r C + S_L - \lambda_d L \quad (4.20)$$

Assuming that the total number of receptors that can initiate a signal transduction pathway in response to the ligand, is proportional to the number of cells per unit volume, the relationship between the total cell surface receptor EGFR( $R_T$ ) and HER2 ( $H_T$ ) receptors and tumor cell density (P) we get :

$$R_T = \rho_R P(t) \quad (4.21)$$

$$H_T = \rho_H P(t) \quad (4.22)$$

As demonstrated previously, the basis of the ODE model to describe the growth kinetics of proliferant cells P(t) with the proliferation rate  $\mu$  is:

$$\frac{dP(t)}{dt} = \mu P(t) \quad (4.23)$$

As we said, Eladdadi and Isaacson's model considered that all the cells are cancerous and more particularly HER2-positive, cell overexpressing high level of the HER2 protein. Therefore they used the Monod phenomenological model to propose a new definition of the cell proliferation rate. Their description of cell proliferation,  $\mu$  by unity of time, being the following:

$$\mu(C, T) = A_1 \frac{\mu_{max}^1 C}{\mu_{half}^1 + C} + A_2 \frac{\mu_{max}^2 T}{\mu_{half}^2 + T} + \mu_0. \quad (4.24)$$

with:

- $A_1$  and  $A_2$  non-negative constants.
- $\mu_{max}^i (i = 1, 2)$  the maximum specific cell growth rate constant ( $time^{-1}$ ).
- $\mu_{half}^i (i = 1, 2)$  the number of occupied receptors required to generate half-maximal response ( $\#/unit\ volume$ ).



- $\mu_0$  the cell proliferation rate independent of EGFR and HER2 receptors ( $time^{-1}$ ).

Finally, combining all the model equations, we get the proliferation model describing the relationship between cell surface complexes EGF-EGFR and EGF-EGFR-HER2, and cell proliferation dynamics proposed by Eladdadi and Isaacson:

$$\frac{dC}{dt} = k_f (\rho_R P - C - T) L - k_r C - k_c (\rho_H P - T) C + k_u T \quad (4.25)$$

$$\frac{dT}{dt} = k_c (\rho_H P - T) C - k_u T \quad (4.26)$$

$$\frac{dL}{dt} = k_f (\rho_R P - C - T) L - k_r C + S_L - \lambda_d L \quad (4.27)$$

$$\frac{dP}{dt} = \left( A_1 \frac{\mu_{max}^1 C}{\mu_{half}^1 + C} + A_2 \frac{\mu_{max}^2 T}{\mu_{half}^2 + T} + \mu_0 \right) P \quad (4.28)$$

### 4.3.2 Receptor-ligand interaction

We build our model based on the work of Eladdadi and Isaacson detailed above. Using the similar notation from their model, we consider all the entities defined at position  $\mathbf{x} \in \Omega$  and time  $t$ . In this model, we consider the source term of the ligand,  $[L]$ , as the tumor cells themselves, with  $\gamma_p$  the rate production of ligand by the tumorous cells. We rewrite the chemical processes for the EGF-Receptor and the EGF-ligand as the following equations:

$$\begin{cases} \partial_t C &= k_f (\rho_R P - C - T) L - k_r C - k_c (\rho_H P - T) C + k_u T \\ \partial_t T &= k_c (\rho_H P - T) C - k_u T \\ \partial_t L &= k_f (\rho_R P - C - T) L - k_r C + \gamma_p P - \nabla \cdot (D \nabla L) - \lambda_d L \end{cases} \quad (4.29)$$

where  $\lambda_d$  is the natural decay rate for the EGF ligand  $L$ ;  $k_f$  and  $k_r$  are respectively the forward and reverse, binding rate constant of ligand with EGF-Receptor;  $k_c$  and

$k_u$  are respectively the coupling and uncoupling, rate constant of hetero-dimerizes with cell surface HER2 receptor;  $\rho_R$  and  $\rho_H$  are respectively EGF and HER2, total cell surface receptors (bounded and unbounded) per unit density volume (#/cell density);  $D$  the diffusion term of the EGF ligand  $L$ . In our model we considered that ligand diffusion depends on the environment,  $D$  is then defined by:

$$D = PD_1 + (S + L_u + N) D_2 \quad (4.30)$$

with  $D_1$  and  $D_2$ , the diffusion coefficients of the ligand respectively, in living tumor cells(proliferative tissue) and other types of tissue (necrosis, stroma tissue, lumen). We choose the diffusion coefficient such as  $D_2 \gg D_1$ . This hypothesis models the rapid cleavage and consumption of ligand by locally proliferative cell (autocrine process).

## 4.4 Computation of velocity

In order to determine the dynamics of the environment, more specifically the tumor motion, we need to compute the velocity,  $\mathbf{v}$ . Using the first equation on the velocity define by eq. 4.3, is not sufficient to determine the velocity, requiring an additional constitutive law. In this model we consider the different entities of cells forming a porous structure permeated by an organic fluid. The porous structure is deformable and its constituents undergo a relative motion because of cell division (see section 4.1). We will consider a Darcy-type law, such a model has already been applied to describe tumor cells [65, 15, 114] . The potential,  $\Pi$ , and the velocity,  $\mathbf{v}$ , for a

material of permeability,  $k$ , are described by the following equations:

$$\mathbf{v} = -k\nabla\Pi \quad (4.31)$$

Thus, using eq. 4.3 the potential field  $\Pi$  satisfies the elliptic equation:

$$-\nabla\cdot(\nabla k\Pi) = \alpha f_P P \quad (4.32)$$

We use this law, with a heterogeneous value of  $k$ , accordingly to the environment definition. This will express the different mechanical property of the environment, hence the porosity  $k$  is defined by:

$$k(\mathbf{x}, t) = k_{lumen}L + k_{cells}(S + P + N) + k_{wall}1_{\eta>0},$$

with  $k_{wall}$ ,  $k_{cells}$ ,  $k_{lumen}$  positive constants, and  $\eta$  a function quantifying the membrane and its degradation, that we will develop later (see section 4.5). Here we impose  $k_{wall} \ll k_{cells} \ll k_{lumen}$ , therefore the lumen will be considered less impermeable than cells and the duct wall will be considered as highly impermeable. This will allow for the lumen to have a fluid like behavior and the duct to be less subject to deformation. We consider that the boundary of the computational domain has no resistance to the movement of the entities:

$$\Pi = 0 \text{ on } \partial\Omega \quad (4.33)$$

We also prescribe the following boundary condition on the velocity field:

$$\mathbf{v}\cdot\mathbf{t} = 0 \text{ on } \partial\Omega \quad (4.34)$$

with  $\mathbf{t}$  being the tangent at the boundary of the domain  $\Omega$ .

## 4.5 Duct wall: localization and degradation

In this model the duct wall location is defined by a level set function  $\eta$ . The motion of the duct wall position is driven by fluid motion through the Darcy Law. We also assume the duct wall to be subject to possible degradation by MMP enzymes. MMP concentration is usually a local balance between production by cancer and stroma cells, and natural decay, for simplicity, we assume that MMP is locally proportional to the density of proliferant cells, and that degradation of the duct membrane is a function of MMP concentration, as it was performed in Ribba et al. work [114]. At time,  $t$ , and position,  $\mathbf{x} \in \Omega$ , the variable  $\eta$  represents the localization and degradation of the duct wall by the enzymes. The duct wall domain is represented by  $\Delta_t = \{\mathbf{x} \in \Omega, \eta(\mathbf{x}, t) > 0\}$  and the duct wall interface by  $\Gamma_t = \{\mathbf{x} \in \Omega, \eta(\mathbf{x}, t) = 0\}$ . The variable  $\eta$  evolves through:

$$\partial_t \eta + \mathbf{v} \cdot \nabla \eta = -\beta(\text{MMP})\eta^+ \quad (4.35)$$

where  $\eta^+$  represents the positive function of  $\eta$ :

$$\eta^+ = 1_{\eta>0}\eta,$$

MMP is the enzyme concentration, and  $\beta$  is a function written as a Michaelis-Menten model:

$$\beta(\text{MMP}) = \frac{\beta_{max}\text{MMP}}{\kappa_\beta + \text{MMP}} \quad (4.36)$$

where  $\beta_{max}$  and  $\kappa_\beta$  are positive constants.

We define the production of enzyme  $\text{MMP}(\mathbf{x}, t)$  at the position  $\mathbf{x} = (x, y, z,)$  and time,  $t$ . We consider that the enzyme concentration is a local balance, proportional

to the density of cancerous living cells:

$$\text{MMP} = \kappa_{\text{MMP}} P, \quad (4.37)$$

where  $\kappa_{\text{MMP}}$  is a positive constant. In section 4.4 it can be seen that the duct wall porosity is highly penalized leading to a high mechanical resistance of the duct to velocity. This will then necessitate a higher pressure to put the duct wall into motion, emulating the real scenario expected.

## 4.6 Computational approach

We defined a mathematical model based on PDEs to simulate HER positive DCIS. The model is nutrient-limited and the spatial dynamics is given by Darcy constitutive law. In this model the duct wall can be degraded by MMP enzymes produced by the proliferant cells.

Our model presents the advantage of materializing the environment condition through the equation and the initialization. Indeed the model in itself contains the different porosity values, and the wall location is determined by the level set function. This structure will be then well adapted for later clinical adaptation. Indeed, such a model will be able to treat individual clinical cases, by allowing the user to compute any simulation if the breast structure, more specifically the duct network, is well defined. For instance, a current tool used to define the duct network is the galactography: a contrast material is injected into the milk duct, and a mammogram is performed so that the inside of the milk duct can be seen. By using the level set function to define the duct network, the computation and evolution of the tumor in the whole

breast can be performed. This will allow surgeons to correctly determine the tissue to resect in order to have a negative margin.

To compute this mathematical model we will use eLYSe a numerical toolbox developed by INRIA MC2 team in Bordeaux [66]. In order to provide a complete description of the model, we define the general algorithm, giving an insight on the computation procedure. The definition of the computation algorithm is essential since our model is multiscale, each entity feeding the computation of other entities at a more macroscopic or microscopic scale. We defined our multiscale process in algorithm 1.

---

**Algorithm 1** Multiscale algorithm

---

```

1: Initialize all entities
2: for  $\Delta t = 1:N_{cycle}$  do
3:   Compute nutrients:  $\Theta$ 
4:   Compute birth and death rate of proliferant cells:  $f_{PN}, f_P$ 
5:   Compute permeability:  $k$ 
6:   Compute Darcy potential :  $\Pi$ 
7:   Compute velocity:  $\mathbf{v}$ 
8:   Compute divergence of  $\mathbf{v}$ :  $\nabla \cdot \mathbf{v}$ 
9:   for  $\delta_t = 1:n_{sub-cycle}$  do
10:    Compute cells entities:  $P, N, S, L_u$ 
11:    Compute enzymes:  $MMP$ 
12:    Compute duct wall:  $\eta$ 
13:    Compute ligand diffusion term:  $D$ 
14:    Compute chemical entities:  $C, T, L$ 
15:   end for
16: end for
17: return results

```

---

# Chapter 5

## Results & discussions

In this chapter we present brief results of our tumor growth model computation. Then we discuss the drawback of our model and the potential improvement we have derived.

### 5.1 Results

We test our model for a two-dimensional configuration, the usual experimental setup is illustrated in figure 5.1. This configuration will consider a tumor inside the duct surrounded by healthy (stroma) tissue, this configuration represents a typical DCIS tumor. Initially no necrosis cells are considered. The source of oxygen will be placed around the stroma tissue. Similarly to this disposition, we define our default configuration setup (see figure 5.2), it describes the environmental condition that appears the most descriptive from the local biology. This domain is quantified by the

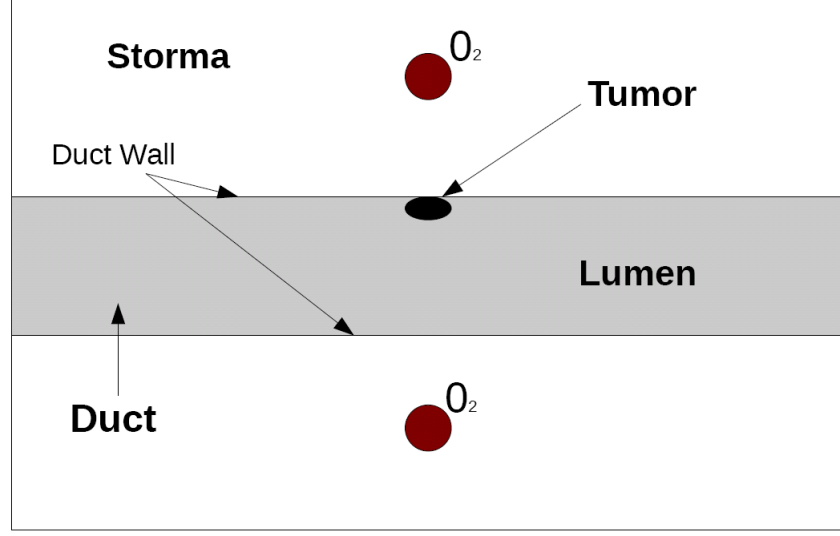


Figure 5.1: Computational domain of the experimental setup considered

length  $D_0$  in long and  $L_0$  in large. These lengths are considered as adimensionalized. The duct canal is in the transverse cut, positioned at the middle of the domain (i.e.  $\frac{D_0}{2}$ ), the diameter of the duct being  $\simeq \frac{D_0}{6}$ . Two oxygen sources are represented by disks at location  $(\frac{L_0}{2}, \frac{D_0}{8})$  and  $(\frac{L_0}{2}, \frac{7D_0}{8})$  both with a radius of  $\simeq \frac{D_0}{100}$ . The duct wall thickness is about  $\simeq \frac{D_0}{300}$ . All the parameters for the default test case are referenced in table 5.1. The initial configuration contains a disk of proliferant cells localized inside the duct, at the neighborhood of the duct wall with a radius  $\simeq \frac{D_0}{1000}$ . It can be observed in table 5.1, the parameters of the MMP enzyme production was selected in such a way that the MMP are not present and active in the default test. This can be removed by increasing the rate of the MMP production parameter  $\beta_{max}$ .

The computation of default setup and the default parameters corresponding is



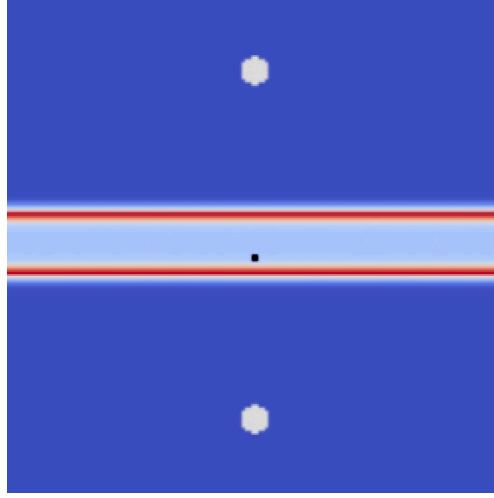


Figure 5.2: Illustration of the initial environment default setup scenario. Light blue being the lumen, dark blue the stroma/healthy cell, black dot the initial proliferant cells, white disks represent the nutrient sources, and the red strips the duct wall.

presented in figure 5.3, we can see that the tumor grows in order to fill the duct and is more likely to spread in the radius direction of the duct since it is attracted by the two nutrient sources around the duct. Also due to nutrient limitation of the environment, the tumor presents a necrotic core. This phenomena can be observed for real DCIS cases, referred as the comedo type (see section 3.1), we illustrate a juxtaposition of the default numerical result as well as a DCIS biopsy. The similarity leads us to believe that our model can reproduce such DCIS phenomena.

When reducing the nutrient rate of consumption by the cell, we observe that a solid DCIS with no necrotic core can be simulated (see figure 5.5). If the computation continues, the tumor will spread along the duct, after it completely fills the duct radius area. This phenomena replicates the non-comedo solid DCIS described in section 3.1.

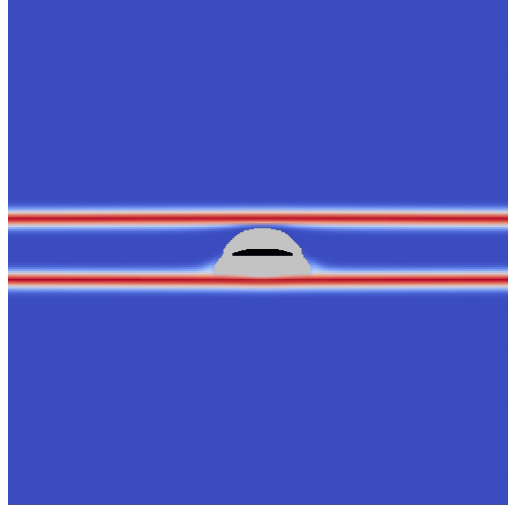


Figure 5.3: Default test after 3000 cellular cycle. Gray: proliferant density  $P \geq 0.5$ ; Black: necrosis density  $N \geq 0.5$ . Percentage distribution in the whole domain:  $P = 1.097\%$ ,  $N = 0.201\%$ ,  $S = 87.183\%$  and  $L_u = 11.511\%$ .

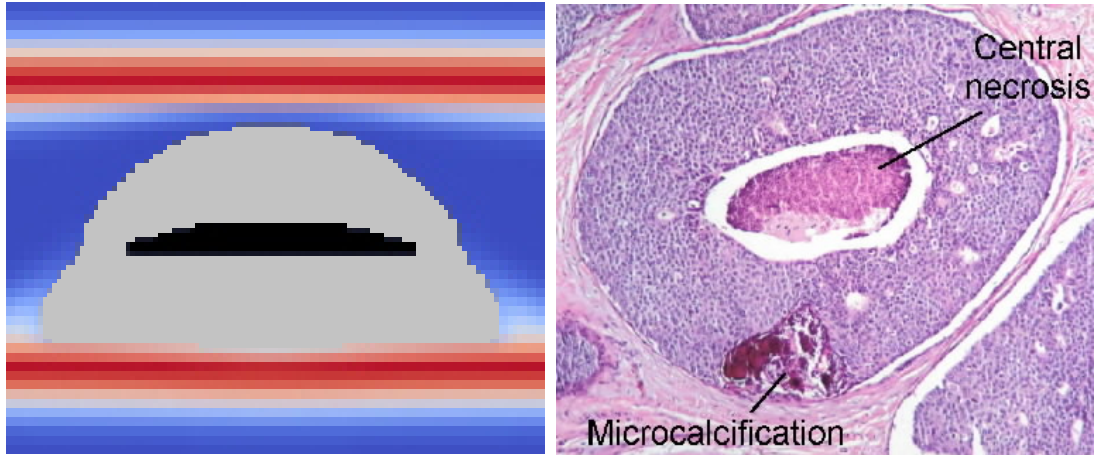


Figure 5.4: Juxtaposition of numerical results and biopsy. *Left:* Default test after 3000 cellular cycle. Gray: proliferant density  $P \geq 0.5$ ; Black: necrosis density  $N \geq 0.5$ . *Right:* Biopsy of DCIS with comedo type.

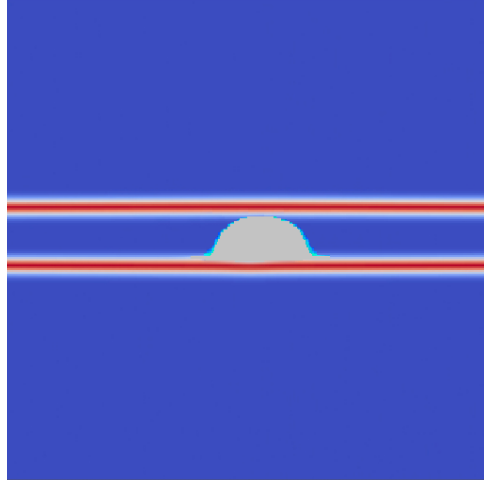


Figure 5.5: Default test after 1000 cellular cycle with a nutrient consumption rate very low:  $\Phi = 1$ . Gray: proliferant density  $P \geq 0.5$ ; no necrosis core has been reported in this simulation.

In an other campaign of computation we intend to visualize the influence of parameters on the whole computation. We compute the simulation for the default parameters, with only one parameter varying at a time, and output the total proliferant and necrosis density. The results of this computation, for the EGF receptor density coefficient,  $\rho_P$ , the HER2 density coefficient,  $\rho_H$ , the EGF ligand rate production  $\gamma_P$ , and the natural decay rate for the EGF ligand  $\lambda_d$ , can be seen in figure 5.6. We can observe that the most sensitive parameters amongst these is the EGF receptor density coefficient  $\rho_P$ . If we investigate these results further, we can also observe that overexpression of the HER2 density coefficient  $\rho_H$ , leads to a greater tumor growth speed than the ligand overexpression (increasing EGF ligand rate production  $\gamma_P$ ). When comparing the relative difference for proliferant cells between ligand overexpression and HER2 overexpression, no considerable results can be outputted,

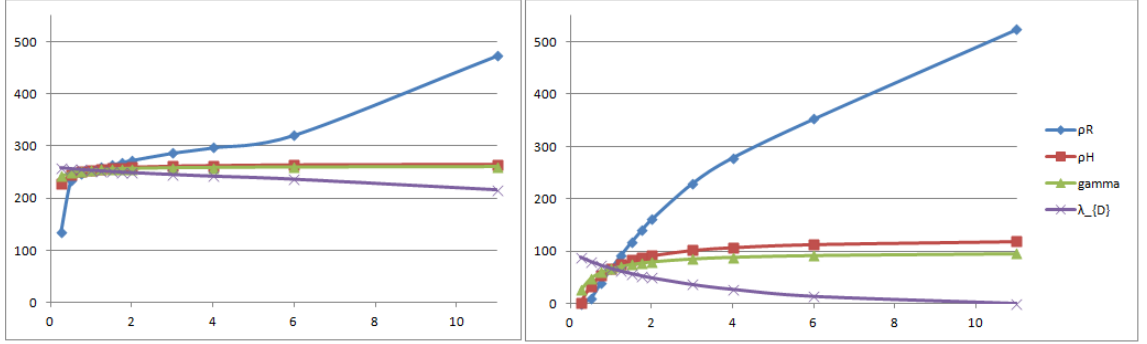


Figure 5.6: Graphs showing the total density of cells in function of the variation rate of the default value parameter:  $\rho_R$ (blue),  $\rho_H$ (red),  $\gamma_P$ (green),  $\lambda_d$ (purple). *Left:* Proliferant cells; *Right:* Necrosis cells.

however the relative difference of necrosis cells does not follow the same pattern; we observe an increase of  $\sim 13\%$  of necrosis population when HER2 are overexpressed as comparison of the ligand overexpression. Using the standard point of view that a tumor adapts and mutates as a function of the environment in order to increase their population, this could explain why HER2 positive carcinoma are more likely to overexpress the HER2 protein rather than EGF ligands, since it favors a greater total density of the tumor. Indeed Eladdadi and Isaacson reported that, while normal breast cells possess 20,000 – 50,000 HER2 receptors, the neu gene amplification can increase levels of this receptor up to 2,000,000 per cell, therefore representing a potential increase greater than 10,000% [38].

So far, our computation never included MMP production, we studied the effects of MMP on the tumor growth rate by igniting the coefficient  $\beta_{max} \neq 0$ . In figure 5.7 we plotted the influence of the MMP enzyme on the total density of tumor, we can see that the MMP contributed to the increase of the tumor density. This is due to the

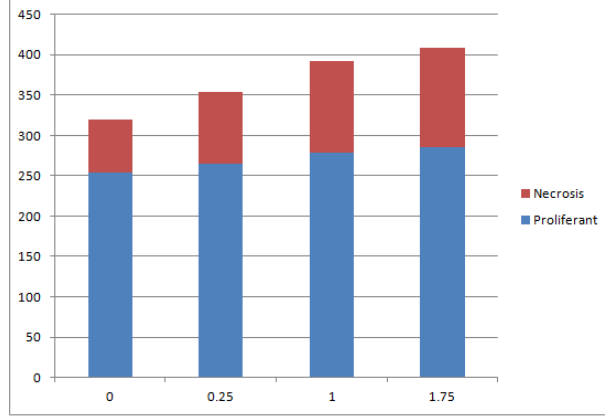


Figure 5.7: Total density of proliferant and necrosis cell as a function of the MMP production coefficient  $\beta_{max}$

invasive property of the tumor into the environment by breaking the duct wall. This allows the tumor to invade the healthy tissue and get closer to the nutrient source (see figure 5.8).

Finally, we investigate the importance of nutrient localization. Indeed as we mentioned earlier, we observed that the proliferation direction is oriented towards the nutrient source. The default configuration considered two sources of nutrients around the duct as presented in figure 5.2, this caused the tumor to fill the tumor in the radius direction, with a necrotic core (see figure 5.3). We investigated two other configurations of oxygen sources: test-A considers four disks of nutrients displayed in each corner of the domain (see figure 5.9); and test-B will consider two sources of nutrients represented in the transverse cut parallel to the duct (see figure 5.10). The visual result of these two computations are significantly different, suggesting that the tumor growth model is highly dependent on nutrient source location.

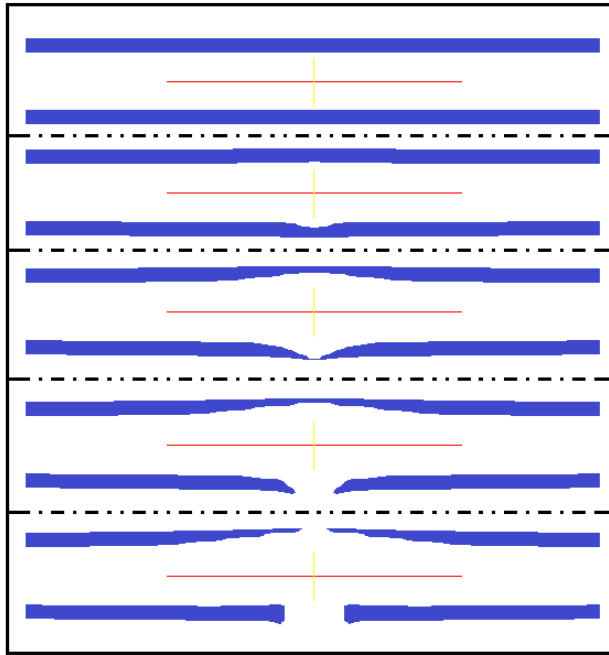


Figure 5.8: Illustration of the duct wall degradation by the MMP enzyme for a initial tumor placed at the lower part of the two-dimensional duct

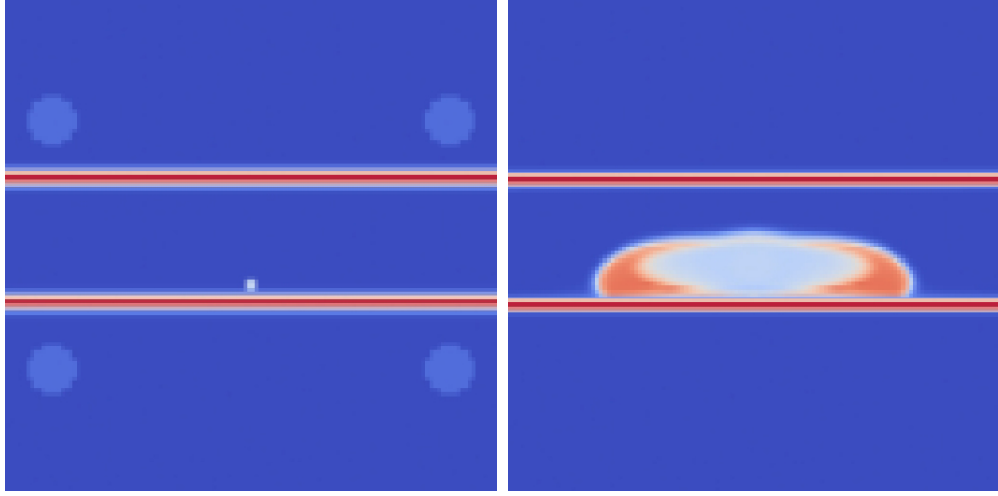


Figure 5.9: Left: Initial configuration for test-A, four sources of nutrients are placed around the duct. Right: Result of test-A computation (light red) proliferant cells, (white) necrosis cells.

After investigating the tumor growth model, by playing with a various set of parameters, we are going to discuss the model and its limitation. We will propose a possible improvement of the model.

## 5.2 Discussion

We presented a tumor growth model that we coded for a two-dimensional configuration. The next step will be to implement this model into a three-dimensional code. However before jumping into such considerations we need to improve the model in order to correctly model 3-D breast tumor growth. The tumor growth model we proposed is well adapted for the current 2-D configuration of the duct we proposed,

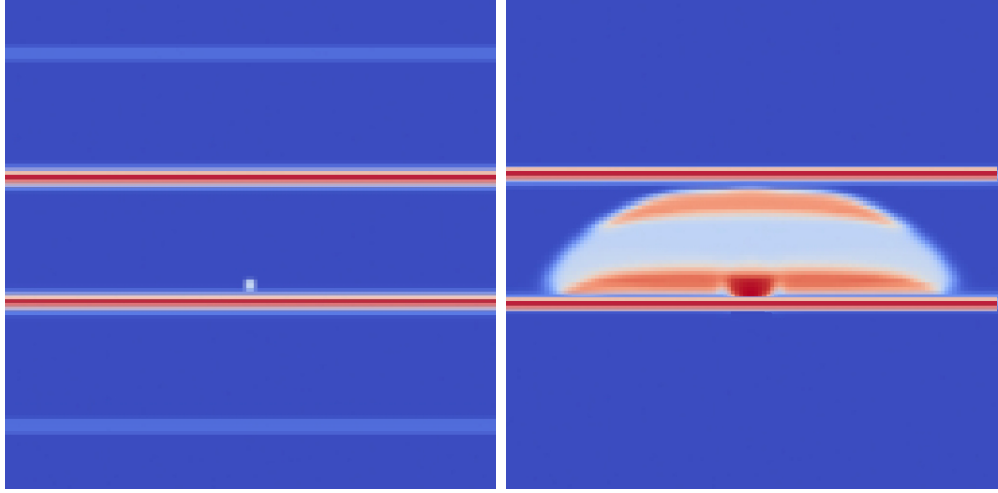


Figure 5.10: Left: Initial configuration for test-B, two sources of nutrients represented in the transverse cut parallel to the duct . Right: Result of test-B computation (light red) proliferant cells, (white) necrosis cells.

however a simulation of a transverse cut of the duct, as in figure 5.11, will immediately output some difficulties. Indeed such a configuration is not well adapted to our model since the tumor will grow indefinitely, increasing the pressure on the duct wall due to the incompressibility of the fluid. This will lead into a duct that will grow as big as the domain will be or the computation to crash due to unrealistic potential value,  $\Pi$ . This is due to the fact that no condition is established between the tumor proliferation and the value of the potential (that can be interpreted as a pressure). This will cause greater problems when computing in a three-dimensional since the tumor volume will grow indefinitely, increasing the breast size with it as well. In order to address this problem we are going to propose an alternative model that accounts for a relationship between the growth and the pressure,  $\Pi$ .

The new proposed model considered that the proliferation is regulated by an ad-



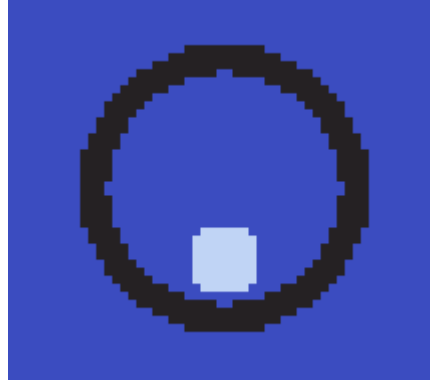


Figure 5.11: Transverse configuration of the duct with an initial tumor inside

ditional factor which is the pressure/potential  $\Pi$ . We considered that if cells are stressed to a certain threshold pressure  $\Pi_{max}$ , cellular division is inhibited. We adjust then the function  $f_P$  in eq. 4.5 by:

$$f_P = \begin{cases} \frac{[T]}{\alpha_T + [T]} \tanh(K_p(\Theta - \Theta_N)) & \text{if } \Theta > \Theta_N \text{ \& } \Pi < \Pi_{max} \\ 0 & \text{otherwise} \end{cases} \quad (5.1)$$

Thanks to this change, the pressure plays a regulatory factor on the cell proliferation, in order to materialize this with a sense, we need to consider the meaning of the pressure threshold  $\Pi_{max}$ . To achieve this we replace the boundary equation on  $\Pi$  (eq. 4.33) by the following time dependent pressure:

$$\Pi(t) = \left( \frac{V(t)}{V_{max}} \right)^\gamma \Pi_{max} \quad \text{on } \partial\Omega \quad (5.2)$$

where  $\Pi_{max}$  is the pressure threshold considered earlier,  $V_{max}$  is the corresponding volume threshold for the domain,  $V(t)$  is the computed volume of the duct canal, and  $\gamma = \frac{2}{5}$ . This description is inspired from the ideal gas consideration. Lets consider that initially  $V(t = 0) = \frac{V_{max}}{2}$ , this results in a boundary pressure of

$\Pi(t = 0) = (\frac{1}{2})^\gamma \Pi_{max} < \Pi_{max}$ . While the tumor grows,  $V \mapsto V_{max}$ , resulting in  $\Pi \mapsto \Pi_{max}$ , such a pressure change will induce the proliferant cells to stop the cellular division process. The computation of the volume can be processed using a level set function of the duct similar to  $\eta$  (see eq. 4.35) with no degradation. Also note for such an application to be possible, we need to ensure that the duct interface will never quit the domain.

Another improvement of the model could be to allow cells to switch into a quiescent phase when environmental conditions are not favorable, in this phase cell division no longer occurs, however if environmental condition are favorable again these quiescent cells can switch back into a proliferant state. In figure 5.12 we illustrate the flowchart of this growth model.

Far from providing the ultimate model, we presented a model that has considerable potential for clinical application. Indeed our model can easily be adapted to all kinds of geometric configuration, giving the ability to treat each patient case individually. In the long term such a model will allow surgeons to correctly assess the extent of the tumor to resect. This will allow patients to avoid undergoing a second surgical procedure, which represents at least 10 % of BCT procedures [36, 31, 28]. In order for this model to be fully ready for clinical practice, the model needs to considerably reduce the number of parameters to be tuned. This can be achieved by proceeding to a complete sensitivity analysis and disable non sensitive parameters, as well as fixed certain parameters which are considered similar for a load of groups of patients. Also, if such a tumor growth model can be used clinically, the increasing data provided by each patient case will allow to reduce the model parameters. In the mean time,

this model can be used to understand the tumor behavior and its adaptation to the environment as displayed in the results section.

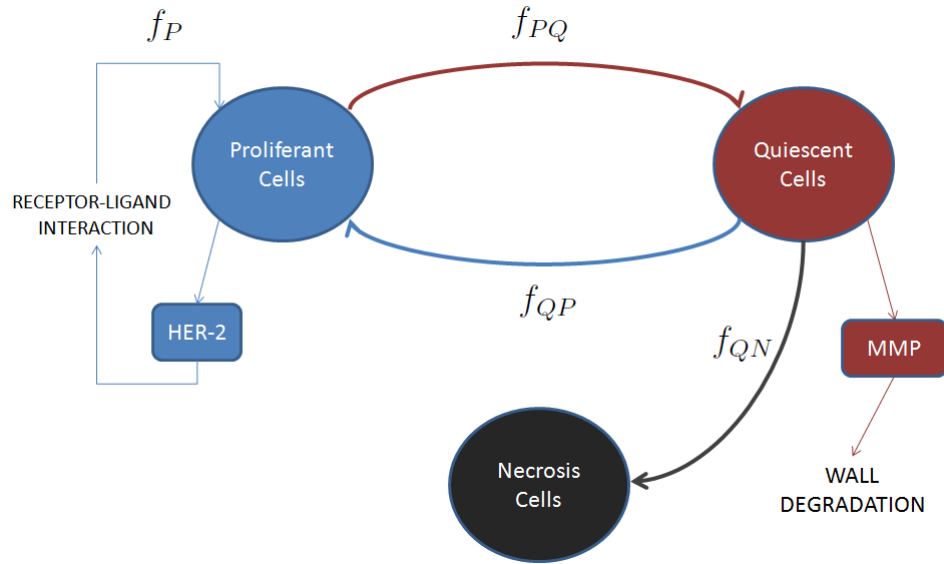


Figure 5.12: Improved tumor growth model

Parameter	Value	Unity	Equation	Ref.
Numerical parameters:				
$N_x$	150			
$N_y$	150			
$CFL$	0.45			
Environment parameters:				
$T$	3000	<i>cycle</i>		
$L_0$	1.2	<i>length</i>		
$D_0$	1.2	<i>length</i>		
Cancerous Cell parameters:				
$C_N$	$2.7 * 10^{-2}$	$M$	4.4, 4.5	
$\alpha$	2.8	$cycle^{-1}$	4.4, 4.5	
$\alpha_T$	0.5	—	4.5	
$K_p$	1.0	—	4.5 , 4.5	
Oxygen parameters:				
$\Theta_0$	0.0	$M$	4.6	
$\Theta_{max}$	$1.0 * 10^{-1}$	$M$	4.6	
$\phi$	50.0	—	4.6	
$K_{diff}$	1.0	$length^2.M^{-1}$	4.6	
Porosity parameters:				
$k_{lumen}$	10.0		4.31	
$k_{cells}$	2.0		4.31	
$k_{wall}$	$1.0 * 10^{-5}$		4.31	
Chemical parameters:				
$k_f$	$1.5714 * 10^{-1}$	$M^{-1}.(\frac{1}{10}cycle)^{-1}$	4.29	[38]
$k_r$	$2.4 * 10^{-1}$	$(\frac{1}{10}cycle)^{-1}$	4.29	[38]
$k_c$	$1.0 * 10^{-1}$	$(\frac{1}{10}cycle)^{-1}$	4.29	[38]
$k_u$	$1.0 * 10^{-2}$	$(\frac{1}{10}cycle)^{-1}$	4.29	[38]
$\rho_R$	$3.33 * 10^{-1}$	$receptors.VOF^{-1}$	4.29	[38]
$\rho_H$	1.0	$receptors.VOF^{-1}$	4.29	[38]
$D_1$	$1.0 * 10^{-6}$	$length^2.(\frac{1}{10}cycle)^{-1}$	4.29	
$D_2$	$1.0 * 10^{-6}$	$length^2.(\frac{1}{10}cycle)^{-1}$	4.29	
$\gamma_P$	$1.0 * 10^{-5}$	$M^{-1}.(\frac{1}{10}cycle)^{-1}$	4.29	
$\lambda_d$	$1.0 * 10^{-5}$	$(\frac{1}{10}cycle)^{-1}$	4.29	
MMP parameters:				
$\beta_{max}$	0.0	$(\frac{1}{10}cycle)^{-1}$	4.36	
$\kappa_\beta$	1.0	—	4.36	
$\kappa_e$	1.0	—	4.37	

Table 5.1: Default parameter values of the tumor growth model

## Part III

# Virtual surgery box for breast conserving therapy

# Chapter 6

## Review & motivation

### 6.1 Motivation for virtual surgery

The current procedure to treat patients diagnosed with breast cancer is surgery, unfortunately this step appears to be inevitable. Although some alternative techniques requiring no surgery have recently been investigated, such as the eradication of the tumor by cooling [11], no accepted clinical substitutions to surgery have been proposed and accepted to date. As we detailed earlier in part I, surgery for early stage breast carcinoma is either total mastectomy (complete breast removal) or surgical lumpectomy (only tumor removal). Lumpectomy coupled with radiotherapy [143], commonly known as Breast Conserving Therapy (BCT), enables the elimination of any microscopic cancer cells in the remaining breast tissue. The goals of BCT are to achieve local control of the cancer as well as to preserve a breast that satisfies the woman's cosmetic, emotional, and physical needs. Trials for breast conservative

therapy with patients affected by breast cancer (I and II) have demonstrated conclusively that BCT produces disease control and survival rates at least equivalent to those of mastectomy, and possibly better in the long run for patients with stage II breast cancer [22]. While most women undergo partial mastectomies with satisfactory cosmetic results, in many patients the remaining breast is left with significant cosmetic defects including concave deformities, distortion of the nipple-areola complex, asymmetry, and changes in tissue density characterized by excessive density associated with parenchymal scarring. These flaws have been reported to contribute to poor body image and psychological distress in some patients.

The advantages of BCT over mastectomy include faster recovery and a better cosmetic outcome for patients. Therefore, BCT should improve the Quality Of Life(QOL) of the patient. Nonetheless, these patients still have to undergo the trauma and hardship of radiation therapy. Therefore, it is key for the surgeons to come out with a satisfactory assessment of the patient on their body image. Furthermore, it has been reported that a link exists between the psychological aspects of patient satisfaction due to the cosmetic outcome, and morbidity[13]. Hence, a bad cosmetic outcome could end up in a complete failure for the patient. Taylor et al. [134] addressed the tumor and group characteristics that led to good outcomes in terms of cosmetic results. They reported that large resections, older age groups, scar orientation, and high radiation doses could lead to a poor outcome. Researchers assessing QOL after breast surgery [134, 52, 128, 54, 42], do not only include the aesthetic factor, but also functional status such as pain and mobility. As a matter of fact, Vries et al. [34], on a study including 102 women undergoing BCT, reported that 63% expressed breast

pain within an average of 36 months after surgery, decreasing to 52% 18 months later. They also reported that the severity of the pain decreased significantly with time, and that no correlation could be established with post-chemotherapy or hormonal treatment.

Using the convergence of disciplines, we propose to build a computational framework, named the Virtual Surgery Box (VSB), for BCT surgery. This tool will improve the surgical outcomes of BCT in regards to prediction of cosmetic and functionality of the breast. The first objective is obviously to provide a tool that can help the dialogue between the patient and the surgeon by providing some rational evidence of what the BCT outcome would be. Virtual surgery in that context should help in exploring various options and therefore guiding decisions. This is a very ambitious goal because the VSB needs to be finely tuned to specific patients' data. Indeed, the more experiences one accumulates with the digital information provided by the VSB for each patient, the better is the quality of the prediction. An intermediate objective of the VSB is to companion each clinical case with the VSB processing in order to build a data base of knowledge. There are numerous techniques available in data mining and statistics that would provide rigorous classification information and error estimates. Finally, once a VSB has gained enough accuracy in this learning process, this tool should be relevant for surgery education. The VSB used as a simulator should enable beginners to gain some judgment, experience, and understanding of the influencing factors through virtual surgery rather than actual surgery. To our knowledge, our work constitutes the first computational framework designed to predict BCT outcomes and explore targets for improvement.



In this part III, we are going to present the work achieve in regards of building this VSB. We started by giving the motivation of our work and a literature review of breast tissue mechanical model in this chapter 6. We will describe the design of the VSB in chapter 7, and the creation of the VSB indicators in chapter 8. We will output the results of out simulations on chapter 9, and we will conclude this part III, by proposing in chapter 10 a multiscale model simulating wound healing using CA that we implemented in two-dimension.

## 6.2 Model and related work

A fair amount of bio-mechanical models for breast tissue have been investigated, all mainly employ finite element methods to predict breast deformation in different situations, this includes:

- guiding clinical breast biopsy (Samani et al.[121] and Azar et al. [17, 18, 20, 19]);
- simulating the compression of breast as in X-ray mammograsy (Ruiter et al. [120, 119]);
- investigating the X-ray and MR mammography registration (Schnabel et al. [126, 125], and Tanner et al.[131, 132]);
- reconstructing the breast using idealized and realistic geometric models, and real patients (Williams et al. [144], and Roose et al. [117]);

- analyzing the impact of stresses and strains occurring in the skin after breast reconstruction (Pamplona et al.[102]);
- predicting the impact of gravity loading on breast mechanics, on an idealized shape and a real patient case (Ozan [100], and Palomar et al. [35])
- finding the reference state of the breast from a deformed configuration (University of Auckland Bioengineering Institute[32, 108, 109, 110]).

Breast biopsy today consists of an extraction of a breast tissue sample using a needle. While the patient lies in prone position with the breast gently compressed between plates, the needle is placed in the breast through one of the plate holes, called the lateral plate containing 1000 holes placed at 5mm intervals [18]. The impossibility to conduct continuous breast imaging through MRI, makes the breast biopsy a critical intervention. Indeed the location of the needle insertion is key in order to make sure the correct region of interest is being extracted. In order to accurately operate, the location of the cancerous lesion is calculated from the contrast-enhanced MRI, the correct hole in the plate is identified and the needle is inserted into the breast through the hole with a precalculated depth. The issue of such a method is that the use of the compression plate after the contrast agent MRI, may critically change the characteristics of the tumors making this operation critical [18]. An inaccurate initial needle placement can removed a tissue specimen outside the lesion of interest. Azar et al. [17, 18, 20, 19] proposed a new method to track the position of the hard inclusion based on a deformable finite element model of the breast. This work presented is the first in the area of breast modeling, allowing clinical cases to successfully take

advantage of mechanical modeling. This opened the door to other areas of interest for breast cancer to come in and use FEM such as image registration.

Image registration, is the process of transforming different sets of data into one coordinate system, allowing clinicians to relate the different breast imaging data coming from different periods of time and different imaging modalities, and providing some assistance for a image guided procedure. The earliest model constituted of nonrigid registration excluding the tissue mechanics [118]. Schnabel et al. [126, 125] proposed a method to map between pre- and post- contrast enhanced MRI using biomechanical models. Ruiter et al. proposed a similar strategy to correlate MRI images with X-ray mammograms, which are typically compressed.

Other applications of breast mechanical modeling involves the prediction of post surgery shape. As it was mentioned by Williams et al. in 2003 [144], there is currently no reliable methods to accurately predict the outcome of breast surgery. So far the current breast reconstructive procedure performed, relies on the surgeon's experience and subjective judgment. Williams et al. addressed this issue by studying the response of the breast to implants and the transverse rectus abdominis myocutaneous (TRAM) flap. The breast tissue was modeled as an hyperelastic material using the Mooney-Rivlin strain energy function detailed in part I. In an other study, Pamplona and Alvim [102] used finite elements to analyze the immediate stresses and strain occurring in the breast after reconstruction using an hyperelastic representation of the breast tissue. More recently Ozan [100] studied the deformation under gravity of an idealized breast shape using different commercial FEM software

(ABAQUS & COMSOL). His computation was performed testing different mechanical breast models, with or without skin, and different material constitutive law: Mooney Rivlin, Neo-Hookean. Palomar et al. [35] proposed a biomechanical model to predict the different positions of the breast. The study was performed on two patients and results were compared using a 3-D scan. The breast tissue was modeled through ABAQUS as a Neo-Hookean material covered by a skin model using a polynomial strain energy function. The accuracy of the model was measured by comparing manually identified landmarks. Their model was successful, keeping all measures under a 7.5% relative error.

While most studies propose accurate mechanical models to simulate breast deformation they somehow all used a wide range of different materials to model breast tissue. Most of these studies, reported here, considered the breast tissue as an incompressible (or nearly incompressible) isotropic homogeneous material, some performed the computation using linear elastic model [133, 117] to simulate the breast material, the other majority using a non-linear constitutive law to simulate the breast tissue material [17, 18, 20, 19, 133, 35, 100, 32, 108]. Studies using non-linear material, presented different approaches to simulate breast deformation, the most current ones being:

- Exponential model, where the young modulus is given by  $E = be^{m\varepsilon}$  with  $\varepsilon$  representing the strain, and  $b$  and  $m$  the material constant [17, 18, 20, 19];
- Neo-Hookean model where the strain energy function is defined by  $W = C_{10}(\bar{I}_1 - 3) + D_1(J - 1)^2$  (see eq. 2.14 part I) [133, 35, 100, 32, 108];

- Mooney-Rivlin model where the strain energy function is defined by  $W = C_{01}(\bar{I}_2 - 3) + C_{10}(\bar{I}_1 - 3) + D_1(J - 1)^2$  (see eq.2.15 part I) [100, 32, 108];
- complex polynomial model where the strain energy function is defined by  $W = \sum_{i,j=0}^n C_{ij}(\bar{I}_1 - 3)^i(\bar{I}_2 - 3)^j + \sum_{k=0}^m D_k(J - 1)^{2k}$  (see eq. 2.13 part I) [133, 122].

This range of different models highlights the fact that there is not a general accepted biomechanical model to simulate breast deformation, however it should be noted that tendency is to use hyperelastic material, most recent applied studies showing that Neo-Hookean or Mooney-Rivlin was a good enough behavior definition for breast tissue [35, 32, 108]. Another issue is that, there is a fair amount of uncertainty in the material properties (material constant values measured) of the soft tissue that composes the breast.

According to Krouskop et al. [78] fat tissue and glandular tissue have similar elastic modulus at low strain levels, while glandular tissue elastic modulus increases by one order of magnitude at high strain levels. Likewise fibrous tissue has an elastic modulus with an one to two order of magnitude higher than fat tissue. Furthermore, with breast tissue composition and distribution being specific and unique to each patient, it is expected that each patient presents a different value for the material constant. For these reasons, it will appear unreasonable in later studies to propose a model with fixed values regarding the constant material.

Breast mechanical models cover a great range of clinical applications, however while one of the latest input in breast cancer surgery, the lumpectomy, is rising and has become widely embraced by clinicians and patients, this type of surgery has never been offered any kind of simulation. Therefore we are going to develop a toolbox

in order to fulfill this task and propose a virtual surgery box (VSB) for the BCT operation.

# Chapter 7

## The virtual surgery box (VSB)

In this chapter we present the Virtual Surgery Box (VSB), we will detail design considerations we implemented through the input in section 7.1, we followed by describing the VSB computational process detailing the tools and methods used for the breast image acquisition and the breast surgery modeling (in section 7.2).

### 7.1 Design considerations

Our objective is to build a tool that can emulate the BCT surgery using mechanical modeling. The ultimate goal being to provide patients and clinicians a device which is patient specific to simulate the BCT surgery outcome. This will provide a powerful tool for the decision process patients and clinicians undergo, allowing them to make a choice for the best interest. While we focus on the design and feasibility of such a virtual box, our approach should readily extend to a more advanced patient specific

situation. To fulfill these requirements, the design of the input is key to provide clinicians with a tool that is easy to use and parameter. It also means that we need to have parameters that can be assessed or be measured by clinicians. Indeed, providing a tool for clinical practice needs to insure that the model proposed by the scientist requires only available clinical information.

We classified the VSB input into three different categories:

- **surgery inputs:** the one related to the size and location of the resection;
- **patient environment input:** the one related to the mechanical properties of the breast tissue specific to the patient;
- **recovery inputs:** the one related to recovery and healing dynamic.

To embed this tool for clinical conditions we defined input constraints making sure that these inputs were simple and relevant for surgeons.

The first input constraint was the nature of the surgical information. It is obvious that surgeons are not able to provide the accurate location, volume, and shape they are going to administer to each patient before surgery. Indeed many variables need to be taken into account from the patient's side. As well as on the surgeon's side, providing different type of resections based on their own technique and experience. Therefore, our model assumes that the tumor resection is a sphere, the information needed are then: the center coordinates and the resection radius.

The second input constraint, is the patient's environmental conditions. Assessment of soft tissue property is challenging and to date there is currently no tool that can claim to provide an accurate measure of mechanical soft tissue property in a non-invasive



manner. Moreover the breast tissue heterogeneity and they different mechanical properties add complexity to the addressed issue. Indeed, those tissue mechanical properties are patient specific and certainly not homogeneous across the breast. As mentioned in part I, the breast anatomy is composed of different structural tissue regions, e.g. fat, fibroglandular, skin; also it was highlighted earlier that glandular and fat tissue, for example, have different mechanical behaviors [78](see section 6.2). Highlighting these observations, published values of the stress to strain relationship of breast tissue types vary considerably in the literature [123, 95]. From a mechanical engineering point of view, playing with all these spectrum of parameters can end up in a fastidious process, therefore the design of this box was made considering models with the least parameter: allowing freedom to change but constraining the user not to get lost in details. We expect the user to be able to play with a set of different mechanical property values using their own knowledge and experience. We envision a process in which the human operator will interact with the VSB. In the best case scenario, the lower load of data required by soft tissue mechanics would be an estimate of stiffness and compressibility of the tissue. For this reason, to keep this input as simple as possible, we considered the breast tissue to be homogeneous and characterized by two attributes: the tissue compressibility that is related to the expected change of volume under pressure, and the tissue stiffness that corresponds to the expected resistance to deformation. Since, the values for each patient is highly inaccessible with the technology developed so far, our hypothesis is that the surgeons can gain experience to set up these parameters values by a trial and error series with the simulator. In fact, the surgeon should set the ratio of these two parameters to

default values known for an average patient, and from there, increase or decrease the material parameter.

The last input constraint is in regards to the recovery process. Response to surgery can vary significantly among patients depending on age, tissue property, and life activity, each body responding in its unique way. This toolbox is designed to provide the freedom for the user to be able to consider different recovery options, allowing it to be patient specific. Our hypothesis is that the dynamic of BCT recovery might be characterized by the amount of inflammation at the beginning of the process and/or tissue lost at wound closure. This, respectively, will dilate or contract the open space left by the resection. The potential positive or negative impact on recovery will be conveniently assessed by one single additional parameter using a pseudo internal pressure in the wound. As a first draft, the idea would be for the surgeon to virtually test the worst possible scenario, assuming for example that the amount of tissue lost in healing can be as much as 20% [72]. A more advanced model will be described later implementing a wound healing code.

The VSB will integrate all these input data, translate, and adapt it to processing parameters for the toolbox. Once this step is achieved, the mechanical model tool will proceed the simulation and will output the results, the unprocessed result from a mechanical tool usually being a three-dimensional surface visualization or the value of marker displacement. This toolbox design is illustrated in figure 7.1. In the next section we are going to describe in more detail the VSB algorithm.

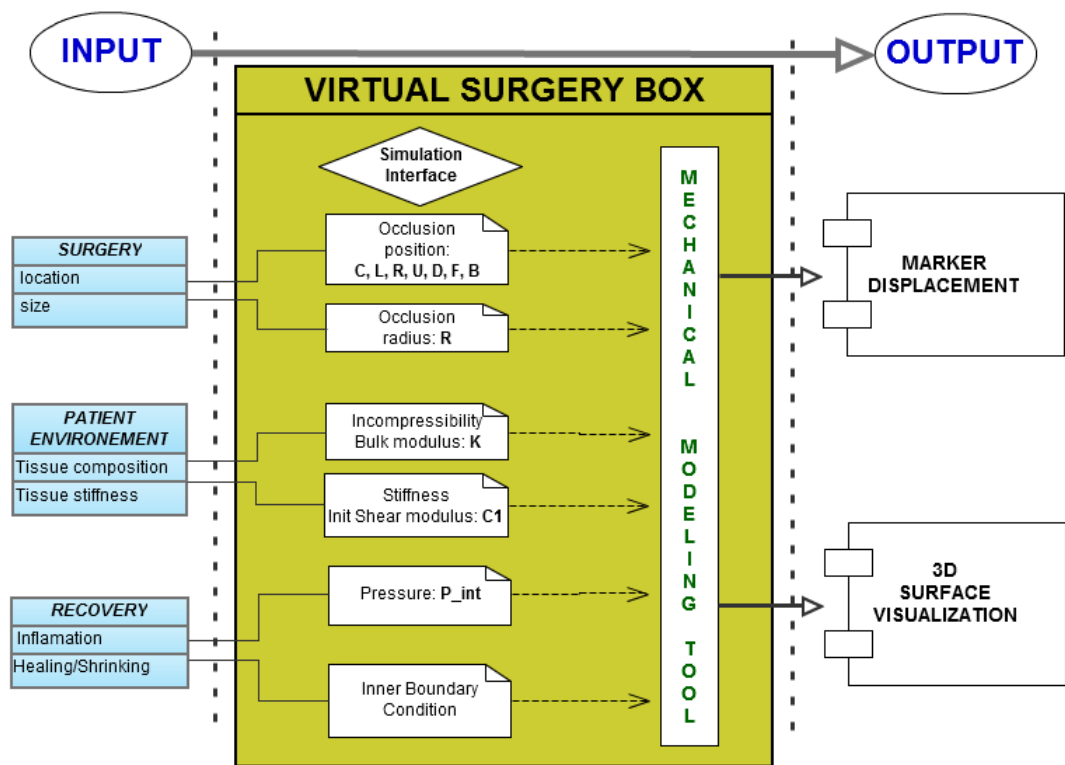


Figure 7.1: Virtual surgery box illustration.

## 7.2 VSB algorithm

The VSB step processes to simulate the BCT surgery is described in algorithm 2. The illustration of this algorithm is illustrated in figure 7.2, showing the different

---

**Algorithm 2** VSB algorithm

---

- 1: *MRI acquisition of the patient breast*
  - 2: *Segmentation of the patient breast*
  - 3: *Create the 3D breast geometry in FEM software*
  - 4: *Mesh the breast geometry*
  - 5: *Get the unloaded shape of breast patient*
  - 6: *Get the loaded shape of breast patient before BCT*
  - 7: *Proceed to virtual surgery for the unloaded shape*
  - 8: *Get the loaded shape of breast patient treated with BCT*
  - 9: *Output results*
- 

steps of the process done by the VSB. In this section, we are going first to introduce the breast MRI acquisition tool specificity, then we will introduce the segmentation method we used to segment the breast shape in subsection 7.2.1; and in subsection 7.2.2, we will describe the FEM simulation process we followed in order to get at first the unloaded shape, then proceed for virtual surgery, and finally get the post-surgery loaded shape.

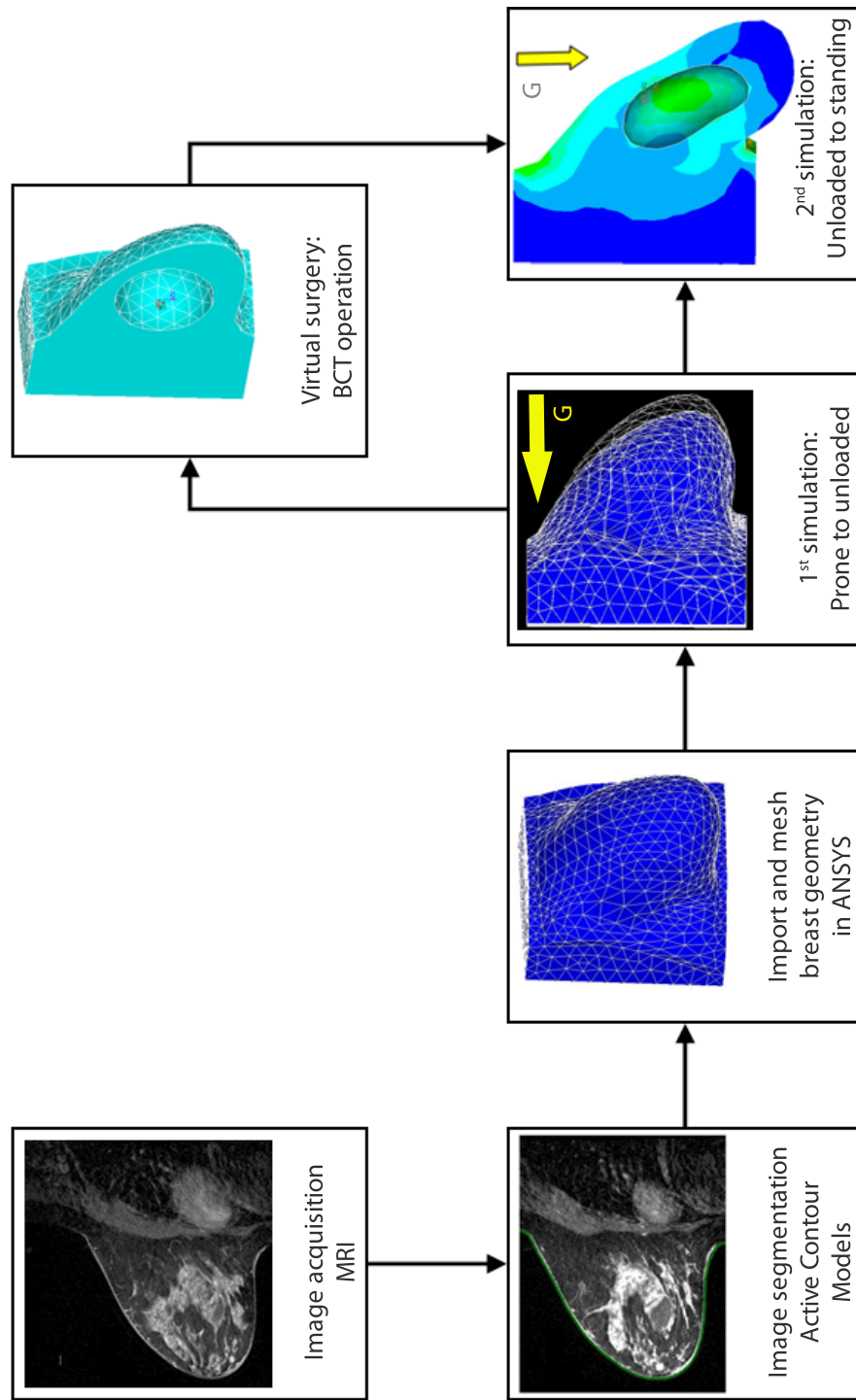


Figure 7.2: Flowchart illustrating the model construction and simulation of BCT.

## 7.2.1 Image acquisition

### 7.2.1.1 Magnetic resonance imaging (MRI)

Magnetic resonance imaging (MRI), or nuclear magnetic resonance imaging (NMRI), is primarily a medical imaging technique most commonly used in radiology to visualize detailed internal structures and limited functions of the body. Magnetic resonance imaging is a relatively new technology. The first MR image was published in 1973 and the first cross-sectional image of a living mouse was published in January 1974. The first studies performed on humans were published in 1977. MRI provides great contrast between the different soft tissues of the body, making it especially useful in neurological (brain), musculoskeletal, cardiovascular, and oncological (cancer) imaging. Unlike most medical imaging devices, MRI does not expose the patient to radiations, it uses a powerful magnetic field (standard unit being the Tesla) to align the nuclear magnetization of (usually) hydrogen atoms of water in the body. Radio frequency (RF) fields are used to systematically alter the alignment of this magnetization, causing the hydrogen nuclei to produce a rotating magnetic field detectable by the scanner. This signal can be manipulated by additional magnetic fields to build up enough information to construct an image of the body. In figure 7.3 we output a General Electric MRI device the Optima MR360 using a 1.5 Tesla magnetic field.

There are three main planes of acquisition used in MR imaging (see fig 7.4):

- Coronal orientation: in a cross section (plane), for example, across the shoulders, dividing the body into front and back halves



Figure 7.3: Magnetic resonance imaging device Optima MR360 from General Electric (image taken from [9]).

- Sagittal orientation: in a cross section (plane), for example, down the middle, dividing the body into left and right halves
- Axial orientation: in a cross section (plane), perpendicular to the long axis of the body, dividing the body into upper and lower halves

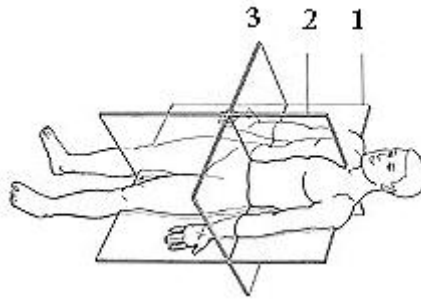


Figure 7.4: The three MR slice orientations: 1. Coronal, 2. Sagittal, 3. Axial. (Image taken from [3])

Patient undergoing breast MRI will be required to lie on their stomach on the scan table (prone position). The breasts will rest in cushioned holes that are part of the breast coil (see figure 7.5). This breast coil works like an antenna and allows the MRI device to take very detailed images of the breast. The scan table will slide into the scanner with the upper body centered in the scanner. A series of pictures will be taken during the procedure, each series lasting only a few minutes. Patients are not required to hold their breath while the images are being taken, but it is very important to be as still as possible while the machine is acquiring images. Unlike a mammogram, this procedure does not require compression of the breasts.

The other type of imaging modality for breast cancer is mammography, ultrasonog-



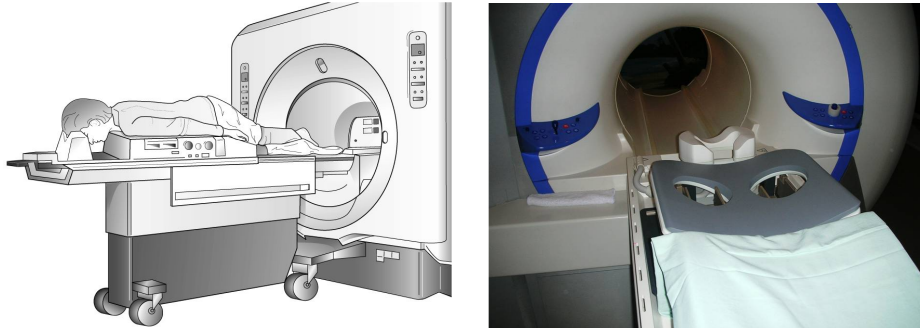


Figure 7.5: (left) Patient positioning in MR examinations [6]; (right) Breast MRI equipment [5]

raphy, and computed tomography (CT).

In this study we will adapt our toolbox to input breast MRI data. The MRI data are collected in stack of DICOM (Digital Imaging and Communications in Medicine), these files contain the medical scan and the meta-data such as the pixel spacing in the image directions, the space between each slice of scan token, as well as all patient information. In figure 7.6 we output DICOM of a breast MRI mapped on the sagittal plan with a pixel spacing of 0.4mm in the MRI plane and a 2.4mm between each slices. Starting from these MRI slices we will rebuild the 3D breast geometry by segmenting the images.

#### 7.2.1.2 Image segmentation

The segmentation of the breast contour was required in order to be able to rebuild the 3D breast geometry for each patient data. The segmentation method needs to be

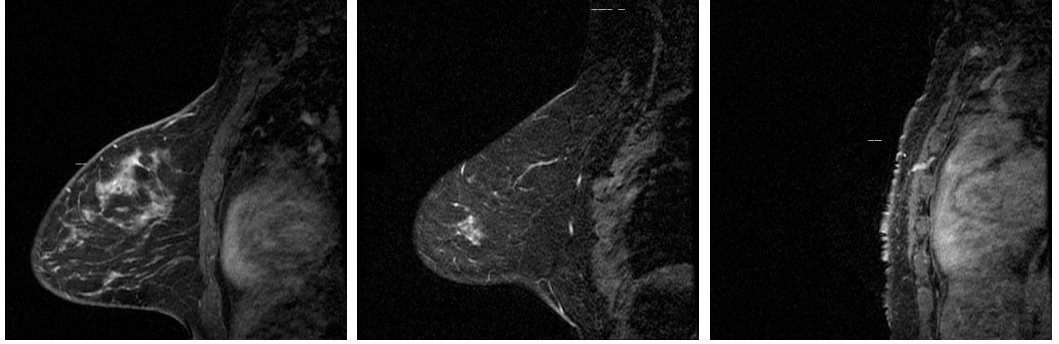


Figure 7.6: Breast Magnetic Resonance Images (BMRI) in the Sagittal plane orientation

robust in order to be able to cope with the different scenarios and difficulties specific to each patient. For instance, the presence of noise is high for peripheral slices (at the extremities of the breast), other cases will also present scenarios very difficult to interpret as it can be seen in figure 7.7. Also, the heterogeneity makes the extraction of the breast contour a segmentation task that is not straight-forward. Adapting the hybrid active contour -snake- model, developed by Lankton et al. [80] outputted the best results for breast segmentation. This method was detailed earlier in section 2.3. This method demonstrated to be the most robust and accurate for our application, coping with the fuzziness of image contour that is found at the periphery of the breast. The segmentation was done through MATLAB<sup>TM</sup>, the code was semi-automatic and needed an operator's intervention to initialize the method for each patient. In order to decrease the computation time and to make sure the segmentation was done correctly we proceed with a 5-level multiresolution pyramid for the segmentation (see figure 7.8 for an illustration of multiresolution pyramid), first segmenting the slice with a lower resolution and using the result as the new initial mask for the next resolution.

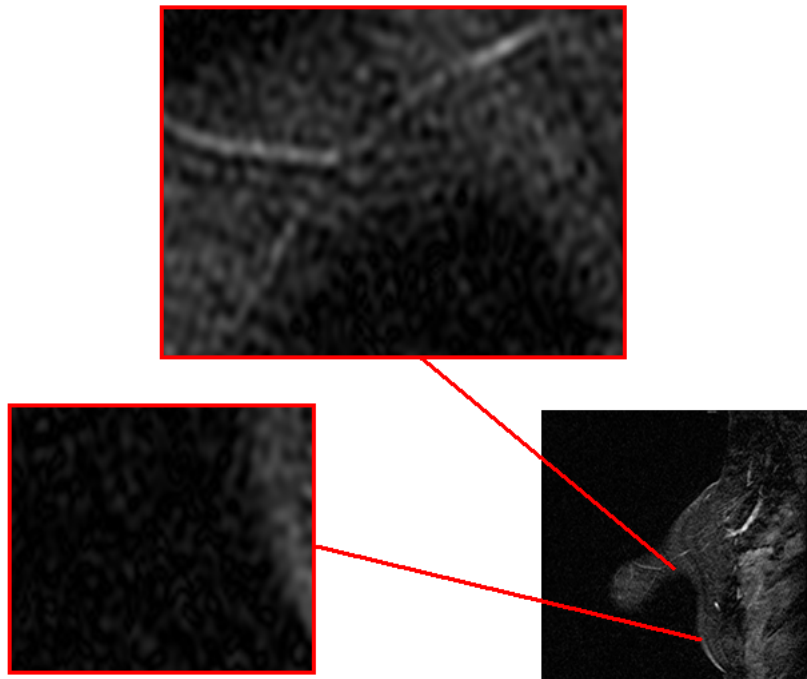


Figure 7.7: Illustration of noisy breast MRI in the sagittal plane orientation

This will also allow the contour to initially segment the greater object which was in figure 7.8 the breast contour. In fact using this method for some patients could avoid any type of human operator initialization. The algorithm is detailed in algorithm 3. The computation time for a complete breast segmentation using this method with a dual core CPU of 2.10 GHz and 2.00 GB RAM will typically take less than 30 minutes. An example of results of slice segmentation for patient can be seen in figure 7.9, as well as the 3D results in MATLAB<sup>TM</sup> after the whole breast reconstruction. Besides the fact of being a robust method, Lankton model shows the advantage to be a level set-based method leaving the user the ability to distinguish the inside and outside of the object with no intervention as well as giving the contour coordinates as precise as the pixel spacing.

---

**Algorithm 3** Breast MRI segmenation algorithm

---

- 1: *Get the width and length,  $N_L$  and  $N_W$ , of the MRI slice image*
  - 2: *Create  $I_{MASK}$  the initial segmentation mask for MRI slice # 1*
  - 3: **for** All MRI slices **do**
  - 4:     **for**  $k=0:4$  **do**
  - 5:         *Segment MRI of pixel resolution  $\frac{N_L}{2^{4-k}} \times \frac{N_W}{2^{4-k}}$  using  $I_{MASK}$*
  - 6:         *Update  $I_{MASK}$*
  - 7:     **end for**
  - 8: **end for**
  - 9: *Translate pixels into a metric measure using the DICOM information*
  - 10: *Merge slices data to create 3D shape*
-



Figure 7.8: Illustration of a 3 level multiresolution pyramid. We can see that the resolution of the images increases when going to the right direction. The use of low resolution for segmentation allows the segmentation contour to increase the computation speed as well as making sure the active contour model segments the main object.

## 7.2.2 FEM simulation

### 7.2.2.1 Biomechanical model

In this study we propose to use a biomechanical model for breast tissue to simulate the BCT operation. All the finite element computation for the VSB will be using the commercial code ANSYS<sup>TM</sup> [8]. This software has previously been used by Tanner et al.[133] in 2006 to perform finite element computation simulating breast compression. We segmented the geometry using the tetrahedral element SOLID187 of ANSYS<sup>TM</sup> (see figure 7.11). This element is defined by 10 nodes having three degrees of freedom at each node: translations in the nodal x, y, and z directions. It supports the large displacement and large strain characteristics of breast deformation. The average mesh size for the computation was 8 *mm* (see table 9.1 for the number of total elements).

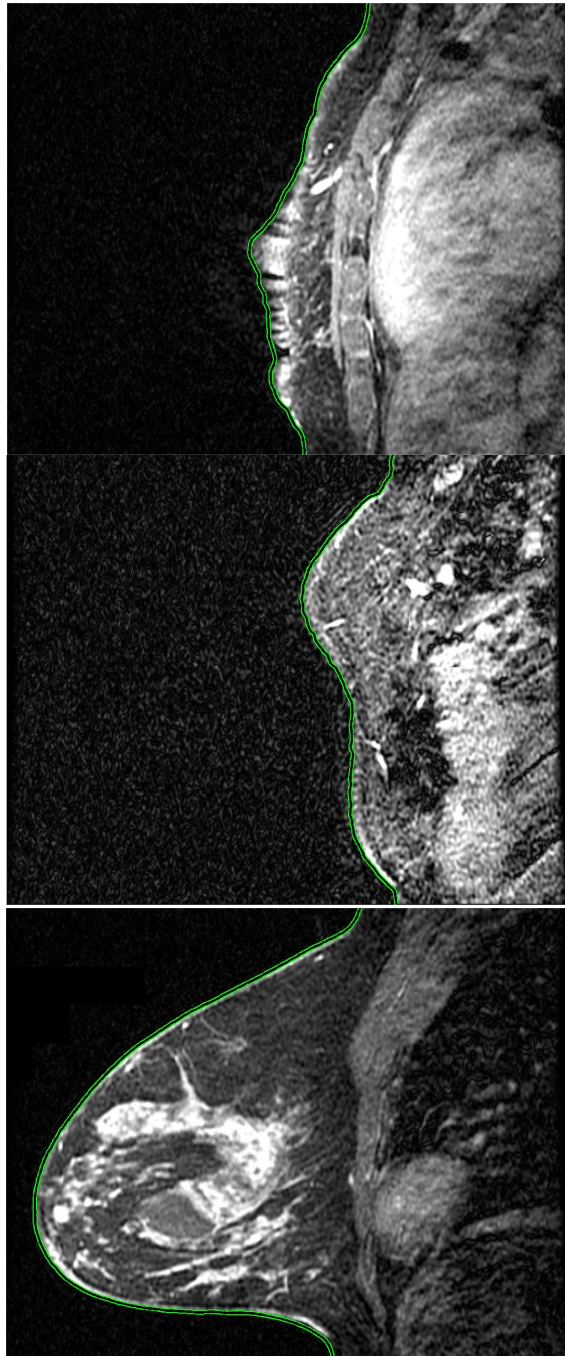


Figure 7.9: Snake method segmentation for different breast MRI slices of patient #01, after: 500 iterations(left); 1250 iterations (middle, right)

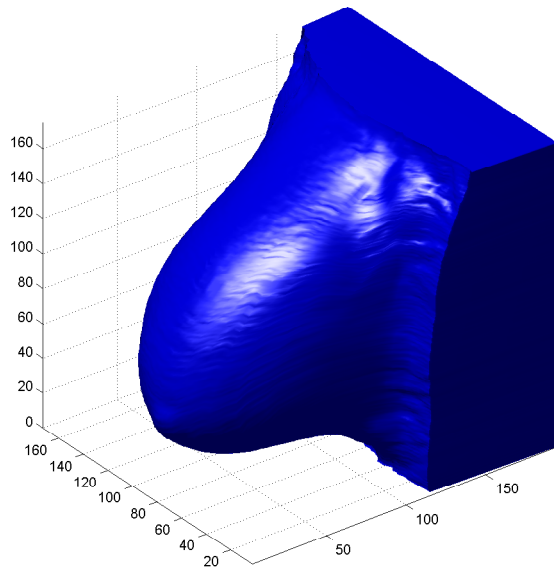
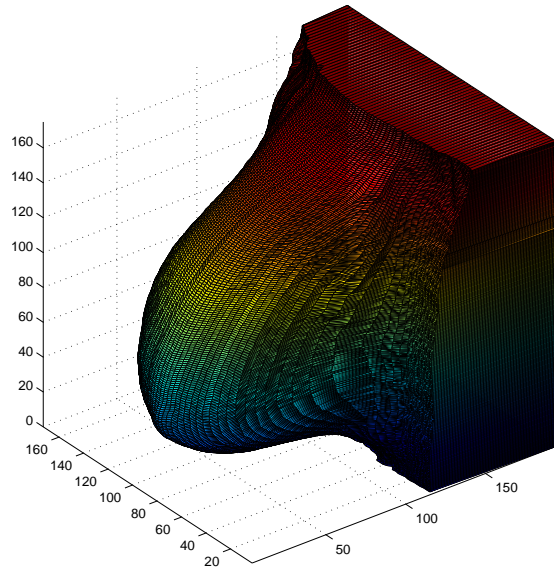


Figure 7.10: 3D breast reconstruction in MATLAB<sup>TM</sup> after segmentation of the DICOM stack

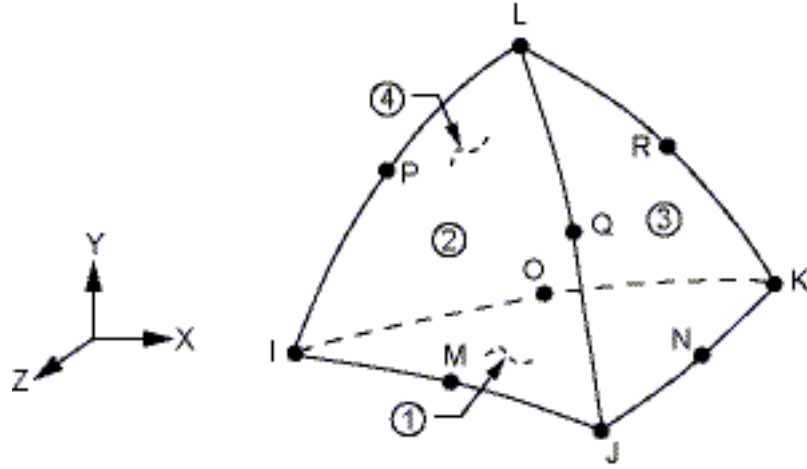


Figure 7.11: SOLID187 elements of ANSYS<sup>TM</sup>

The boundary conditions imposed for our model are the following:

- the front contour of the breast was left as a free surface - no force or displacement constraints;
- all the other sides of the breast boundary were considered fixed - no displacement allowed.

Based on the literature [32, 108, 100, 121], the Neo-Hookean hyperelastic mechanical model is well adapted for breast tissue deformation, and allows us to keep the number of parameters to the strict minimum. Hence we selected this model to simulate all our breast deformation with the VSB. This model was described in more detail earlier in subsection 2.2.3 of part I. The Neo Hookean hyperelastic material form of strain energy potential is given by equation 2.14. As we can see, in this model, the stiffness matrix which is derived from this energy function, is affected



when the material stretches or the body volume of a solid is varying (compression of the material), this in a non-linear way. The left side of the equation increases energy when the material stretches while on the right side the solid is compressed. These changes are following a non-linear behavior, the tissue being dramatically stiffer when the strain increases. For reference purposes, we can relate the shear modulus  $\mu$  and the bulk  $K$  to the Young modulus  $E$  and the Poisson ratio  $\nu$  of the classical linear elastic theory with the following relationship:

$$\mu = \frac{E}{2(1 + \nu)} \quad \text{and} \quad K = \frac{E}{3(1 - 2\nu)} \quad (7.1)$$

We considered the breast tissue to be isotropic homogeneous with an uniform density. However the design of the VSB leaves the ability to use the tissue heterogeneity feature as an available option.

This mechanical model was used to output the deformation shape of the breast for different loading conditions, with the goal to simulate BCT operation. As mentioned in subsection 7.2.1, breast MRI is acquired in the prone position, we then adjust gravity in order to obtain the breast shape for the standing position. The adjustment of position required is illustrated in figure 7.12. We hypothesize that the BCT operation was performed with a breast shape under no gravity load: unloaded shape. To obtain this result the BCT mechanical modeling for breast MRI was decomposed into three steps:

1. breast deformation from prone to unloaded;
2. tumor resection from the unloaded shape;
3. breast deformation from unloaded to standing.

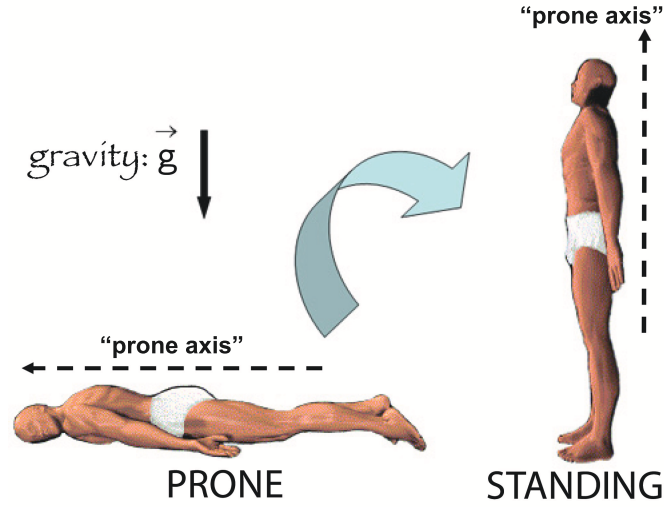


Figure 7.12: Illustration of the prone and the standing position in regards to gravity direction (Image modified from [67]). Note that the “prone axis” is always attached to the patients body.

#### 7.2.2.2 Prone to unloaded

We seek to output the shape of the unloaded breast; therefore it is necessary to first reverse the gravity loading before proceeding with the tumor resection. As we highlighted earlier, The MRI data is acquired while the patient is in the prone position (see figure 7.12). The first computation is to reverse the gravity loading perpendicular to the “prone axis” to obtain a coarse approximation of the unloaded shape. We presume that in the initial prone position the tissue is stress free. We assume that initial stress does not have a major impact on the final deformed shape. This hypothesis is reasonable in the sense that this study focuses on comparison

between computations without virtual surgery and with virtual surgery, hence the emphasis of getting a very accurate unloaded shape may not be relevant since both computations, with or without virtual surgery performed, underwent the exact same hypothesis in regard to the initial stress status. Also, one can improve that method and skip that computational step by using a floating device during MRI acquisition [108] in order to acquire directly the unloaded shape. Once we obtain the unloaded shape we can perform virtual surgery on the breast model.

### 7.2.2.3 Virtual surgery

During the BCT surgery, the surgeons remove the tumor from the breast. As mentioned earlier, we assumed the removed tumor is spherical. Also, we assumed that the following operation is performed from an unloaded position, therefore we perform the virtual surgery from the unloaded geometry. The radius of resection is denoted  $R_T$  and the sphere center coordinates  $(X_T, Y_T, Z_T)$ . We defined three different conditions available to be set on the void left by the surgery intervention:

1. leave the resection void with a free surface boundary at the wound edge;
2. fill the resection with a liquid like behavior material that is incompressible and has very low stiffness;
3. apply some stress at the wound edge with positive or negative hydrostatic pressure.

Each one of these conditions is intended to simulate a specific stage of the recovery, respectively:

1. immediate stage after surgery and/or draining the seroma from the resected cavity;
2. lumpectomy filled with seroma and/or a breast implant;
3. dilatation of the wound due to the accumulation of inflammatory fluid or contraction of the wound due to the scarring process.

The VSB allows us to simulate each of these options, providing different outcomes and reactions to the BCT surgery outcomes. The surgeons have the ability to visualize worst case scenarios and decide from experience.

#### **7.2.2.4 Unloaded to standing**

In order to simulate the outcome of the surgery, we computed the gravity effect on the breast unloaded shape after the virtual surgery was done. We computed the gravity corresponding to the patient in the standing position (see figure 7.12). This corresponds to a gravity in the direction parallel to the “prone axis”. We performed the same simulation on the breast from the unloaded shape with no virtual surgery as well. For both breasts, we assumed that the unloaded shape is stress free. The breast geometry that did not undergo the virtual surgery was used as a control/reference shape. This provided a powerful tool to compare the impact of surgery.

At the end of the day, such a tool will allow patient and surgeons to get the outcome

of BCT procedure and debate on whether or not this is the best solution. The output of this toolbox so far will provide the users with 3D geometry visualization, and the displacement values of manually placed marker. The results will be presented in section 9.1 of chapter 9.

## Chapter 8

# Building surgical indicators

Assessing a 3D shape of the breast is very subjective to variation in regards to the environmental conditions i.e. lighting, orientation, visualization device, as well as the personal judgment of the operator [33]. The alternative using visual features such as marker displacement, could improve the rating of surgery impact. Nevertheless providing visual output will never fulfill the purpose of such a study, as it is time consuming, requires observations skills, and it will rely on the subjectivity of personal judgments. In order to address this issue we propose to build indicators rooted on scientific basis providing a more robust quantitative measurement. Further, the mechanical model provides much more information since we have access to the displacement and the mechanical stress across the complete volume of the tissue. We redesigned the VSB as such that it includes two indicators as an output: the cosmetic and the functional indicator (see figure 8.1). Building indicators seems to

be the best output the VSB could provide. Indicators are widely used and understood by clinicians, they allow classification of patients into different groups with increasing potential risk and a posteriori can be tuned using a greater pool of data. In this chapter we are going to describe our method and hypothesis to derive the cosmetic indicators in section 8.1, and the functional indicator in section 8.2 .

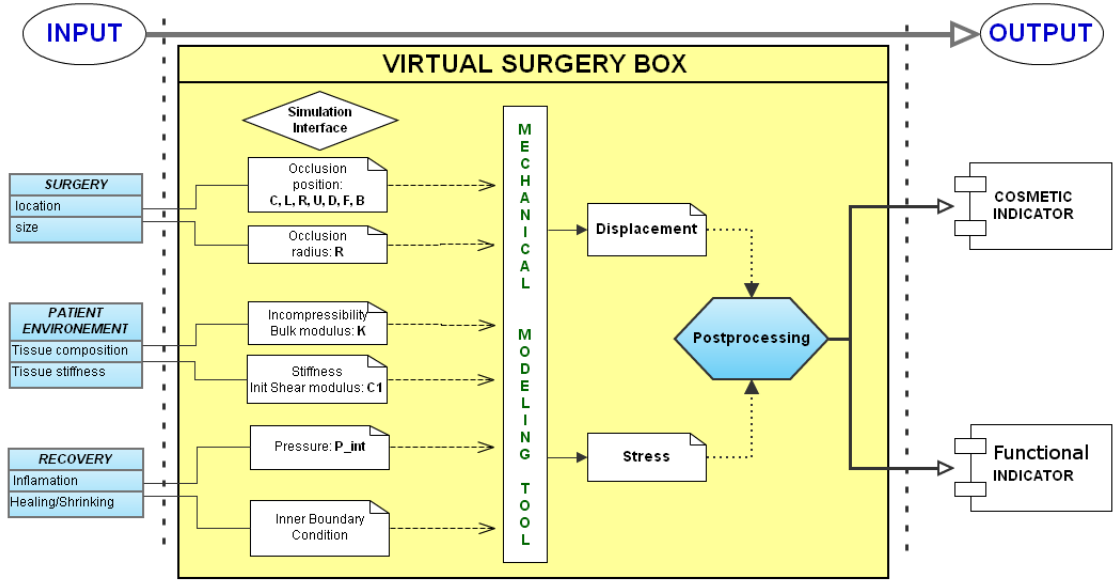


Figure 8.1: Virtual surgery box illustration.

## 8.1 Cosmetic indicator

Aesthetic outcome is a major issue in breast cancer treatment when it comes to quality of life. Although the aesthetic rating of a breast is subjective, this issue needs to be addressed for the sake of the patient's psychological welfare. Waljee et

al. [141] highlighted this in their psychological study, adding that symmetry of the breast played an important role on quantifying breast cosmetics.

In order to provide an assessment of BCT surgery impact on cosmesis we built a cosmetic indicator based on the following hypothesis:

- The shape without virtual surgery is considered as the ideal cosmesis outcome;
- Preservation of symmetry is required in order to keep cosmesis acceptable;
- Loss of symmetry localized near the nipple of the breast has more negative impact on the cosmesis overall grading than at the periphery.

We report mathematically these assumptions into a cosmetic indicator as follows. Let  $\mathbf{f}_S$  be a three-dimensional vector function, representing the displacement in the the breast along a defined path  $S(t)$  with a parametric representation  $t \in (0, 1)$ . We set the following norm:

$$N_\omega(\mathbf{f}_S) = \int_{[0 \ 1]} \|\omega(t) \cdot \mathbf{f}_S(t)\|_1 dt$$

with  $\omega(t) = e^{-\frac{(t-0.5)^2}{\sigma_0}}$  and  $\sigma_0 = 0.05$ .

$w$  is a weight function that emphasizes the role of symmetry and geocentricity of aesthetics shapes.  $\sigma_0$  expresses the rate at which peripheral cosmetic defects influence, overall, the indicator. The path is defined such that the value at  $t = 0.5$  coincides with the nipple location. We concentrated on two specific paths. We choose the path to be an intersection of the sagittal or axial plane with the skin surface.



In this paper, the central tumor resection center  $(X_T, Y_T, Z_T)$  relative to each patient, was chosen to be in the same sagittal or axial plane location. In principle, this may minimize the cosmetic defect. If  $\mathbf{f}_S^0$ , (respectively  $\mathbf{f}_S^l$ ) defines the displacement function along  $S$  before lumpectomy (respectively after lumpectomy) then the distance:

$$CI = N_\omega(\mathbf{f}_S^l - \mathbf{f}_S^0) \quad (8.1)$$

gives a simple quantitative indication on the cosmetic impact of surgery. This quantity will be, for now, our definition of a *cosmetic indicator*. We expect that the greater the cosmetic indicator is, the greater the impact of surgery on aesthetic form should be.

We may modify this indicator by considering other paths or weight functions. It would be interesting to take into account additional criteria, for example, if the tumor location was far from the sagittal plan that it intersects the nipple. Optimizing the definition of that cosmetic indicator will be the topic of a further study that requires more patients' data enrolled in a clinical trial.

## 8.2 Functional indicator

Like most surgical procedures, lumpectomy has an impact on the functionality of the breast in regards to mobility, pain presence, and healing. Vries et al. [34], reported that breast pain occurs in the majority of women after BCT intervention. The intensity is low and decreases with time. Although it is expected that surgery is

followed by pain, the time range reported by this study, in average 36 to 54 months after surgery, goes beyond our expectation. Sources of pain has been investigated in different studies unrelated to breast itself, such as tissue healing or bone fracture. Xu et al. [146] introduced a multiscale model relating the biothermomechanics of skin tissue that establishes a correlation between the pain process and mechanical stress. In another study, Li et al. [140] study the correlation of mechanical factors with gallbladder pain. They reported that, the normal stress peak total may be used as an effective pain indicator for gallbladder pain. Their study includes 37 patients, showing a success rate of 88.2% in positive pain prediction. On an other hand, Javierre et al. [70, 71] developed a healing model that uses the mechanical stress as a triggering mechanism for wound contraction. This later study highlights the potential impact of stress due to surgery on post-surgery healing.

We intend to take advantage of the VSB simulation to supervise how lumpectomy affects the anatomy at the mechanical stress level. In regards to previous observations, stress could provide some understanding in the source of pain as well as lumpectomy healing. This investigation would be a first in this area. We build a functional indicator assessing the impact of BCT on pain and healing based on the following hypothesis:

- The mechanical stress map before virtual surgery is considered as the ideal functional outcome;
- The gradient map of stress before virtual surgery contributing to the ideal functional outcome.

We will now translate mathematically this general idea of a functional indicator linked to mechanical stress. As before, we restrict our indicator to vector functions in the sagittal or radial planar domain  $\Omega$  inside the breast that intersects the nipple. Let  $\mathcal{B}_R(y)$  be a disk of radius  $R$  and center  $y$  in that domain, i.e

$$\mathcal{B}_R(y) = \{x \in \Omega \text{ such as } |x - y| \leq R\} \quad (8.2)$$

Let  $f$  and  $g$  be two vector functions defined on  $\Omega$ . We define the scalar product

$$(f, g)_R(y) = \int_{\mathcal{B}_R(y)} f(x)g(x)dx + \sum_{i=1}^2 \int_{\mathcal{B}_R(y)} \frac{\partial f(x)}{\partial x_i} \frac{\partial g(x)}{\partial x_i} dx, \quad y \in \Omega$$

From this scalar product, we define the norm:

$$\forall y \in \Omega, \quad (\cdot, \cdot)_R(y) = \|\cdot\|_R^2(y).$$

Let  $(\sigma_x^0, \sigma_y^0, \sigma_z^0)$  (respectively  $(\sigma_x^1, \sigma_y^1, \sigma_z^1)$ ) the three components of the normal stress inside the breast before surgery (respectively after surgery).

The following scalar indicator

$$D(\sigma^0 - \sigma^1)(y) = \sqrt{\|\sigma_x^0 - \sigma_x^1\|_R^2(y) + \|\sigma_y^0 - \sigma_y^1\|_R^2(y) + \|\sigma_z^0 - \sigma_z^1\|_R^2(y)}$$

provides an average measurement on the change of stress in the disc  $\mathcal{B}_R(y)$ . Our functional indicator  $FI(y)$  provides a relative change of that stress:

$$FI(y) = \frac{D(\sigma^0 - \sigma^1)(y)}{1 + D(\sigma^0)(y)} \quad (8.3)$$

This functional indicator should reveal locations of abnormal changes of the normal stress after lumpectomy.

To get a single scalar value that represents the worst stress value, we will use the maximum norm of that indicator inside the breast:

$$|| FI(y) ||_{\infty}.$$

As noted earlier, this a priori indicator of mechanical stress might be fine tuned with conducting a clinical study involving a large number of patient's feedback, thanks to statistical analysis.

# Chapter 9

## Results & discussions

The impact of BCT was simulated on four different breast geometries coming from three patients. These patients were women with breast cancer who have elected to undergo BCT and are being treated at the Methodist Hospital in Houston, TX. In table 9.1, we detail some of the characteristics of each patient with respect to age, anatomy, relevant MRI image specification, as well as the number of meshes used in the mechanical model later on. Each computation was performed with less than 50000 elements, and the default values for the material constant were as such:

- initial shear modulus  $\mu = 1677 \text{ Pa}$ ,
- bulk modulus  $\kappa = 83333 \text{ Pa}$ ,
- tissue density  $\rho = 1000 \text{ kg.m}^{-3}$ .

As mentioned earlier, a fairly large distribution of these parameters values were found in the literature. According to (7.1), these  $(\mu, \kappa)$  values correspond to a Young modulus  $E = 5000 \text{ Pa}$  and a Poisson ratio  $\nu = 0.49$ . The Poisson ratio being very close to 0.5 describes this tissue as highly incompressible. The Young modulus being very low, describes the tissue as having very low stiffness. For reference  $E$  would be in the range 0.01 to 0.1 GPa for rubber.

We simulated the BCT operation for each of these patients, and the results are presented in two different sections. In section 9.1 the raw product from the VSB with no extensive post-processing is outputted, displaying three-dimensional breast shape after BCT, and the curve of the marker displacement. On section 9.2, the result obtained from the cosmetic indicators is displayed. In this later section, a sensitivity analysis on the input parameters was conducted and the results we obtained are discussed.

Table 9.1: Patient's specification

	Patient # 01	Patient # 02	Patient # 03 L	Patient # 03 R
Label	P01	P02	P03L	P03R
Age	50	65	72	72
Breast side	RIGHT	LEFT	LEFT	RIGHT
Pixel spacing ( $mm$ )	0.4297	0.7813	0.664	0.664
Y pixel spacing ( $mm$ )	2.4	0.7813	0.664	0.664
Z pixel spacing ( $mm$ )	0.4297	2	1	1
Model volume ( $mm^3$ )	3222	2895	2978	3118
Mesh size	47000	41000	42901	44428
MRI acquisition plan	sagittal	axial	axial	axial

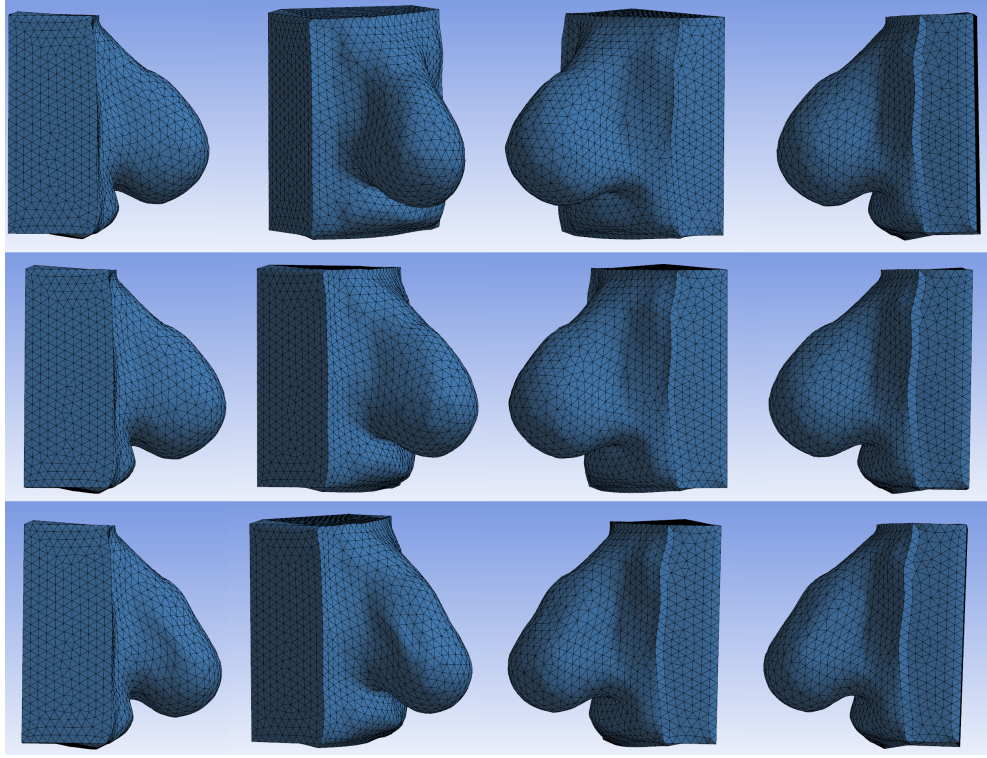


Figure 9.1: Breast shape of patient # 02. Top row: before surgery; middle row: resection radius  $R=15\text{mm}$ ; bottom row: resection radius  $R=35\text{mm}$ ;

## 9.1 Vizualization results

This section provides some vizualization output results of the BCT simulation. Although it is difficult to provide a judgment on visual observation of 3D snapshots we can see in figure 9.1 the impact of lumpectomy for two different resection sizes for patient P02. We denoted that after lumpectomy the breast has a more elongated shape, leading to the accentuation of a bump deformity.

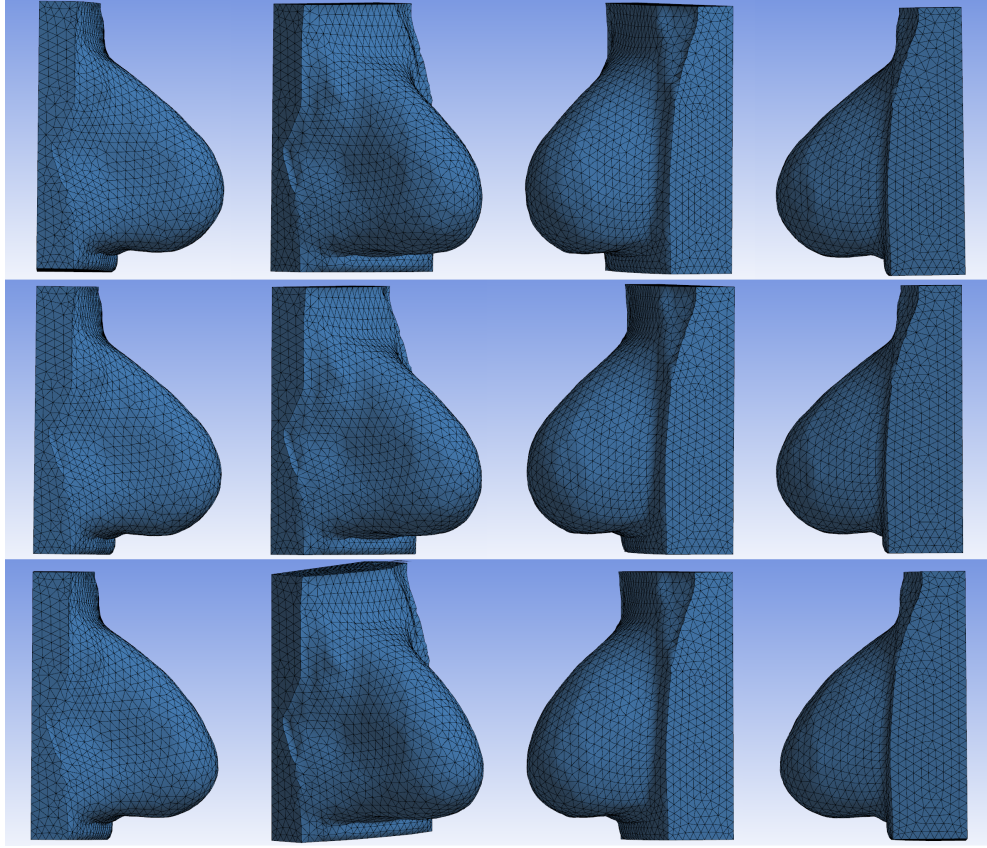


Figure 9.2: Breast shape of patient # 03 R. Top row: before surgery; middle row: resection radius  $R=15\text{mm}$ ; bottom row: resection radius  $R=35\text{mm}$ ;

This visual defect observation is not visible in an obvious manner for every patient. Figure 9.2 represents the breast shape after lumpectomy for different resection volumes on patient RP03. In this case, it is less obvious to highlight a difference between the shapes, although we can still guess an overall more concave shape of the breast with a higher resection volume. Figure 9.3 superposes the 2D deformed shape on the sagittal plan of the breast before and after surgery for each patient for a centered tumor resection of radius  $R = 35\text{mm}$ . As we can see, the effect of surgery



is more highlighted, indeed we can observe that for each case the birth of a bumpy shape at the top, leading to an overall more elongated shape.

Fig. 9.4 represents the displacement difference on the “prone axis” (parallel to gravity direction) between the breast, before and after surgery for the 3 patients. Patient PO3, presents quantitatively very similar results for both breasts. However, the pattern of deformation for patient PO3 is rather different than for patient PO1 and PO2 as shown in figure 9.4. Although a difference in the amplitude is observable between both patients PO1 and PO2, the displacement for the two patients follows the same pattern. In other words, the location of local minima and maxima of the displacement, are very similar for both patients PO1 and PO2, provided that the tumor location relative to the breast stays similar. However this was different for PO3.

In order to visualize where these points stand, we picture the location of the reference points on the breast surface. Figure 9.5 illustrates the local minima, maxima, and fixed point locations attached to the tissue on the patients’ breast, as well as the direction of deformation compared to an untreated breast. Interestingly we note that the parts more likely to create a visible unaesthetic shape are the 3 top markers. From this, we can assume that a bump will appear on the top part of the breast. In the meantime, a concavity will appear on top of the nipple area. This technique may provide a rational method for choosing tracking points. The implies is that patients can be classified into categories that will have similar cosmetic surgery outcomes on the basis of the input parameters of our VSB.

Although computer visualization can provide a model of the breast surface, we are

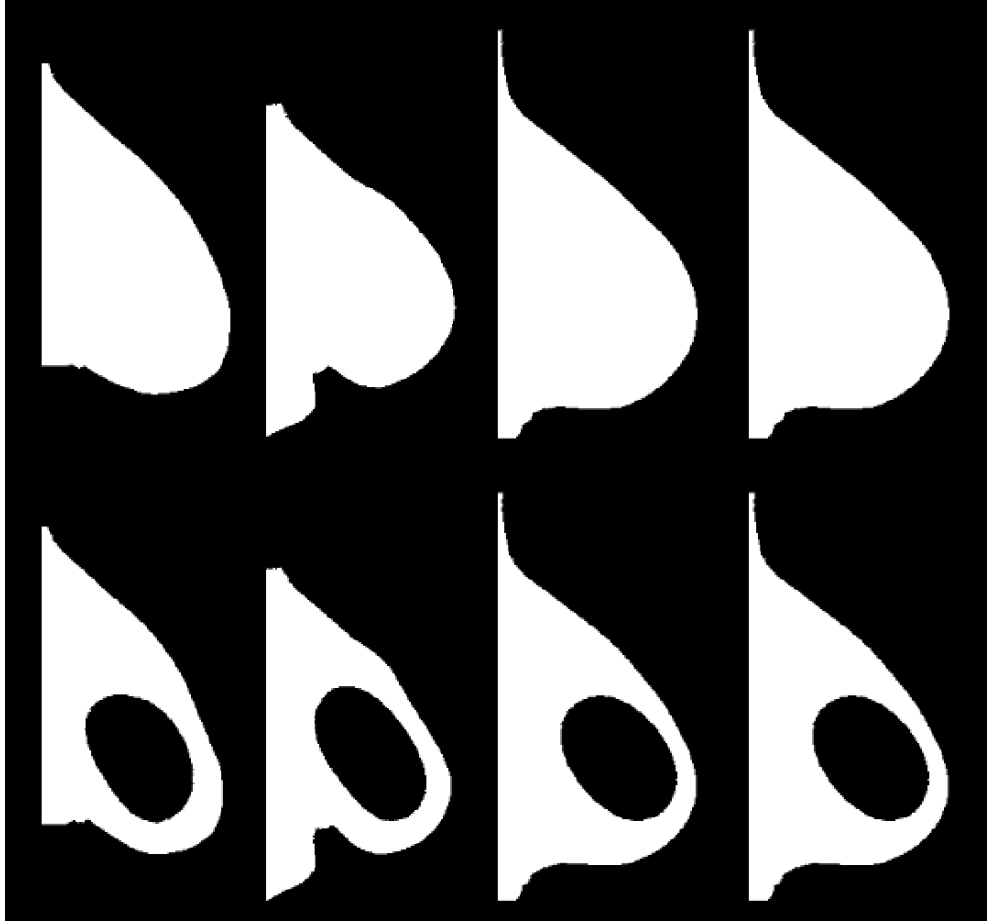


Figure 9.3: Breast deform shape on a sagittal plan (from left to right) P01, P02, RP03, LP03 for a resection radius  $R=35\text{mm}$ .

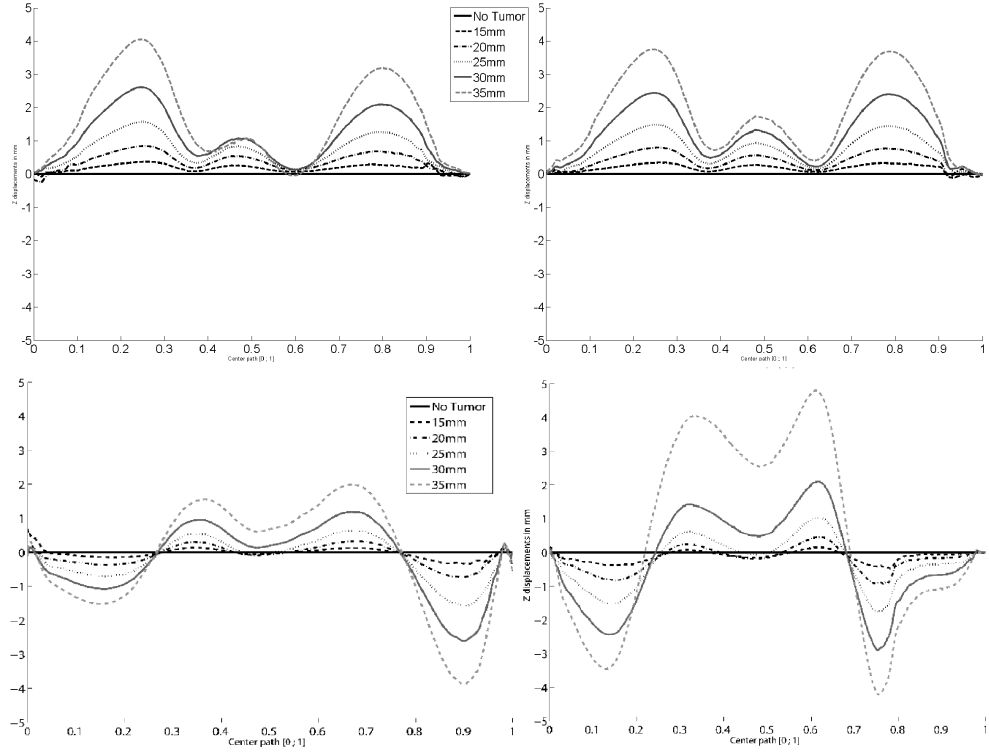


Figure 9.4: Displacement difference on gravity loading direction of breast before and after BCT operation for the different tumor size of (top left) LP03, (top right) RP03, (bottom left) P01, (bottom right) P02. Sagittal plane

looking for a quantitative measurement that will be less subjective. Computing the displacement of a specific plan, or specific points to track the motion between the shape before and after surgery appears to be helpful to provide some premium analysis. Nevertheless providing visual output will never fulfill the purpose of such a study, as it is time consuming, requires observations skills, and it will lie under the subjectivity of personal judgments. In the next section we will perform an analysis on the VSB input, outputting the sensitivity of the indicators.

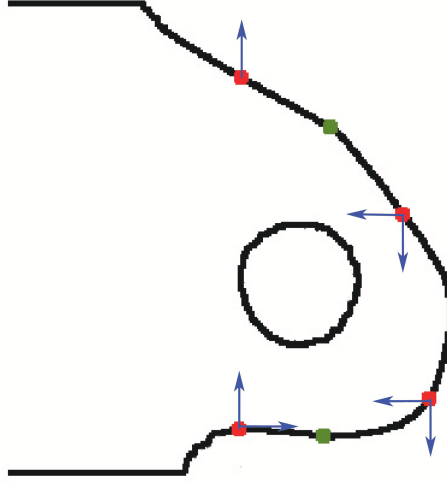


Figure 9.5: Breast deformation pattern after BCT operation; (red) local minima and maxima points, (green) fixed points.

## 9.2 Sensitivity analysis for the VSB input

We are going to, separately, test the impact of various parameter inputs of the VSB for breast patient data listed in table 9.1. If not specified otherwise, the tumor resection will be: (i) of radius  $R_T = 30mm$ , (ii) localized at the center of the breast, (iii) empty therefore its boundary will be considered as a free surface.

Specifically for the functional indicator computation we select  $R = 10mm$  for the disk radius in equation 8.2. The radius was chosen to be large enough to deal with the finite element mesh we use, and small enough to provide some localized information. In our study, we notice significant spatial variability on mechanical stress distributions among subjects. For instance, figure 9.6 represents the functional indicator plot for patient #01 for a tumor resection size  $R_T = 30mm$  at the center of the plane cut. As we can see, the surrounding of the tumor resection seems highly

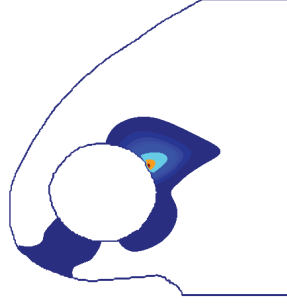


Figure 9.6: Pain indicator contour for a tumor resection size  $R_T = 30$  mm on P01. Sagittal plane. Scale map from dark blue to red:  $[1, 2, 5, 10, 15, 20, 50, 100, 140]$ .

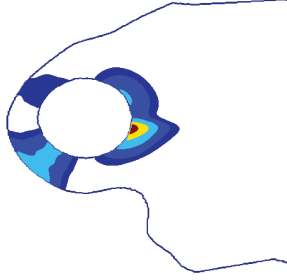


Figure 9.7: Pain indicator contour for a tumor resection size  $R_T = 30$  mm on P02. Sagittal plane. Scale map from dark blue to red:  $[1, 2, 5, 10, 15]$ .

solicited, with a peak at the top of the breast resection near the angle  $\pi = 140$ . After conducting, a similar analysis for patient #02, the computation of the functional indicator gives a completely different spatial distribution as shown in figure 9.7: although only the surrounding of the tumor resection is still the most solicited, the peak stays at the angle  $\pi = 18$ , and its magnitude is one order of magnitude less for patient #01. For this reason, when studying the functional indicator, we output only the maximum norm value of the function indicator  $\|FI\|_\infty$ .

### 9.2.1 Sensitivity analysis

#### Test 1 - Influence of tumor position

When describing the location of a breast lump, the breast can be subdivided into four quadrants:

- UOQ - Upper Out Quadrant
- UIQ - Upper Inside Quadrant
- LOQ - Lower Out Quadrant
- LIQ - Lower Inside Quadrant

Each quadrant is further subdivided using the clock face model, see figure 9.8. The 12 o'clock position is above the nipple and the 6 o'clock position is below the nipple. Care must be used when describing the location of a lesion in the right vs. the left breast. In this test, the sensitivity of lumpectomy to the quadrant location will be studied. We will perform these simulations for a tumor resection of radius  $R_T = 20mm$ .

Figure 9.9, represents the plot of the cosmetic indicator as a function of the quadrant location of a tumor resection of radius  $R_T = 20mm$  respectively for the sagittal and axial plane. The Lower Inside Quadrant (LIQ) scored the highest whereas a centered resection will have the most satisfactory cosmetic impact.

Figure 9.10, represents the plot of the  $\|\cdot\|_\infty$  norm of the functional indicator as a function of the quadrant location of the tumor resection for the 3 patients (P01 P02,

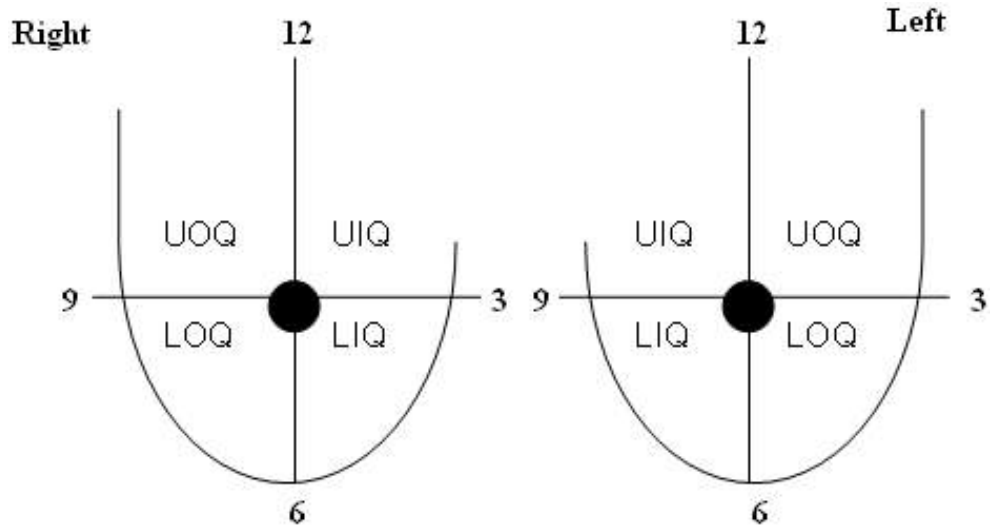


Figure 9.8: This schematic drawing demonstrates the four quadrants of the breast: upper inner quadrant (UIQ), upper outer quadrant (UOQ), lower inner quadrant (LIQ), and lower outer quadrant (LIQ). The clock face model is superimposed on the four quadrant model to demonstrate how each breast is subdivided within the quadrant model.

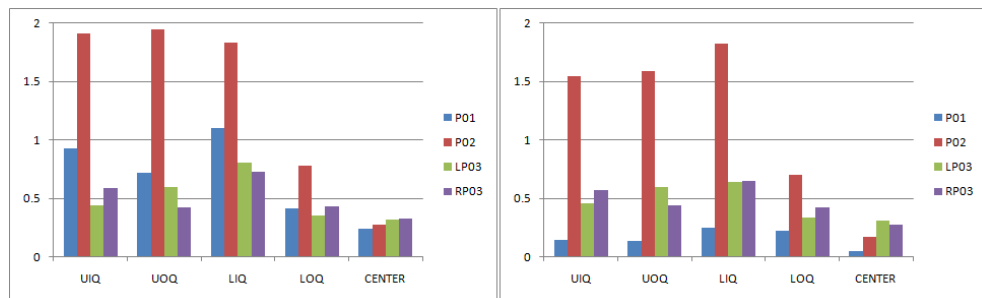


Figure 9.9: Cosmetic indicator as a function of the quadrant location of a tumor resection of radius  $R = 20mm$ . Left: Sagittal plan; Right: Axial plan

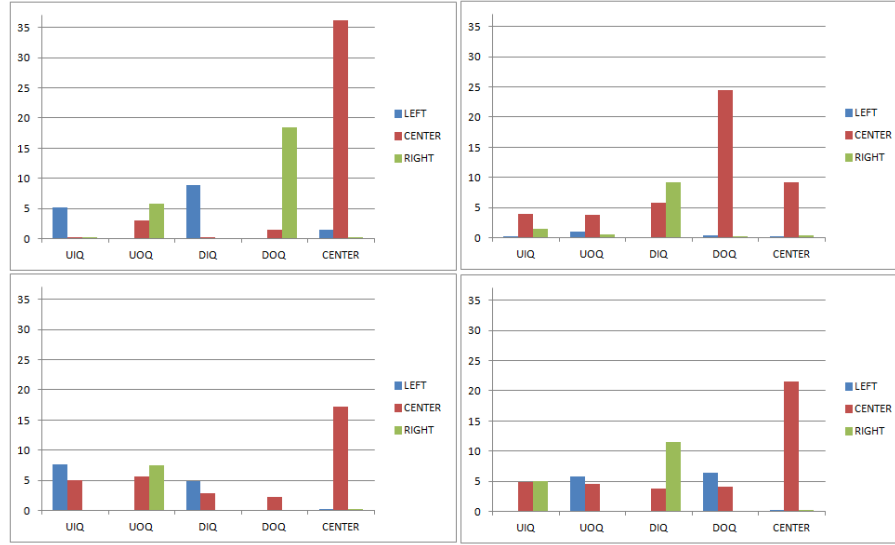


Figure 9.10:  $\|\cdot\|_\infty$  norm of the functional indicator as a function of the quadrant location - Test 1; From right to left top to bottom: P01, P02, PL03, PR03.

PL03, PR03) on the sagittal plan. We observe that although we have a general trend to get higher results for a centered tumor, there is no real general tendency, neither there is a standard of amplitude of the functional indicator. This test carries two observations: the first is that we are facing a limitation on the number of patients and a higher pool of patients is required to be able to conclude on any particular finding; second this highlights the necessity of such a tool due to the unpredictability of behavior for each patient in regards to the tumor position.

## Test 2 - Influence of the occlusion size

In 1995, Taylor et al. [134] investigated the factors that qualify to be considered a good cosmetic outcome for BCT. Obviously, it appeared that poorer cosmetic



Radius ( $mm$ )	15	20	25	30	35
Volume ( $cm^3$ )	14.14	33.51	65.45	113.10	179.59

Table 9.2: Radius ( $mm$ ) and corresponding volume ( $cm^3$ ) of the occlusion that have been tested.

outcomes were obtained with increasing volume of breast removed. In this test, we explore the impact of surgery for different tumor sizes. We considered only spherical occlusion shapes and varied the occlusion radius. We vary the radius from 15  $mm$  to 35  $mm$  corresponding to a resection volume varying from 14.14  $cm^3$  to 179.59  $cm^3$  as in table 9.2.

Figure 9.11, represents the plot of the cosmetic indicator as a function on the radius of the tumor resection for 3 patients, respectively, on the sagittal and axial plan. We observe that the greater the radius the greater the cosmetic indicator is. Although this could have been easily predicted, it is interesting to observe that the effect on the cosmetic indicator has a steep non-linear growth.

Figure 9.12, represents the plot of the  $\|\cdot\|_\infty$  norm of the functional indicator as a

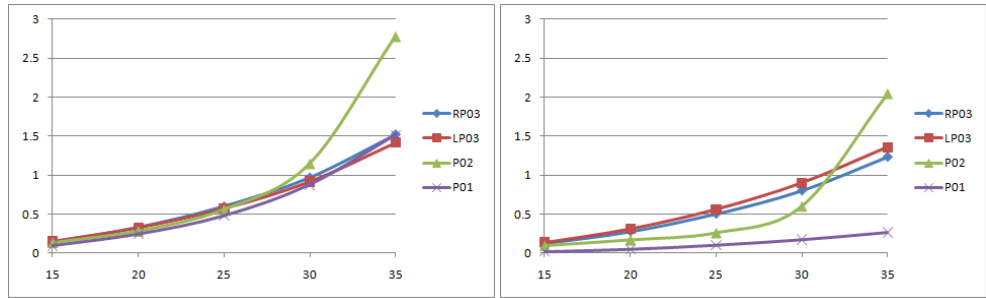


Figure 9.11: Cosmetic indicator as a function of the tumor resection size  $R_T$  (in  $mm$ ); Left: Sagittal plan; Right: Axial plan.

function of the radius of tumor resection for each patient on the sagittal plan. We

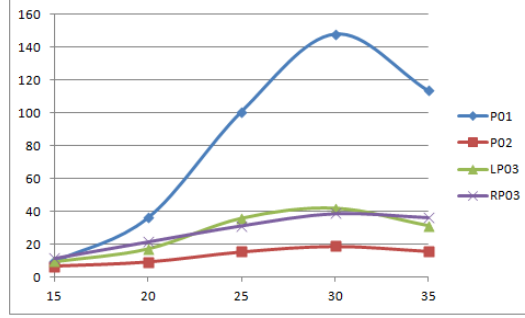


Figure 9.12:  $\|\cdot\|_\infty$  norm of the functional indicator as a function of tumor resection radius - Test 2; Sagittal plan.

observe that the greater the radius, the greater the functional indicator is, nonetheless it decreases after a certain radius. Although we can see that the behavior is similar, the amplitude is patient-related.

### Test 3 - Influence of tissue compressibility

Tissue characteristics vary between different patients, and more specifically, between different patient age groups. Tissue characteristics could explain the fact younger age groups have a better cosmetic outcome[134, 12]. We explore how tissue compressibility could affect the outcome. The compressibility of a material in the mechanical model we are using, the neo-Hookean model, is characterized by the bulk modulus  $\kappa$ . The higher the bulk modulus is, the more it penalizes the energy function, the less it allows a volumetric difference change into the material. In this study, we will test the influence of changing the bulk modulus  $\kappa$  between 0.015 MPa and 1 MPa on the surgery outcome. For reference the bulk modulus for air averages 0.1 MPa while

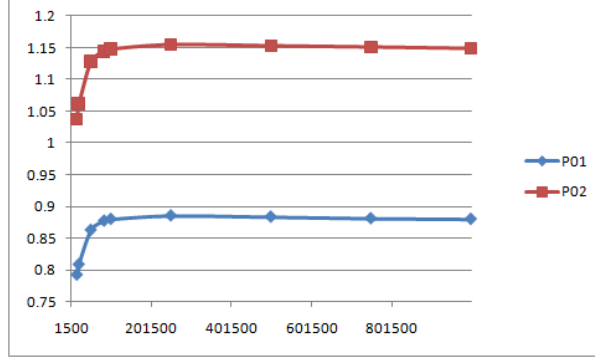


Figure 9.13: Cosmetic indicator as a function of the bulk modulus  $\kappa$  (in Pa) for patient #1 and #2. Sagittal plan

the bulk modulus for water(incompressible material) is  $\sim 200$  MPa.

Figure 9.13 represents the cosmetic indicator for two patient cases as a function of the bulk modulus for a tumor resection with a radius  $R_T = 30mm$ . As we can see for a lower bulk modulus, the cosmetic indicator remains lower. However above  $\kappa = 100$  KPa there is no noticeable effect. Furthermore, the overall variation of the cosmetic indicator is only about 10%, suggesting that tissue compressibility has no major impact on the aesthetic outcome.

Figure 9.14, represents the plot of the  $\|\cdot\|_\infty$  norm of the functional indicator as a function of the tissue compressibility for a tumor resection with a radius  $R_T = 30mm$  for 2 patients (P01 and P02) on the sagittal plan. In Figure 9.14 we observe that increasing the bulk modulus leads to an increase of the functional indicator. The increase rate is low and converges to a plateau. The overall variation of the cosmetic indicator is only about 15%, suggesting again, that tissue compressibility has no major impact.

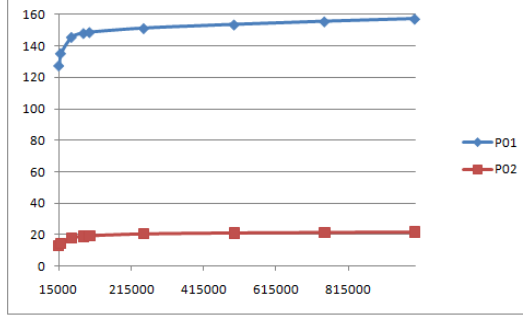


Figure 9.14:  $\|\cdot\|_\infty$  norm of the functional indicator as a function of the tissue compressibility - Test 3; Sagittal plan.

These observations could result in upgrading the VSB design by fixing,  $\kappa$  parameter. This is a suggestion that needs to be validated only after launching a whole study on a greater pool of patients.

#### Test 4 - Influence of tissue stiffness

Following the same reasoning from above, we explore the effect that stiffness has on changing the surgery outcome. The stiffness of the material in the neo-Hookean model is represented by the shear modulus  $\mu$ . When  $\mu$  is increased, the energy function gets more sensitive to stretch in the material principal direction. Therefore, the higher  $\mu$  is, the stiffer the material will be. In the literature, a stiffness of 5 kPa is the average right order of magnitude [100, 108, 109, 110, 32]. To study the stiffness influence, we will vary the initial shear modulus  $\mu$  from 1.3 kPa to 6 kPa.

Figure 9.15 represents the cosmetic indicator for two patients as a function of the initial shear modulus for a tumor resection with a radius  $R_T = 30mm$  respectively

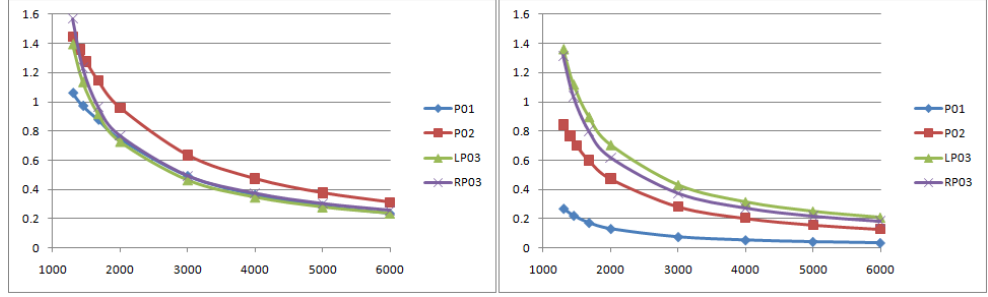


Figure 9.15: Cosmetic indicator as a function of the initial shear modulus  $\mu$  (in Pa); Left: Sagittal plan; Right: Axial plan.

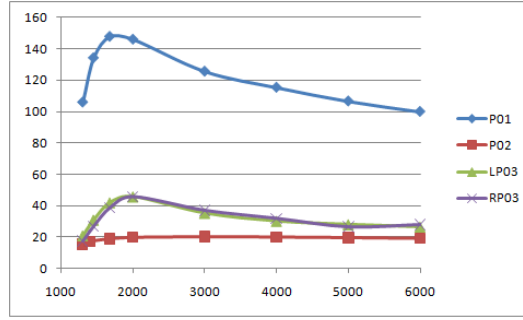


Figure 9.16:  $\|\cdot\|_\infty$  norm of the functional indicator as a function of the tissue stiffness - Test 4. Sagittal plan

on the sagittal and axial plan. We can observe a significant decrease on the cosmetic indicator while the tissue property gets stiffer. Also, it is interesting to highlight that the cosmetic indicator behaves similarly for the sagittal and axial plan.

Figure 9.16 displays  $\|\cdot\|_\infty$  as a function of the compressibility and stiffness of the tissue. As we can see, the functional indicator behavior is similar for each patient. Nonetheless, the amplitude is highly dependent on the patient, suggesting that each breast shape does not agree on the same sensitivity in regards to tissue stiffness.

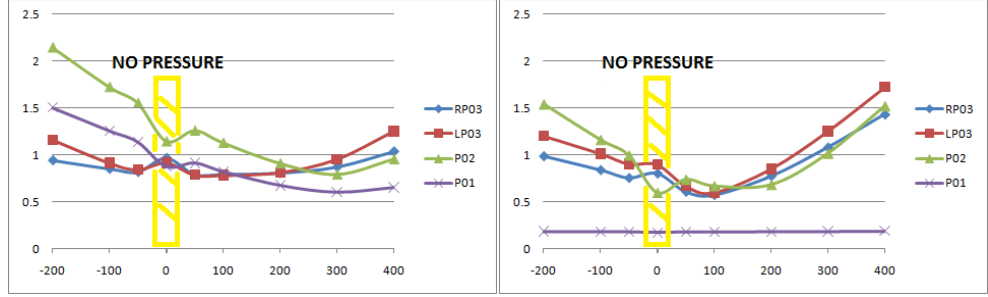


Figure 9.17: Cosmetic indicator as a function of an imposed pressure at wound boundary surface  $P_{wound}$  (in Pa). Left: Sagittal plan; Right: Axial plan.

### Test 5 - Influence of a pseudo-pressure inside the wound:

In order to simulate the potential boundary condition that the wound edge faces after surgery during the recovery process, we imposed an hydrostatic pressure condition at the wound edge. We vary this pressure between  $-300 Pa$  to  $+400 Pa$ . As a side note, the hydrostatic pressure exercised by a fluid such as water on a sphere surface of  $30 mm$  radius is equivalent to  $\sim 100 Pa$ . Positive pressure corresponds to the accumulation of seroma during the inflammation process. Negative pressure will simulate the contraction of scar tissue and overall loss of volume due to fibroblast. Figure 9.17 represents the plot of the cosmetic indicator as a function of the pseudo pressure boundary condition imposed at the tumor resection for both patients. Negative pressure on the wound edge creates damage regarding the cosmetic outcome. However, it is interesting to note that positive pressure can limit the cosmetic outcome.

Figure 9.18 displays  $\|\cdot\|_{\infty}$  of the functional indicator as a function of the hydrostatic pressure imposed at the tumor resection surface. Regardless of the value amplitude

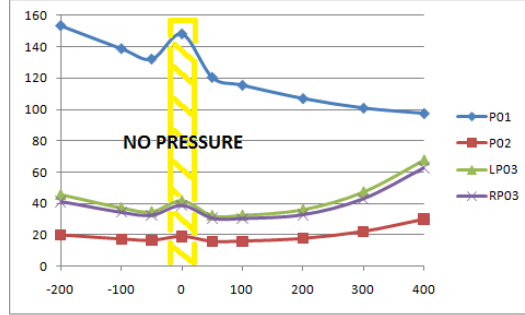


Figure 9.18:  $\|\cdot\|_\infty$  norm of the functional indicator as a function of the hydrostatic pressure at the wound - Test 5. Sagittal plan

specific to each patient, we can observe the same general behavior occurs. The same conclusion of test 4 can be made: each breast has its own sensitivity in regards to hydrostatic pressure at the wound. It is also important to note that in all the sensitivity tests, P01 always scored the highest, suggesting that some patients have some critical responses to BCT surgery and they are more likely to experience post-surgery difficulties.

### Test 6 - Influence of a liquid-filling inside the wound

In order to simulate the post-surgery state in a more realistic way, we simulate the stage where the surgical resection would be filled up with liquid seroma. In order to achieve this, we imposed a very elastic material that has low stiffness  $E = 500$  Pa. In this test we performed the computation for 2 different values of bulk modulus corresponding to a Poisson ration  $\nu = 0.40$  and  $\nu = 0.49$  for an elastic linear model. Figure 9.19 represents the cosmetic indicator values as a function of the Poisson

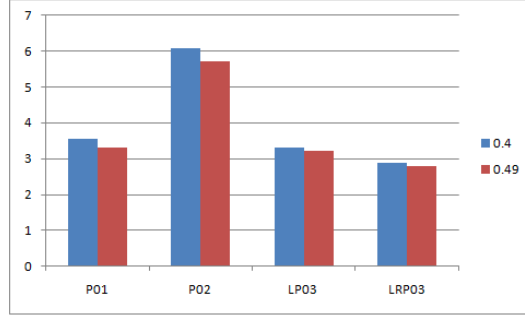


Figure 9.19: Cosmetic indicator as a function of the filling fluid compressibility for a tumor resection of radius  $R = 30mm$ .  $E_{FLUID} = 500Pa$ ; Sagittal plan

ratio of the liquid filling resection of 30mm. We can see that most of these cosmetic indicators exceed the value of 3 which is large in comparison to the average cosmetic indicator value we have seen thus far.

Figure 9.20 represents  $\|\cdot\|_{\infty}$  of the functional indicator as a function of the Poisson ratio of a liquid filling resection of  $R_T = 30mm$ . We can see that patient #01 experienced great values for the functional indicator compared to the other patients. Apart from this, most of these cosmetic indicators exceed the value of 3 which is large in comparison to the average cosmetic indicator value we have. There is no difference between the value of the functional indicator for each patient with two different Poisson ratio values. Leading to the conclusion that the compressibility of the tissue was not a big influence on the outcome of the results.



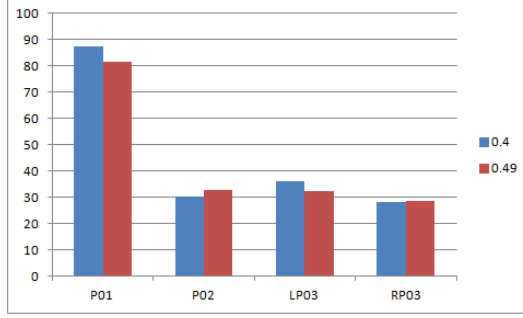


Figure 9.20:  $\|\cdot\|_\infty$  norm of the functional indicator as a function of the filling fluid compressibility for a tumor resection of radius  $R = 30mm$ .  $E_{FLUID} = 500Pa$ ; Sagittal plan

Variation	Resection size $R_T$	Incompressibility	Stiffness	Pressure
$\searrow$	-	-	+	+
$\nearrow$	+	$\emptyset$	-	$\sim$

Table 9.3: Summary of cosmetic indicator behavior in regards to the input parameters.

## 9.2.2 Discussion

The cosmetic indicator was conceived around the hypothesis of preservation of symmetry in regards to pre-surgery shape. Whereas the functional indicator was built taking into account the birth of a stress region as well as the gradient of stress, expressing concern in regards to tissue mechanics and energy re-distribution in the tissue. In table 9.3 we summarize the observations we performed in this study for the cosmetic indicators. This table highlights that BCT is sensitive to the amount of tissue removed and to the stiffness of tissue. This conclusion is consistent with the clinical observation obtained by Taylor et al. [134]. It is important to note that the cosmetic indicator average value was patient specific, meaning that maximum

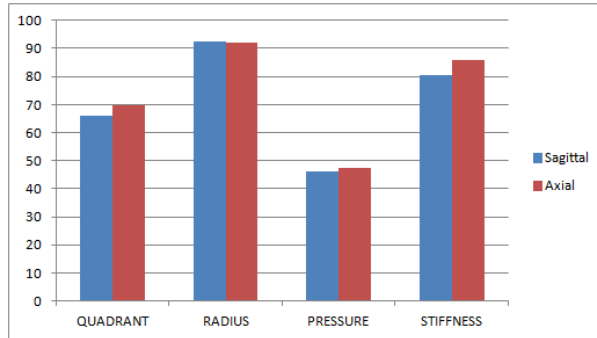


Figure 9.21: Absolute relative impact of parameters on the cosmetic indicator, average value on the 3 patients combined. Blue: Sagittal plan; Red: Axial plan.

amplitude varied significantly among patients. This observation could be explained in many ways. One reason may be the fact that breast volume and shape were quite different among patients. However, in order to correlate the sensitivity of the cosmetic indicator to the input parameter, regardless of the patient, we plotted in figure 9.21 the average value of the relative difference of the cosmetic indicator for each test. We can observe that the volume of the resection, the stiffness of the tissue, and the quadrant location are the input parameters that are the most sensitive with regards to the cosmetic indicator. This result remains coherent with the Taylor et Al. [134] study. Also, we can observe that the cosmetic indicator has the same relative impact whether it is in the sagittal or axial plane, suggesting that the shape is relatively affected in both directions in the same way. Conversely, we still have an unclear picture of the relationship between this cosmetic indicator and the visual results for the breast shape after surgery. Subjectivity on visual outcome can account for one reason, but we need more patient data to further that relationship. It is anticipated that the design of the cosmetic indicator will then be adjusted to straighten that

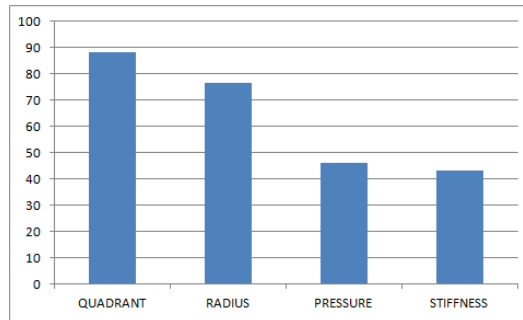


Figure 9.22: Absolute relative impact of parameters on the functional indicator average value on the 3 patients combined. Sagittal plan

relationship.

Regarding the impact of lumpectomy on the functional factor, we observed that the amplitude is strongly dependent on the patient. This could lead us to identify patients that are high risk for eventual recovery in respect to healing and perhaps pain and/or radiotherapy sensitivity. More research still needs to be done to state that stress has, unequivocally, a major impact on healing and that it is highly sensitive to radiation. We plotted in figure 9.22 the average value of the relative sensitivity of the functional indicator in regards to input parameters for all patients. The radius of the tumor resection as well as the tumor location were the most sensitive to this indicator, suggesting that these two parameters can have major impact on healing as well as the functionality/pain of the patient.

Mechanical stress is not easy to assess from medical imaging. This new functional indicator provided by the VSB has the potential to deepen our understanding of the process that leads to successful or unsuccessful cosmetic results.

# Chapter 10

## Multiscale modeling

Thus far we have presented a tool allowing the user to simulate the impact of BCT surgery using a mechanical model. We simulated the recovery process using boundary conditions at the wound, either by simulating a liquid like material or by imposing hydrostatic pressure to model contraction or dilatation. It is expected for the surgical wound to heal, while we believe this process is potentially responsible for post surgery breast deformities experienced by some BCT patients. In this chapter we propose a new method to implement a healing model combined with the mechanical simulation of the VSB. This implementation will constitute a two-time scale model, (1) combining the mechanical model, describing the behavior at the macroscopic level, (2) and combining a CA model of healing, describing the wound recovery at the microscopic level. In section 10.1 a description of this two-time scale model will be given. In section 10.2 we will present the healing model we used. Finally, in section 10.3 results of our simulation will be given.

## 10.1 Two-time scale model

Wound healing mechanism involves complex interactions between the biological, chemical, and mechanical processes. A multiscale model was designed that uses the interaction between the mechanical and the healing process. Tissue generated at the cellular level influences the mechanical deformation of the breast by modifying the tissues distribution, simultaneously the deformation induces mechanical stress along the wound edge that is a function of the shape of the breast and the geometry of the wound. Our computational approach is summarized in figure 10.1. We start from an initial unloaded position of the breast with a known geometry of the tissue resection inside the breast. From this initial condition, we compute the displacement and mechanical stress using our mechanical model. The healing model operates on the unloaded configuration of the breast and takes into account the map of stress distribution. From this new shape of the breast in the unloaded position, we apply the soft tissue mechanical model to get the new displacement and mechanical stress under gravity load. This procedure is repeated for a number of cycles until the internal cavity is closed. This procedure as been detail in algorithm 4. This model presents two scale levels:

1. temporal scale, while the tissue mechanic is approached as quasi continuous transformations, the healing takes over an extended period. In our model a time step of the wound healing model will correspond to the cycle time of a cell  $> 24$  hours. The healing process itself lasting over several generations of a cell, e.g. about one week.

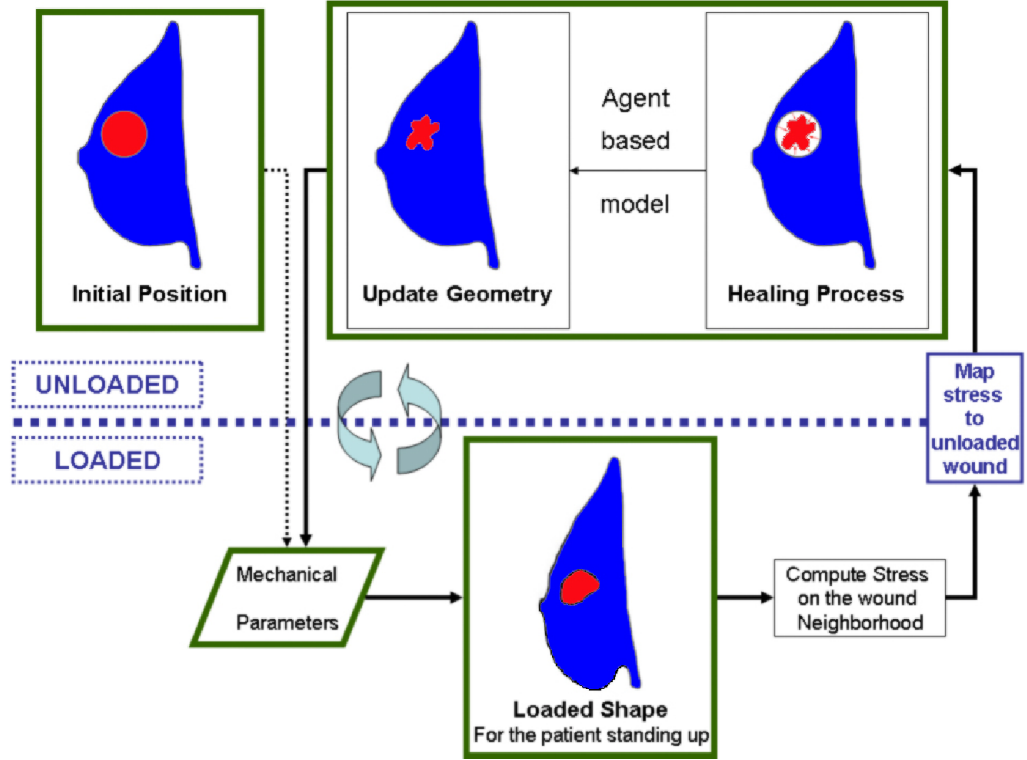


Figure 10.1: Illustration of the two steps Algorithm.

2. spatial scale, the mechanical model is operated at the centimetric scale, with average size of mesh element being in millimeter units, while the healing computes cells as agents and approximates their size to about  $20\mu m$ , which is an order of magnitude  $10^4$  times superior of the mechanical model scale.

In this model, we implement this method for a two-dimensional configuration. The mechanical part is computed using the Finite Element Modeling (FEM) commercial software ANSYS<sup>TM</sup> [8]. The breast structure was meshed using PLANE182 elements. PLANE182 is a 2D solid structure modeling element, defined by four nodes

---

**Algorithm 4** Two-time scale model

---

```
1: Get initial unloaded position  $\Rightarrow Breast_0$ 
2: for Till wound recovery do
3:   Compute Loaded shape of  $Breast_0$ 
4:   Compute Get stress at the wound  $\Rightarrow \sigma_{wound}$ 
5:   Map  $\sigma_{wound}$  in unloaded shape  $\Rightarrow \sigma_{wound}^0$ 
6:   for healing cycle do
7:     Compute healing using  $\sigma_{wound}^0$ 
8:   end for
9:   Get new wound shape in unloaded position
10:  Update  $Breast_0$ 
11: end for
12: Output results
```

---

having two degrees of freedom each, translations in the nodal  $\mathbf{x}$  and  $\mathbf{y}$  directions. It has the capabilities to model large strains and hyperelastic materials. The mesh size for this simulation was  $2mm$ . We considered the front skin as a free surface and fixed all displacements for the back of the breast. The Neo-Hookean hyperelastic mechanical model was used to model breast tissue deformations (see eq 2.14). Simulations were performed with an initial shear modulus  $\mu = 3448 \text{ Pa}$ , a bulk modulus  $\kappa = 33333 \text{ Pa}$ , and a tissue density  $\rho = 1000 \text{ kg.m}^{-3}$ . In order to simulate the shrinking of tissue we penalize the determinant term of the elastic deformation gradient,  $J$ , at the neighborhood of the wound according to the following expression:

$$J^{new} = J^{old}(1 + \alpha\Delta L)^3 \quad (10.1)$$

with  $\alpha = 0.3$  and  $\Delta L = -1$ . Aside from the wound neighborhood where we penalized volumetric components to simulate tissue contraction, the breast tissue was considered as homogeneous.

In our model we consider an active layer of the wound where cell division is promoted

by the mechanical stress experienced [70]. We will represent, this mechanical stress stimuli by computing the energy,  $E$ , at the wound through the following equation:

$$E(\theta) = \sigma_x \varepsilon_x + \sigma_y \varepsilon_y + \sigma_{xy} \varepsilon_{xy} \quad (10.2)$$

where  $\theta$  parametrizes the wound edge.  $\sigma_*$  is the stress components of the stress tensor and  $\varepsilon_*$  the strain component of the strain tensor. This energy function will be used for the healing model later (see section 10.2).

## 10.2 Model for wound healing

The healing model used a CA over a finite spacial grid, with each grid element representing a cell. Each cellular automaton cell is defined by a finite number of states, and follows a simple set of rules that are common to all the cells of the CA that only involve neighborhood interactions. The complex behavior of the evolution of the considered area of cells emerges from a large number of sites of CA, which are required to match the spacial scale of the model. This is the main advantage of the realistic approach of the CA where the complexity of the simulation comes from the large dimension of the system instead of the degree of complexity of the models that rule the system. A hexagonal grid was used, which represents the complex spacial distribution of cells in tissues; in this model one cell is surrounded by six neighbors. Since each site represents a cell, with an average cell diameter being  $20\mu m$ , a domain of centimetric size for the computation will require an order of magnitude of  $10^7$  number of CA sites. The state of each CA is either empty or occupied by a cell, and the cell can undergo two types of transformation. Cells can either divide (mitosis)



or migrate. The model is described by four successive operators that applies to the CA at each time step(here a cell cycle): division of the cell at the wound edge, cell mobility, cell division inside the active layer of the wound, and cell redistribution.

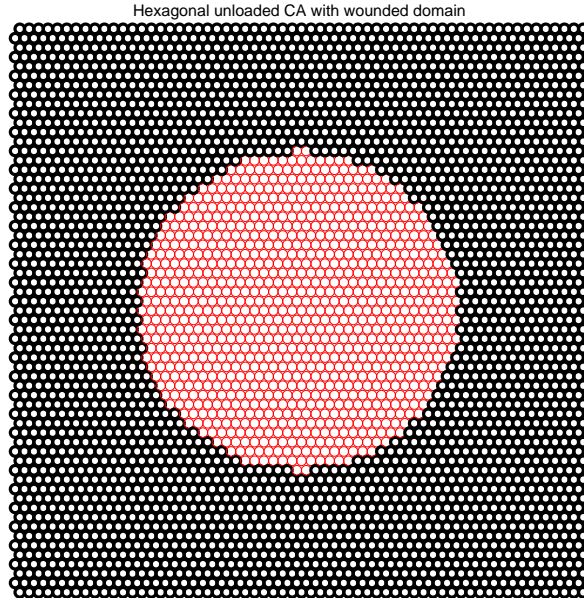


Figure 10.2: Hexagonal grid for CA.

We define  $\Omega$  as the considered domain,  $\Omega_{wound}$  the domain occupied by the CA with no cell present, and  $\Gamma$  the wound edge. The algorithm is initialized such as  $u_i = 1$  for the resected area ( $\Omega_{wound}$ ), and  $u_i = 0$  outside the resected area ( $\Omega \setminus \Omega_{wound}$ ).

### (i) Cell division at the wound edge

This step only applies to cells that are located at the wound edge and simulate the invasion by tissue cells of the area where the tissues are removed after BCT. In this step, the cell of the wound edge ( $\Gamma$ ), and the one in contact with the wound area ( $\Omega_{wound}$ ), are assigned a random probability,  $p$ . If this probability is greater than the predefined probability  $p^{edge}$ , then mitosis is considered to happen, affecting a random free site among the neighbors.

### (ii) Cell mobility

This step concerns only the cells of the resected wound,  $u \in \Omega_{wound}$ . Motion is simulated by diffusion towards the empty sites of the CA. Indeed, uniform diffusion corresponds to an equi-probabilistic migration of the cells where the probability of a cell to move to an empty site is  $\frac{q}{6}$ , with  $q$  being the number of empty sites surrounding the cell. The probability distribution  $U_i \in [0, 1]$  of a cell after diffusion is computed using a P1 finite element approximation of the diffusion operator

$$\partial_t - \Delta \tag{10.3}$$

on the hexagonal grid. The probability of the CA site is computed explicitly from the initial values (0 or 1) of the sites of the CA:

$$u_i^{n+1} = u_i^n + \frac{1}{2} \left( \frac{1}{6} \sum_{neighborsitesj} u_j - u_i \right) \tag{10.4}$$

This scheme is repeated over  $N_d$  iterations, where  $N_d$  serves as the mobility parameter for the model. From this probability distribution we select the empty sites where

cells have migrated and the ones that have become vacant, by selecting the level set of  $U = U_0 \in (0, 1)$  such that the number of sites where  $U \geq U_0$  conserves the total number of cells.

### (iii) Cell division inside the active layer

Unlike step (i), we consider here the cells that are inside an active layer of  $\Omega \setminus \Omega_{wound}$  and that are subject to the mechanical stress of the tissues. The active layer is a preselected area around the wound. The propability of mitosis in the tissue is a function of the strain energy,  $E$  (see eq. 10.2). The growth factor is calculated first by applying the diffusion operator (10.4) to all the sites  $u_i^{old}$  and then by thresholding at 0 the resulting value, i.e. the sites where  $u_i^{new} > 0$  will undergo mitosis with a non-uniform probability  $p^{inside}$ . We define  $E(\theta)$ , the energy along the wound edge  $\Gamma$  and  $E_{max} = \max_{\theta}(E)$ . From this we compute:

$$p^{inside}(u_i) = p^{activelayer} \left( E_0 + E_1 \frac{E_i}{E_{max}} \right) \quad (10.5)$$

where

$$E_i = E(\theta_i), \theta_i = \operatorname{argmin}_{\theta} d(\theta, u_i)$$

with  $d(\theta, u_i)$  the L2 distance between the position of the site  $u_i$  in  $\Omega$  and  $\theta$ , and  $E_0$  and  $E_1$  are weighting the influence of the strain energy on the probability distribution and  $p^{activelayer}$  is the predefined probability of mitosis inside the active layer.

#### (iv) Cell redistribution

Once the density of probability cell division inside the active layer is known, we can create a new array of sites  $u_i^{mitosis}$  of the cells of the active layer that will undergo mitosis:

$$u_i^{mitosis} = \begin{cases} 1 & \text{if } n_i \geq p^{inside}(u_i) \\ 0 & \text{if } n_i < p^{inside}(u_i) \end{cases} \quad (10.6)$$

where  $n_i \in [0, 1]$  is pseudo-randomly generated from a standard uniform distribution.

After cell division inside the active layer we need to modify the arrangement of cells in the tissue so that each site of the CA remains occupied by a single cell. After the mitosis step each cell will exert a pressure (hydrostatic pressure) on its neighbors leading to a rearrangement of the cell distribution. We model this in the same fashion of the cell mobility step.

First we define a probability distribution using the operator (10.4) repeated over  $N_d$  times, initialized as well with  $u_i = 1$  inside the active layer and  $u_i = 0$  otherwise. Then we keep the probability distribution superior to zero only inside the empty area. Hence, the site with the maximum value of computed probability distribution corresponds to the final site of the shortest path for an active layer cell to move. In other words, a cell of the active layer that went through mitosis will move towards the site with the highest value of the probability density.

To avoid conflicts induced by equi-probability for two or more empty sites to be occupied after the redistribution step, we introduce a white noise  $p_i$  to the normalized

probability density:

$$p_i = \frac{p_i}{p_i^{max}} + 10^{-3}n_i \quad (10.7)$$

where  $n_i \in [0, 1]$  is pseudo-randomly generated from a standard uniform distribution as well. The new distribution of cells in the tissue is then retrieved using the same method as iii.

### 10.3 Preliminary results

Presented in this section are results for a two-dimensional simulation of a breast contraction. Represented in figure 10.3 is the breast geometry meshed with the resected area in the loaded position, parameters used are the following:  $p^{edge} = 0.05$  and  $p^{inside} = 0.02$ . Figure 10.4 shows the evolution of the energy along time as well as its non uniformity; the two peaks being induced by the mechanical stress due to gravity. In figure 10.5 we plotted the evolution of the closure of the wound area. We can see that the closure does not occur in an uniform way in all directions, this is due to the dependence of the active layer division due to the mechanical stress. In figure 10.6 we plot the loaded breast contour before and after the healing process. We can see that the breast after the healing process displays a more significant bump, and the overall breast reaches a lower level.

Merging the complete work achieved so far, the VSB and the coupled healing modeling, this work presents an innovative computational framework for clinical study. This tool allows to red flag patient with lower outcome for BCT, understand the

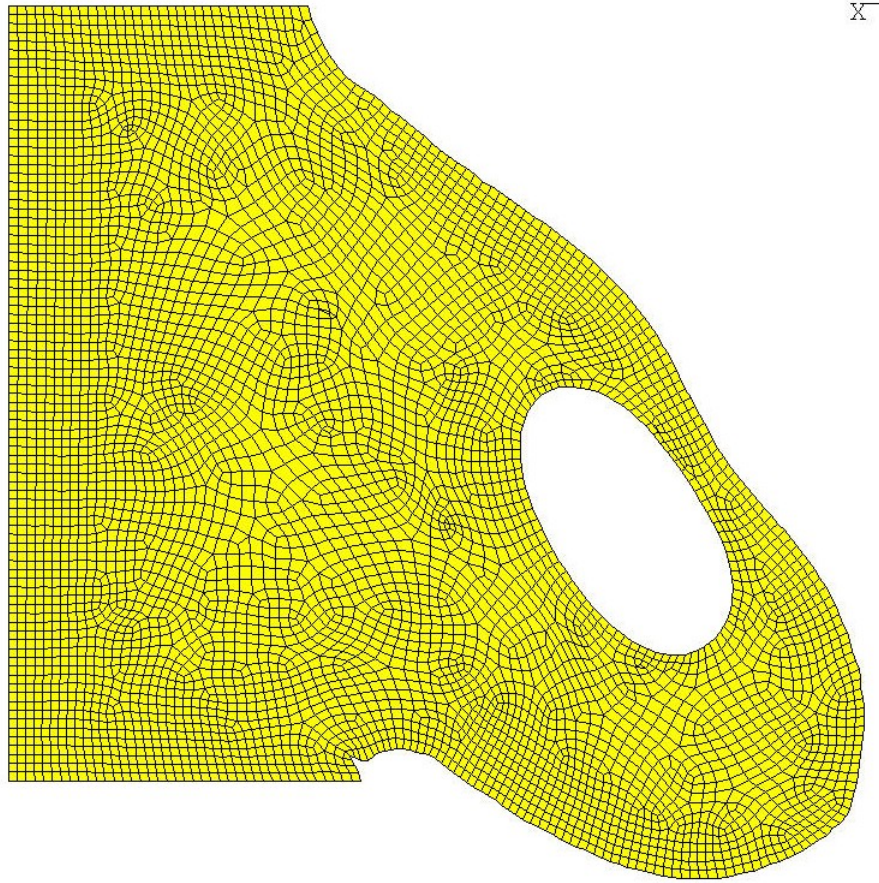


Figure 10.3: Meshing of breast with wounded area.

post surgery recovery, and therefore later allow clinicians to adapt the surgery to the patient thanks to the recovery knowledge gained. This tool is a first in its kind and the general idea should be applied for various types of surgery.

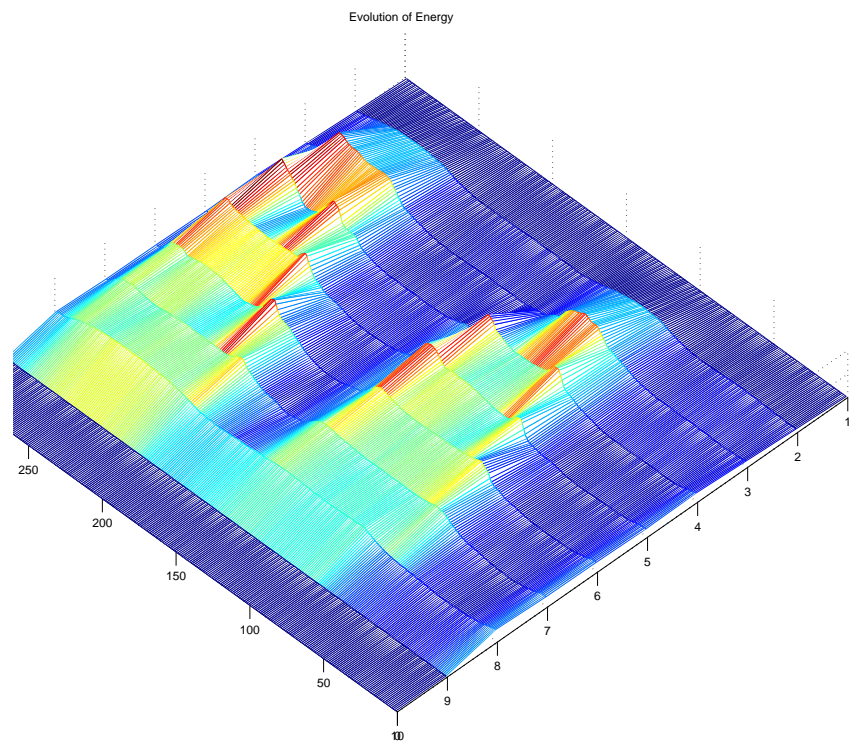


Figure 10.4: Evolution of strain energy through the healing process  $E(\theta) = f(t)$ .

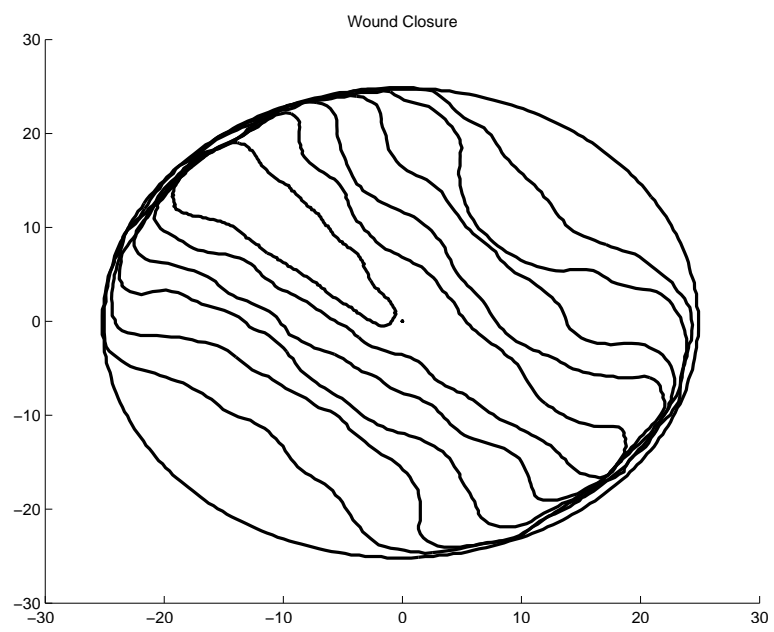


Figure 10.5: Closure of the wound: history of the wound area.



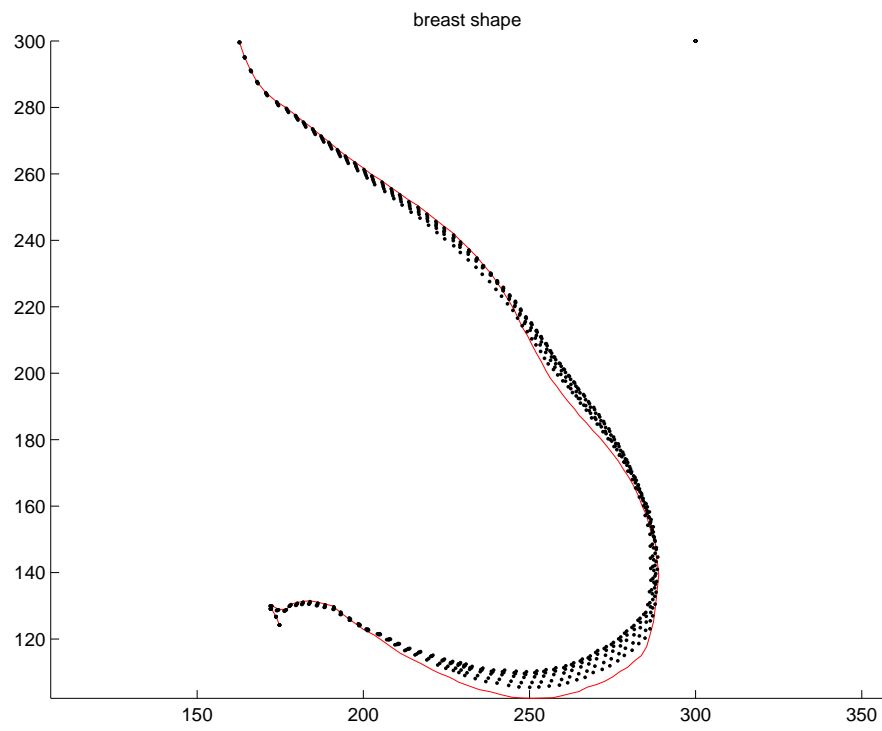


Figure 10.6: Final and intermediate shape of the breast through the healing process.

## Part IV

### Thesis review

# Chapter 11

## Conclusions and future work

The primary goal of this dissertation is to develop a computational framework for breast cancer treatment. Indeed the rise of technology in this last century is phenomenal, however a gap still exist between these advances and the actual implementation into the medical world. Taking more time than expected, was probably due to various ranges of variability among patients, and the need for science to get more stable inputs. This gap gives place in the medical world for a lot of uncertainty when treating diseases, i.e. patient over-treatment, patient under-treatment, patient re-excision. In this dissertation we developed tools that used the merging of various science such as computer science, mathematics and biology to benefit the outcome of breast cancer treatment, focusing on the development of DCIS growth model overexpressing HER2 and realistic mechanical model to perform BCT virtual surgery. In this chapter the conclusion of our work was presented, section 11.1 presents the conclusion derived from the tumor growth model. The conclusion from the breast conserving therapy

modeling was presented in section 11.2. This will be followed up in section 11.3 by the dissertation contributions, and finally in section 11.4 are detailed the potential for further studies in the area.

## 11.1 Tumor growth model studies

In this dissertation a continuous mathematical model was build to simulate tumor growth model, using PDEs. The model was adapted for DCIS with the potential of secreting MMP enzyme, allowing the tumor to switch into an invasive mode. The model considered healthy cells, the liquid lumen inside the duct, tumor cells, and necrosis cells, these entities were modeled as an incompressible fluid. The constitutive law to model the fluid dynamics was Darcy's law. The fluid motion dynamic was driven by cellular division only. The tumor growth was nutrient limited, the oxygen playing the role of nutrients. Also this model included a growth dependence regarding the concentration of a ternary complex  $[T]$ . Ternary complex was the result of a chemical reaction involving the HER2 oncogene. This tumor model is therefore likely to simulate DCIS cases that overexpresses HER2, which represents 30% of DCIS cases. The model was implemented into a 2D code using the eLYSe library.

The numerical simulation showed that the tumor was successfully simulating the pattern of solid tumor cases of DCIS with or without the presence of necrosis. The influence of various parameters controlling the chemical reaction was investigated, and this illustrated the influence of nutrients source location in our model. At last

tumor that was secreting MMP enzymes was computed, it showed that the growth was greater when the duct wall was broken.

To conclude this part of research, a potential improvement of our model was proposed in order to get a successful implementation and application of a 3-D clinical case. This model presents the advantage to be well adapted for clinical application since it is a continuous model, that inputs the environmental conditions directly into the equations. Using medical imaging technology to get a three-dimensional description of the duct network inside the breast, this model will easily simulate tumor growth model taking into account the whole environment. Which will lead to great clinical implementation. For instance it will enable surgeons to visualize exactly the region of the tumor to resect avoiding patient positive margin, and going for re-excision, which represents at least 10% of lumpectomy cases. Another implementation will be the ability to judge to what extent the radiation therapy should be applied, avoiding patient over or under treatment, leading to eventually disabling any case of local recurrence.

Implementing chemical reaction in the model, allows to include all phenomena involved in a cancer development, this model, will allow the understanding of tumor mechanism and trigger what are the factors for aggressive growth versus factors that have no influence.

## 11.2 Breast conserving therapy modeling studies

While BCS is the preferred therapy for most patients with early stage breast cancer, no tools or grading tools have been implemented further in order to answer the surgery outcome regarding the physiological aspects of such an intervention. In this work the design of a virtual surgery box to predict surgery outcome after a lumpectomy intervention was presented. This VSB has inputted, to date 4 sets of patient data. Our prototype system requires an MRI of the breast and, by design, a limited number of input parameters such as the radius and position of the resection, the stiffness of the tissue, and the potential dynamic of the recovery expressed as a pseudo pressure. These last two parameters must be estimated by the surgeons who may provide a range of values using their past experience. The outcome of the present study is the straight visualization of the breast shape before and after surgery, either by 3D visualization or displacements of plane section or marker points. Three-dimensional visualization results suggested that this could lead to some misinterpretation, leading to the conclusion that quantitative measurements will be more useful. Displacement information provide relevant conclusions on potential behavior. Pushing the analysis to a further step, indicator to assess the cosmetic outcome of surgery was created. It was derived as well a second indicator that evaluates the rate of relative change of normal stress occurring inside the breast after surgery. This indicator being “functional” as opposed to cosmetic or “geometric” because it measures the mechanical response of the tissue to resection. These indicators have the advantage to provide simple output that can be used to compare clinical cases and possibly lead to a classification of clinical outcomes rather than use the human eye

judgment of breast shape that is highly variable and relative to each person. Using the design of these indicators a sensitivity analysis was performed on the input parameters, rationalizing the sensitive physical parameters impacting the outcome of lumpectomy.

This work was followed by of a proposition of a more developed model for the VSB, adding a new module representing the healing process. This module was implemented in a multiscale fashion interacting with the mechanical model. Some preliminary results of this work for a two-dimensional configuration of a breast was outputted. This study brings the first brick to such a direction, trying to merge the technology advances made in different fields to benefit patient comfort and satisfaction as well as provide a powerful tool for surgeons to build on experience.

### **11.3 Work contributions**

The primary research contributions that was made during the course of this doctoral study are:

1. Implementation of a DCIS growth model expressing HER2;
2. Modeling of breast tumor invasion threw the release of MMP enzyme;
3. Breast tumor growth model that implemented the mechanical environment;
4. Implemented a breast MRI segmentation tool;
5. Mechanical modeling tool to simulate BCT surgery;

6. Design of cosmetic and functional indicator assessing the outcome of surgery using mechanical modeling;
7. Sensitivity analysis on successful factors for BCT;
8. Coupling healing model and mechanical model to simulate long term recovery of BCT surgery.

In item 4, 6, the work was performed on women with breast cancer who have elected to undergo BCT and are being treated at the Methodist Hospital in Houston, Texas.

## **11.4 Future work**

Merging these two studies could provide significant assistance to surgeons and patient facing breast cancer. Indeed, using the tumor growth model will allow clinicians to exactly measure the extent of the tumor and the exact resection needed for the patient. This quantification being made, clinicians will use the VSB to forecast post-surgery shape. The VSB will more likely output indicator scores in order for the users to classify the patient into a group and based on experience judge the likelihood of the BCT being an option for the patient. In order for this model to be complete the VSB should fully implement the recovery process such as the healing, a module that we already implement in two-dimension, but as well the effect of radiotherapy on tissue. It is expected that the radiation therapy will affect the tissue composition and more likely influence the final shape. Finally such a tool will need to be tested in a more significant pool of patient in order to tune the indicators. Also in order to get



a more accurate description of the breast it will be interesting to investigate the effect of using an heterogeneous tissue for the breast mechanical tissue model. In the long term, we expect future research to use this framework to engineer tissue material that will be inputted inside the tumor resection during BCT surgery, in order to process a controlled healing, limiting cosmesis and breast functionality defect as well as local recurrence of the tumor.

## 11.5 List of publications

- Boook chapters:

- [138] D. Thanoon, M. Garbey, N.-H. Kim, and B. L. Bass. A computational framework for breast surgery: Application to breast conserving therapy. *Computational Surgery and Dual Training*, pages 249–268, 2010;

- Conferences:

- [58] M. Garbey, D. Thanoon, F. Berjoan, and B. L. Bass. Simulation of breast conservative therapy. *The 20th International Conference on Domain Decomposition Methods*, February 2011;
- [137] D. Thanoon, M. Garbey, and B. L. Bass. Computational modeling of breast conserving surgery: a cosmetic outcome indicator from virtual surgery. *Conference Proceedings at the ISCA 3r International Conference on Bioinformatics and Computational Biology*, 2011;

- [57] M. Garbey, D. Thanoon, and B. L. Bass. Multi-scale modeling of breast conservative therapy. *PARENG2011*, April 2011;
- Journal:
  - [135] D. Thanoon, M. Garbey, and B. Bass. Computational modeling of breast conserving surgery(bcs) starting from mri imaging. *submitted to Medical Engineering Physics*, 2011;
  - [136] D. Thanoon, M. Garbey, and B. Bass. Deriving indicators for breast conserving surgery using finite element analysis. *submitted to CMBBE*, 2011;
  - [59] M. Garbey, D. Thanoon, R. Salmon, and B. Bass. Multiscale modeling and computational surgery: Application to breast conservative therapy. *JSSCM*, 5:81–89, 2011;
  - [55] M. Garbey, R. Salmon, D. Thanoon, and B. Bass. Multiscale modeling and distributed computing to predict of cosmesis outcome after a lumpectomy. *Invited for submission to the special issue of JCP*, 2011;
  - [56] M. Garbey, D. Thanoon, and B. Bass. Modeling and simulation for the lumpectomy of breast cancer. *submitted to Journal of Biomechanics and Modeling in Mechanobiology*, 2011.

# Bibliography

- [1] <http://www.breastpathology.info/sloane/dcis.html>, July 2010.
- [2] <http://www.cancer.org/>, July 2010.
- [3] <http://www.imaginis.com/mri-scan/work.asp>, October 2010.
- [4] <http://www.pathology.med.ohio-state.edu/ext/meded/med2visuals/>, July 2010.
- [5] <http://www.squidoo.com/my-breast-cancer-story>, October 2010.
- [6] <http://www.uwhealth.org>, October 2010.
- [7] <http://www.wikipedia.org>, July 2010.
- [8] <http://www.ansys.com>, September 2011.
- [9] <http://www.gehealthcare.com>, September 2011.
- [10] <http://www.mathworks.com>, September 2011.
- [11] <http://www.nbclosangeles.com/news/health/new-way-to-cure-breast-cancer-without-surgery-being-studied-94974834.html>, October 2011.
- [12] S. Al-Ghazal, L. Fallowfield, and R. Blamey. Comparison of psychological aspects and patient satisfaction following breast conserving surgery, simple mastectomy and breast reconstruction. *European Journal of Cancer*, 36:1938–1943, 2000.
- [13] S. K. Al-Ghazal, L. Fallowfield, and R. W. Blamey. Does cosmetic outcome from treatment of primary breast cancer influence psychosocial morbidity? *European Journal of Surgical Oncology*, 25:571–573, 1999.

- [14] M. Alber, M. Kiskowski, J. Glazier, and Y. Jiang. On cellular automaton approaches to modeling biological cells. In *IMA 134: Mathematical systems theory in biology, communication, and finance*. Springer-Verleg, New York., page 12, 2002.
- [15] D. Ambrosi and L. Preziosi. On the closure of mass balance models for tumor growth. *Mathematical Models and Methods in Applied Sciences*, 12(5):737–754, 2002.
- [16] A. R. A. Anderson and M. A. J. Chaplain. Continuous and discrete mathematical models of tumor-induced angiogenesis. *Bulletin of Mathematical Biology*, 60:857–900, 1998.
- [17] F. Azar, D. Metaxas, and M.D.Schnall. A finite element model of the breast for predicting mechanical deformations during interventional procedures. *Proc. Int. Soc. Magn. Reson. Med.*, 7(1084), 1999.
- [18] F. Azar, D. Metaxas, and M.D.Schnall. A finite element model of the breast for predicting mechanical deformations during biopsy procedures. *IEEE Workshop on Mathematical Methods in Biomedical Image Analysis*, 2000.
- [19] F. Azar, D. Metaxas, and M.D.Schnall. Methods for modeling and predicting mechanical deformations of the breast under external perturbations. *Medical Image Analysis*, 6:1–27, 2002.
- [20] F. S. Azar, D. N. Metaxas, and M. D. Schnall. A deformable finite element model of the breast for predicting mechanical deformations under external perturbations. *Academic Radiology*, 8(10):965 – 975, 2001.
- [21] J. Behrens, M. Mareel, F. V. Roy, and W. Birchmeier. Dissecting tumor cell invasion: Epithelial cells acquire invasive properties after the loss of uvomorulin-mediated cell-cell adhesion. *Journal of Cell Biology*, 108:2435–2447, 1989.
- [22] R. K. Benda, N. P. Mendenhall, D. S. Lind, J. C. Cendan, B. F. Shea, L. C. Richardson, and E. M. Copeland. Breast-conserving therapy (bct) for early-stage breast cancer. *Journal of Surgical Oncology*, 85(1):14–27, 2004.
- [23] F. Billy, B. Ribba, O. Saut, H. Morre-Trouilhet, T. Colin, D. Bresch, J. Boissel, E. Grenier, and J. Flandrois. A pharmacologically-based multiscale mathematical model of angiogenesis and its use in investigating the efficacy of a new cancer treatment strategy. *J Theor Biol.*, 260(4):545–562, October 2009.
- [24] A. Blake and M. Isard. *Active Contours*. Springer, 2000.

- [25] D. Bresch, T. Colin, E. Grenier, B. Ribba, and O. Saut. Computational modeling of solid tumor growth: The avascular stage. *SIAM J. Sci. Comput.*, 32:2321–2344, 2010.
- [26] X. Bresson. *Image segmentation with variational active contours*. PhD thesis, Ecole Polytechnique Federale de Lausanne, 2005.
- [27] H. M. Byrne and M. A. J. Chaplain. Growth of nonnecrotic tumors in the presence and absence of inhibitors. *Mathematical Biosciences*, 130:151–181, 1995.
- [28] N. Cabioglu, K. Hunt, A. Sahin, H. Kuerer, G. Babiera, S. Singletary, G. Whiteman, M. Ross, F. Ames, B. Feig, T. Buchholz, and F. Meric-Bernstam. Role for intraoperative margin assessment in patients undergoing breast-conserving surgery. *Annals of Surgical Oncology*, 14:1458–1471, 2007.
- [29] V. Caselles, R. Kimmel, and G. Sapiro. Geodesic Active Contours. *International Journal of Computer Vision*, 22(1):61–79, Feb. 1997.
- [30] T. F. Chan and L. A. Vese. Active contours without edges. *Image Processing, IEEE Transactions on*, 10(2):266–277, Feb. 2001.
- [31] L. Cheng, N. K. Al-Kaisi, F. Gebrail, R. R. Shenk, N. H. Gordon, and A. Y. Liu. Relationship between the size and margin status of ductal carcinoma in situ of the breast and residual disease. *Journal of the National Cancer Institute*, 89(18):1356–1360, 1997.
- [32] J.-H. Chung. *Modelling Mammographic Mechanics*. PhD thesis, Auckland Bioengineering Institute, The University of Auckland, 2008.
- [33] M. Dabeer, M. C. Fingeret, F. Merchant, G. P. Reece, E. K. Beahm, and M. K. Markey. A research agenda for appearance changes due to breast cancer treatmentassessment of breast aesthetics. *Breast Cancer: Basic and Clinical Research*, 2:1–3, June 2008.
- [34] J. E. de Vries, P. R. Timmer, E. J. Erftemeiert, and L. T. van der Weelet. Breast pain after breast conserving therapy. *The Breast*, 3(3):151–154, September 1994.
- [35] A. P. del Palomar, B. Calvo, J. Herrero, J. Lpez, and M. Doblar. A finite element model to accurately predict real deformations of the breast. *Medical Engineering & Physics*, 30(9):1089 – 1097, 2008.

- [36] M. Dillon, E. Mc Dermott, A. O’doherty, C. Quinn, A. Hill, and N. O’higgins. Factors affecting successful breast conservation for ductal carcinoma in situ. *Ann Surg Oncol*, 2007.
- [37] W. Duchting and T. Vogelsanger. Recent progress in modelling and simulation of three-dimensional tumor growth and treatment. *Biosystems*, 18:79–91, 1985.
- [38] A. Eladdadi and D. Isaacson. Mathematical model for the effects of her2 overexpression on cell proliferation in breast cancer. *Bulletin of Mathematical Biology*, 70:1707–1729, 2008.
- [39] H. Enderling, A. R. Anderson, M. A. Chaplain, A. J. Munro, and J. S. Vaidya. Mathematical modelling of radiotherapy strategies for early breast cancer. *Journal of Theoretical Biology*, 241:158–171, 2006.
- [40] H. Enderling, M. A. Chaplain, A. R. Anderson, and J. S. Vaidya. Mathematical modelling of radiotherapy strategies for early breast cancer. *Journal of Theoretical Biology*, 246:245–259, 2007.
- [41] H. Enderling and J. S. Vaidya. Mathematical modelling of breast carcinogenesis, treatment with surgery and radiotherapy, and local recurrence. *Selected Topics in Cancer Modeling*, 2008.
- [42] J. Engel, J. Kerr, A. Schlesinger-Raab, Hansjörg, and D. Hölzel. Quality of life following breast-conserving therapy or mastectomy: results of a 5-year prospective study. *The Breast Journal*, 10(3):223–231, 2004.
- [43] B. Erbas, E. Provenzano, J. Armes, and D. Gertig. The natural history of ductal carcinoma in situ of the breast: a review. *Breast Cancer Research and Treatment*, 97:135–144, 2006.
- [44] A. et al. Myoepithelial cells: good fences make good neighbors. *Breast Cancer Research*, 7(5), October 2005.
- [45] E. L. B. et al. Multiparameter computational modeling of tumor invasion. *Cancer Res.*, 69(10), May 2009.
- [46] H. B. F. et al. Prediction of drug response in breast cancer using integrative experimental/computational modeling. *Cancer Res.*, 69(10), May 2009.
- [47] M. et al. Clusters overlying focally disrupted mammary myoepithelial cell layers and adjacent cells within the same duct display different immunohistochemical and genetic features: implications for tumor progression and invasion. *Breast Cancer Research*, 5(6):231–241, 2003.

- [48] M. P. et al. Agen-based modeling of ductal carcinoma in situ: Application to patient-specific breast cancer modeling. *Computational Biology*, pages 77–111, 2009.
- [49] S. Franks and H. Byrne. Mathematical modelling of comedo ductal carcinoma in situ of the breast. *Mathematical Medicine and Biology*, 20:277–308, 2003.
- [50] S. Franks, H. Byrne, J. Underwood, and C. Lewis. Modelling the early growth of ductal carcinoma in situ of the breast. *Journal of Mathematical Biology*, 47:424–452, 2003.
- [51] S. Franks, H. Byrne, J. Underwood, and C. Lewis. Biological inferences from a mathematical model of comedo ductal carcinoma in situ of the breast. *Journal of Theoretical Biology*, 232:523–543, 2005.
- [52] D. A. Frassica, G. K. Bajaj, and T. N. Tsangaris. Treatment of complications after breast-conservation therapy. *Oncology*, 17(8), 2003.
- [53] U. Frixen, J. Behrens, M. Sachs, G. Eberle, B. Voss, A. Warda, D. Lochner, and W. Birchmeier. E-cadherin-mediated cell-cell adhesion prevents invasiveness of human carcinoma cells. *Journal of Cell Biology*, 113, 1991.
- [54] P. A. Ganz, A. C. Schag, J. J. Lee, M. L. Polinsky, and S.-J. Tan. Breast conservation versus mastectomy: Is there a difference in psychological adjustment or quality of life in the year after surgery? *Cancer*, 69(7):1729–1738, 1992.
- [55] M. Garbey, R. Salmon, D. Thanoon, and B. Bass. Multiscale modeling and distributed computing to predict of cosmesis outcome after a lumpectomy. *Invited for submission to the special issue of JCP*, 2011.
- [56] M. Garbey, D. Thanoon, and B. Bass. Modeling and simulation for the lumpectomy of breast cancer. *submitted to Journal of Biomechanics and Modeling in Mechanobiology*, 2011.
- [57] M. Garbey, D. Thanoon, and B. L. Bass. Multi-scale modeling of breast conservative therapy. *PARENG2011*, April 2011.
- [58] M. Garbey, D. Thanoon, F. Berjoan, and B. L. Bass. Simulation of breast conservative therapy. *The 20th International Conference on Domain Decomposition Methods*, February 2011.

- [59] M. Garbey, D. Thanoon, R. Salmon, and B. Bass. Multiscale modeling and computational surgery: Application to breast conservative therapy. *JSSCM*, 5:81–89, 2011.
- [60] A. Giese, L. Kluwe, B. Laube, H. Meissner, M. E. Berens, and M. Westphal. Migration of human glioma cells on myelin. *Neurosurgery*, 38:755–764, 1996.
- [61] R. C. Gonzalez and R. E. Woods. *Digital image processing*. Prentice Hall, 3rd edition edition, 2008.
- [62] H. P. Greenspan. Models for the Growth of a Solid Tumor by Diffusion. *Studies in Applied Mathematics*, LI(4), 1972.
- [63] G. A. Holzapfel. *Nonlinear solid mechanics: A continuum approach for engineering*. Wiley, 2000.
- [64] G. N. Hortobagyi, L. Esserman, and T. A. Buchholz. Neoplasms of the breast. *Cancer Medicine*, pages 1584–1643, 2006.
- [65] H.P. and Greenspan. On the growth and stability of cell cultures and solid tumors. *Journal of Theoretical Biology*, 56(1):229 – 242, 1976.
- [66] <http://www.math.u-bordeaux1.fr/MAB/mc2/>, October 2011.
- [67] <http://www.medtrng.com/posturesdirection.htm>, October 2010.
- [68] A. B. III and R. Heckendorn. Using evolvable genetic cellular automata to model breast cancer. *Genet Program Evolvable Mach*, 8:381–393, October 2007.
- [69] J. Ivins and J. Porcill. Everything you always wanted to know about snakes (but were afraid to ask). AIVRU Technical Memo # 86, 1993.
- [70] E. Javierre, F. J. V. and C. Vuik, and S. van der Zwaag. A mathematical analysis of physiological and morphological aspects of wound closure. *Journal of Mathematical Biology*, 59:605–630, 2009.
- [71] E. Javierre, P. Moreo, M. Doblare, and J. Garcia-Aznar. Numerical modeling of a mechano-chemical theory for wound contraction analysis. *International Journal of Solids and Structures*, 46:3597–3606, 2009.
- [72] E. Javierre, F. Vermolen, C. Vuik, and S. van der Zwaag. A mathematical analysis of physiological and morphological aspects of wound closure. *Journal of Mathematical Biology*, 59:605–630, 2009.



- [73] A. R. Kansal, S. Torquato, G. R. Harsh IV, E. A. Chiocca, and T. S. Deisboeck. Cellular automaton of idealized brain tumor growth dynamics. *Bio Systems*, 55(1-3):119–127, 2000.
- [74] A. R. Kansal, S. Torquato, G. R. H. IV, E. A. Chiocca, and T. S. Deisboeck. Simulated brain tumor growth dynamics using a three-dimensional cellular automaton. *J. THEOR. BIOL*, 203:367–382, 2000.
- [75] K. Kerlikowske, A. Molinaro, I. Cha, B.-M. Ljung, V. L. Ernster, K. Stewart, K. Chew, D. H. Moore, and F. Waldman. Characteristics associated with recurrence among women with ductal carcinoma in situ treated by lumpectomy. *Journal of the National Cancer Institute*, 95(22):1692–1702, 2003.
- [76] N.-H. Kim. *Introduction to nonlinear finite element analysis*. Springer, 1st edition edition, 2012.
- [77] Y. Kim, M. A. Stolarska, and H. G. Othmer. The role of the microenvironment in tumor growth and invasion. *Progress in Biophysics and Molecular Biology*, 106(2):353 – 379, 2011.
- [78] T. A. Krouskop, T. M. Wheeler, F. Kallel, B. S. Garra, and T. Hall. Elastic Moduli of Breast and Prostate Tissues Under Compression. *Ultrasonic Imaging*, 20:260–274, 1998.
- [79] A. K. Laird. Dynamics of tumour growth. *British Journal of Cancer*, 18(3):490–502, 1964.
- [80] S. Lankton and A. Tannenbaum. Localizing region-based active contours. *Image Processing, IEEE Transactions on*, 17(11):1–11, 2008.
- [81] S. M. Lankton. *Localized statistical models in computer vision*. PhD thesis, School of Electrical and Computer Engineering, Georgia Institute of Technology, 2009.
- [82] N. Larry. A gompertzian model of human breast cancer growth. *Cancer Res.*, 48:7067–7071, December 1988.
- [83] P. Macklin, M. E. Edgerton, and V. Cristini. Agent-based cell modeling: application to breast cancer. In *Multiscale Modeling of Cancer: An Integrated Experimental and Mathematical Modeling Approach*, chapter 10, pages 206–234. (invited author: P. Macklin).

- [84] P. Macklin, M. E. Edgerton, A. Thompson, and V. Cristini. Patient-calibrated agent-based modelling of ductal carcinoma in situ (DCIS): From microscopic measurements to macroscopic predictions of clinical progression. *J. Theor. Biol.*, 2011. (in final review).
- [85] L. Malvern. *Introduction to the mechanics of a continuous medium*. Prentice-Hall, 1969.
- [86] M. Marusic. Mathematical models of tumor growth, 1996.
- [87] S. R. McDougall, A. R. A. Anderson, M. A. J. Chaplain, and J. A. Sherratt. Mathematical modelling of flow through vascular networks: Implications for tumour-induced angiogenesis and chemotherapy strategies, 2002.
- [88] S. Michelson and J. Leith. Autocrine and paracrine growth factors in tumor growth: A mathematical model. *Bulletin of Mathematical Biology*, 53(4):639–656, 1991.
- [89] F. Michor, Y. Iwasa, and M. A. Nowak. Dynamics of cancer progression. *Nature reviews. Cancer*, 4(3):197–205, Mar. 2004.
- [90] I. A. E. Nathan J. Godde, Ryan C. Galea and P. O. Humbert. Cell polarity in motion: Redefining mammary tissue organization through emt and cell polarity transitions. *Journal of Mammary Gland Biology Neoplasia*, 15:149–168, 2010.
- [91] K. Norton, M. Wininger, G. Bhanot, S. Ganesan, N. Barnard, and T. Shinbrot. A 2d mechanistic model of breast ductal carcinoma in situ (dcis) morphology and progression. *Journal of Theoretical Biology*, 263:393–406, 2010.
- [92] H. Oka, H. Shiozaki, K. Kobayashi, M. Inoue, H. Tahara, T. Kobayashi, Y. Takatsuka, N. Matsuyoshi, S. Hirano, M. Takeichi, and et al. Expression of e-cadherin cell adhesion molecules in human breast cancer tissues and its relationship to metastasis. *Cancer Res.*, 53(7):1696–1701, 1993.
- [93] N. Olea, M. Villalobos, M. I. Nunez, J. Elvira, J. M. R. de Almodovar, and V. Pedraza. Evaluation of the growth rate of mcf-7 breast cancer multicellular spheroids using three mathematical models. *Cell Proliferation*, 27(4):213–223, 1994.
- [94] M. Olinick. Mathematical models in the social and life sciences, 2008.
- [95] J. Ophir, S. K. Alam, B. S. Garra, F. Kallel, E. Konofagou, T. A. Krouskop, and T. Varghese. Elastography: Ultrasonic Estimation and Imaging of the

- Elastic Properties of Tissues. *Proc. Instn. Mech. Engrs.*, 213:203–233, June 1999.
- [96] G. Osborn and E. Vaughan-Williams. Management of breast cancer: basic principles. *Surgery*, 28(3):130–134, 2009.
  - [97] C. Osborne, P. Wilson, and D. Tripathy. A mathematical model of breast and ovarian cancer treated with paclitaxel. *Mathematical biosciences*, 146:89–113, 1997.
  - [98] C. Osborne, P. Wilson, and D. Tripathy. Oncogenes and tumor supressor genes in breast cancer: Potential diagnostic and therapeutic applications. *The Oncologist*, 9:361–377, 2004.
  - [99] S. Osher and J. A. Sethian. Fronts propagating with curvature dependent speed: Algorithms based on hamilton-jacobi formulations. *JOURNAL OF COMPUTATIONAL PHYSICS*, 79(1):12–49, 1988.
  - [100] C. Ozan. *Mechanical Modeling of Brain and Breast Tissue*. PhD thesis, Georgia Institute of Technology, 2008.
  - [101] D. L. Page, W. D. Dupont, L. W. Rogers, and M. Landenberger. Intraductal carcinoma of the breast: follow-up after biopsy only. *Cancer*, 49(4):751–758, 1982.
  - [102] D. C. Pamplona and C. de Abreu Alvim. Breast reconstruction with expanders and implants: A numerical analysis. *Blackwell Publishing, Inc., International Center for Artificial Organs and Transplantation*, 28(4):353–356, 2004.
  - [103] N. Patani, B. Cutuli, and K. Mokbel. Current management of dcis: a review. *Breast Cancer Research and Treatment*, 111:1–10, 2008.
  - [104] A. A. PATEL, E. T. GAWLINSKI, S. K. LEMIEUX, and R. A. GATENBY. A cellular automaton model of early tumor growth and invasion: The effects of native tissue vascularity and increased anaerobic tumor metabolism. *Journal of Theoretical Biology*, 213(3):315 – 331, 2001.
  - [105] P. N. Patel and C. W. Patrick. Materials employed for breast augmentation and reconstruction. In *Scaffolding in Tissue Engineering*, pages 425–436, 2004.
  - [106] M. J. Piccart, W. C. Wood, C.-M. Hung, L. J. Solin, and F. Cardoso. *Breast Cancer Management and Molecular Medicine*. Springer, first edition, 2007.

- [107] A.-S. Qi, X. Zheng, C.-Y. Du, and B.-S. An. A cellular automaton model of cancerous growth. *Journal of Theoretical Biology*, 161(1):1 – 12, 1993.
- [108] V. Rajagopal. *Modelling Breast Tissue Mechanics Under Gravity Loading*. PhD thesis, Auckland Bioengineering Institute, The University of Auckland, 2007.
- [109] V. Rajagopal, J.-H. Chung, D. Bullivant, P. M. F. Nielsen, and M. P. Nash. Determining the finite elasticity reference state from a loaded configuration. *International Journal for Numerical Methods in Engineering*, 72(12):1434–1451, 2007.
- [110] V. Rajagopal, A. Lee, J.-H. Chung, R. Warren, R. P. Highnam, M. P. Nash, and P. M. Nielsen. Creating individual-specific biomechanical models of the breast for medical image analysis. *Academic Radiology*, 15(11):1425 – 1436, 2008.
- [111] D. Ramsay, J. C. Kent, R. A. Hartmann, and P. E. Hartman. Anatomy of the lactating human breast redefined with ultrasound imaging. *Bulletin of Anatomy*, 206(6):525–534, June 2005.
- [112] K. A. Rejniak and R. H. Dillon. A single cell based model of the ductal tumour microarchitecture. *Computational and Mathematical Methods in Medicine*, 8(1), July 2007.
- [113] B. Ribba, T. Colin, and S. Schnell. A multiscale mathematical model of cancer, and its use in analyzing irradiation therapies. *Theoretical Biology and Medical Modelling*, 3(7), 2006.
- [114] B. Ribba, O. Saut, T. Colin, D. Bresch, E. Grenier, and J. Boissel. A multiscale mathematical model of avascular tumor growth to investigate the therapeutic benefit of anti-invasive agents. *Journal of Theoretical Biology*, 243:532–541, 2006.
- [115] R. S. Rivlin and D. W. Saunders. Large elastic deformations of isotropic materials vii. experiments on the deformation of rubber. *Phi. Trans. Royal Soc. London Series A*, 243(865):251–288, 1951.
- [116] L. Ronnov-Jessen, O. W. Petersen, and M. J. Bissell. Cellular changes involved in conversion of normal to malignant breast: Importance of the stromal reaction. *Physiological Reviews*, 76(1), January 1996.
- [117] L. Roose, W. D. Maerteleire, W. Mollemans, F. Maes, and P. Suetens. Simulation of soft-tissue deformations for breast augmentation planning. *ISBMS LNCS*, 4072:197–205, 2006.

- [118] D. Rueckert, L. I. Sonoda, C. Hayes, D. L. G. Hill, M. O. Leach, and D. J. Hawkes. Nonrigid registration using free-form deformations: Application to breast mr images. *IEEE Transactions on Medical Imaging*, 18:712–721, 1999.
- [119] N. Ruiter, T. Müller, R. Stotzka, H. Gemmeke, J. Reichenbach, and W. Kaiser. Registration of x-ray mammograms and mr-volumes of the female breast based on simulated mammographic deformation. *Forschungszentrum Karlsruhe - Germany and Universitätsklinikum Jena - Germany*, 2004.
- [120] N. Ruiter, T. Müller, N. V. Müller, R. Stotzka, H. Gemmeke, W. Kaiser, and J. Reichenbach. Automatic image matching for breast cancer diagnostics, 2002.
- [121] A. Samani, J. Bishop, M. J. Yaffe, and D. B. Plewes. Biomechanical 3-d finite element modeling of the human breast using mri data. *Medical Imaging, IEEE Transactions on*, 20(4):271–279, April 2001.
- [122] A. Samani and D. Plewes. A method to measure the hyperelastic parameters of ex vivo breast tissue samples. *Physics in Medicine and Biology*, 49(18):4395, 2004.
- [123] A. Samani, J. Zubovits, and D. Plewes. Elastic moduli of normal and pathological human breast tissues: an inversion technique-based-investigation of 169 samples. *Physics in medicine and biology*, 52:1565–1576, 2007.
- [124] M. E. Sanders, P. A. Schuyler, W. D. Dupont, and D. L. Page. The natural history of low-grade ductal carcinoma in situ of the breast in women treated by biopsy only revealed over 30 years of long-term follow-up. *Cancer*, 103(12):2481–2484, 2005.
- [125] J. A. Schnabel, C. Tanner, A. D. Castellano-Smith, A. Degenhard, M. O. Leach, D. R. Hose, D. L. Hill, and D. J. Hawkes. Validation of nonrigid image registration using finite-element methods: application to breast MR images. *IEEE transactions on medical imaging*, 22(2):238–247, Feb. 2003.
- [126] J. A. Schnabel, C. Tanner, A. D. C. Smith, A. Degenhard, C. Hayes, M. O. Leach, D. R. Hose, D. L. G. Hill, and D. J. Hawkes. Validation of non-rigid registration of contrast-enhanced mr mammography using finite element methods, 2001.
- [127] M. Smalley and A. Ashworth. Stem cells and breast cancer: A field in transit. *Nature Reviews Cancer*, 3:832–844, November 2003.

- [128] A. L. Stanton, L. Krishnan, and C. A. Collins. Form or function? part 1. subjective cosmetic and functional correlates of quality of life in women treated with breast-conserving surgical procedures and radiotherapy. *American Cancer Society*, 91(12):2273–2281, 2001.
- [129] K. Swanson, E. Alvord Jr, and J. Murray. A quantitative model for differential motility of gliomas in grey and white matter. *Cell Prolif*, 33(5):317–329, 2000.
- [130] K. R. Swanson, E. C. Alvord, and J. D. Murray. Virtual brain tumours (gliomas) enhance the reality of medical imaging and highlight inadequacies of current therapy. *Br J Cancer*, 86(1):14–8, 2002.
- [131] C. Tanner, A. Degenhard, J. A. Schnabel, A. C. Smith, C. Hayes, L. I. Sonoda, M. O. Leach, D. R. Hose, D. L. G. Hill, and D. J. Hawkes. A method for the comparison of biomechanical breast models. In *Proceedings of the IEEE Workshop on Mathematical Methods in Biomedical Image Analysis (MMBIA'01)*. IEEE Computer Society, 2001.
- [132] C. Tanner, A. Degenhard, J. A. Schnabel, A. C. Smith, C. Hayes, L. I. Sonoda, M. O. Leach, D. R. Hose, D. L. G. Hill, and D. J. Hawkes. The comparison of biomechanical breast models: Initial results. In *ANSYS Proceedings*, 2002.
- [133] C. Tanner, J. A. Schnabel, D. L. Hill, D. J. Hawkes, M. O. Leach, and D. Hose. Factors influencing the accuracy of biomechanical breast models. *American Association of Physicists in Medicine*, 2006.
- [134] M. E. Taylor, C. A. Perez, K. J. Halverson, R. R. Kuske, G. W. Philpott, D. M. Garcia, J. E. Mortimer, R. J. Myerson, D. Radford, and C. Rush. Factors influencing cosmetic results after conservation therapy for breast cancer. *Int. J. Radiation Oncology Biol. Phys.*, 31(4):753–764, 1995.
- [135] D. Thanoon, M. Garbey, and B. Bass. Computational modeling of breast conserving surgery(bcs) starting from mri imaging. *submitted to Medical Engineering Physics*, 2011.
- [136] D. Thanoon, M. Garbey, and B. Bass. Deriving indicators for breast conserving surgery using finite element analysis. *submitted to CMBBE*, 2011.
- [137] D. Thanoon, M. Garbey, and B. L. Bass. Computational modeling of breast conserving surgery: a cosmetic outcome indicator from virtual surgery. *Conference Proceedings at the ISCA 3rd International Conference on Bioinformatics and Computational Biology*, 2011.

- [138] D. Thanoon, M. Garbey, N.-H. Kim, and B. L. Bass. A computational framework for breast surgery: Application to breast conserving therapy. *Computational Surgery and Dual Training*, pages 249–268, 2010.
- [139] V. G. Vaidya and F. J. A. Jr. Evaluation of some mathematical models for tumor growth. *International Journal of Bio-Medical Computing*, 13(1):19 – 35, 1982.
- [140] N. A. H. A. S. S. B. C. A. G. J. W. G. Li, X. Y. Luo and N. Bird. Correlation of mechanical factors and gallbladder pain. *Computational and Mathematical Methods in Medicine*, 9(1):27–45, 2008.
- [141] J. F. Waljee, E. S. Hu, P. A. Ubel, D. M. Smith, L. A. Newman, and A. K. Alderman. Effect of esthetic outcome after breast-conserving surgery on psychosocial functioning and quality of life. *Journal of Clinical Oncology*, 26(20):3331–3337, July 2008.
- [142] T. J. Whelan, M. Levine, J. Julian, P. Kirkbride, P. Skingley, and O. C. O. Group. The effects of radiation therapy on quality of life of women with breast carcinoma. *Cancer*, 88(10):2260–2266, 2000.
- [143] T. J. Whelan, M. Levine, J. Julian, P. Kirkbridge, and P. Skingley. The effects of radiation therapy on quality of life of women with breast carcinoma: Results of a randomized trial. *American Cancer Society*, 88(10):2260–2266, 2000.
- [144] C. Williams, I. A. Kakadiaris, K. Ravi-Chandar, M. J. Miller, and C. W. Patrick. Simulation studies for predicting surgical outcomes in breast reconstructive surgery. In *MICCAI (1)’03*, pages 9–16, 2003.
- [145] S. Wise, J. Lowengrub, H. Frieboes, and V. Cristini. Three-dimensional multispecies nonlinear tumor growth-i model and numerical method. *Journal of Theoretical Biology*, 253:524–543, 2008.
- [146] F. Xu, T. Lu, and K. Seffen. Biothermomechanics of skin tissues. *Journal of the Mechanics and Physics of Solids*, 56:1852–1884, 2008.
- [147] Y. Xu. A free boundary problem model of ductal carcinoma in situ. *Discrete and dynamical systems-series B*, 4(1), February 2004.
- [148] A. Yezzi, A. Tsai, and A. Willsky. A fully global approach to image segmentation via coupled curve evolution equations. *Journal of Visual Communication and Image Representation*, 13:195–216, 2002.

- [149] E. D. Yorke, Z. Fuks, L. Norton, W. Whitmore, and C. C. Ling. Modeling the development of metastases from primary and locally recurrent tumors: comparison with a clinical data base for prostatic cancer. *Cancer Res*, 53(13):2987–2993, 1993.
- [150] S. C. Zhu and A. Yuille. Region competition: Unifying snakes, region growing, and bayes/mdl for multi-band image segmentation. *IEEE Transactions on Pattern Analysis and Machine Intelligence*, 18:884–900, 1996.